eXPRESS Polymer Letters Vol.6, No.3 (2012) 177
Available online at www.expresspolymlett.com
DOI: 10.3144/expresspolymlett.2012.19

Editorial corner – a personal view

Future view of structural capacitor with laminated CFRP

A. Todoroki[*]

Tokyo Institute of Technology, 2-12-1, Ookayama, Meguro, Tokyo, Japan

The great east Japan earthquake has destroyed much of the sea cost area of Japan, and the Fukushima nuclear power plants. The nuclear accident caused by the earthquake changed the Japanese energy policy. It reminded the Japanese people the necessity of making the maximum possible use of renewable energy.

This new trend may accelerate weight reduction in all kinds of vehicles and thus to reduce the electric energy consumption. By the end of summer of 2011, Toray Industries Inc. in Japan, announced a new concept car made from carbon fiber/polymer composites. EVs and hybrid cars are loaded with electric capacitors or batteries. These equipments cause weight increase and are space demanding.

Structural capacitors made of composite materials offer solutions for these issues. Structural capacitors were initially adopted as multifunctional composite materials for unmanned air vehicles (UAV) to save both weight and space. The structural battery is also used for the UAV, but their usage is limited to military applications due to life limitation. On the other hand, structural capacitors have long functional life.

All this accelerate research in the field of the structural capacitors. Since carbon-fiber/polymer composites conduct electricity, the carbon-fiber ply can be applied as electrodes. Electrical conductance of carbon-fiber reinforced polymer (CFRP) has been investigated for long time. Research mainly focused on monitoring the effect of applied strain or damages on the change of electrical resistance of CFRP structures. Here electric current is direct current or the frequency of the alternating current is low. Under these conditions the CFRP laminate behaves as a simple anisotropic conductive material. When the CFRP structure is used as a capacitor, the high frequency electrical properties become important. This means that the impedance behavior of laminated CFRP at high frequency will be a next target of research for structural capacitors.

The laminated CFRP usually has electric conductivity even in the thickness direction. This means that the normal laminated CFRP cannot be used for the structural capacitor. Even for the highly toughened laminated CFRP used for new aircrafts, the laminated CFRP has electric conductivity in the thickness direction although the highly toughened CFRP exhibits thick resin rich interlayer.

Laminated CFRP has not been considered as an electrical material but counted on structural material, so not too many studies were done at higher frequencies. I believe the careful researches at frequencies higher than 0.5 to 1 MHz) should be conducted in the near future. These investigations surely bring significant changes in energy policy in all over the world within the decades.

Prof. Dr. Akira Todoroki
Member of International Advisory Board

---

[*] Corresponding author, e-mail: atodorok@ginza.mes.titech.ac.jp

eXPRESS Polymer Letters Vol.6, No.3 (2012) 178–188
Available online at www.expresspolymlett.com
DOI: 10.3144/expresspolymlett.2012.20

Properties of casting solutions and ultrafiltration membranes based on fullerene-polyamide nanocomposites

N. N. Sudareva[1*], *A. V. Penkova*[2], *T. A. Kostereva*[1], *A. E. Polotskii*[3], *G. A. Polotskaya*[1,2]

[1]Institute of Macromolecular Compounds, Russian Academy of Sciences, Bolshoy pr. 31, 199004 Saint Petersburg, Russia
[2]Saint Petersburg State University, Department of Chemical Thermodynamics & Kinetics, Universitetsky pr. 26, Petrodvoretz, 198504 Saint Petersburg, Russia
[3]State Research Institute of Ultrapure Biopreparations, Pudojskaya st. 7, 197110 Saint Petersburg, Russia

Received 7 July 2011; accepted in revised form 22 September 2011

Abstract. Poly(phenylene isophtalamide) (PA) was modified by fullerene C_{60} using solid-phase method. Novel ultrafiltration membranes based on nanocomposites containing up to 10 wt% of fullerene and carbon black were prepared. Properties of PA/C_{60} composites in solutions were studied by light scattering and rheological methods. The relationship between characteristics of casting solutions and properties of nanocomposite membranes was studied. Scanning electron microscopy was used for structural characterization of the membranes. It was found that increase in fullerene content in nanocomposite enhances the membrane rigidity. All nanocomposite membranes were tested in dynamic (ultrafiltration) and static sorption experiments using a solution of protein mixture, with the purpose of studying protein sorption. The membranes modified by fullerene demonstrate the best values of flux reduced recovery after contact with protein solution. It was found that addition of fullerene C_{60} to the polymer improves technological parameters of the obtained composite membranes.

Keywords: *nanocomposites, poly(phenylene isophtalamide), fullerene C_{60}, asymmetric membranes, ultrafiltration*

1. Introduction

Fullerenes exhibit a number of unique physicochemical properties. Particularly, being π-acceptor, fullerene molecule can be incorporated into a wide variety of polymers via formation of donor-acceptor [1, 2] or, in certain cases, covalent bonds [3, 4]. Polymer-fullerene complexes can be prepared either by synthesis or by mixing components in solvent or in solid phase; they exhibit properties different from those of the pristine polymer. Complexes obtained by mixing solutions usually contain 1–2 wt% of fullerene at the most [5, 6]. The solid-phase approach allows to increase fullerene content in the complexes appreciably (up to 10 wt%) [7–9]. The polymer-fullerene complexes have been extensively studied for several years, and the general view of their structure is still open to question. Polymer-fullerene complexes are studied using static (light scattering, NMR, diffusion, etc.) and dynamic methods. The static methods, which affect the solution structure very slightly, clearly indicate the existence of intermolecular associates [7, 10, 11]. Dynamic methods such as liquid chromatography, viscometry, sedimentation, and birefringence in flow characterize only individual macromolecules since intermolecular associates existing in solution are destructed by velocity gradients during the experiments [4, 7, 10, 12, 14, 15]. The change in polymer properties after modification by fullerene was demonstrated very clearly in the cases of poly(vinylpyrrolidone) (PVP)/fullerene and polystyrene (PS)/fullerene complexes. Properties of water-soluble PVP/C_{60} or

---

[*]Corresponding author, e-mail: nnsas@mail.ru

PVP/C_{70} complexes were studied in detail [7, 10–12, 15]. The light scattering investigation showed that the sizes of intermolecular associates were one or two orders of magnitude higher than those of PVP molecules; the diameter of associate increased with increasing fullerene content in the complex. The majority of the data concerning supramolecular association in complex solutions was obtained using dilute aqueous solutions of polymer-fullerene complexes. According to [16], water soluble supramolecular structures are stabilized by dipolar interaction. The study of polystyrene/C_{60} complexes by liquid chromatography showed that destruction of the polymer chain followed by the formation of PS-C_{60} covalent bonds occurred during the preparation of the samples (mixing of C_{60} and PS solutions with subsequent solvent evaporation and re-dissolving of the complexes). The degree of destruction increases with increasing polymer molecular weight (M_w) and deterioration of the solvent quality for fullerene C_{60} [4]. Intrinsic viscosities of solutions of many polymer-fullerene complexes including polymers of different structure and M_w were determined in various solvents [7, 13, 14]. The decrease in intrinsic viscosity of the complex as compared with that of pristine polymer was mainly observed in experiments with polymers having high M_w. Dynamic methods using controlled velocity gradients are of particular interest. For instance, sedimentation [12] and rheological [17] experiments with aqueous solutions of PVP/C_{60} complexes and birefringence in flow experiments using PVP/C_{70} solutions [10] showed that increase in velocity gradient leads to the destruction of the clusters (even to the appearance of pristine polymer at the velocity gradient of 5700 s^{-1} [12]). The destruction of covalent bonds in the PVP chains took place at the velocity gradient of 3000 s^{-1} in dilute aqueous solutions [18]. These data give indirect evidence that the clusters are destructed at high velocity gradients. The inclusion of fullerenes, other carbon and metal oxide nanoparticles in different polymers modifies the properties of films and membranes based on these polymers [3, 9, 19–30]. For example, the addition of small amounts of fullerene (up to 2–10 wt%) to poly (phenylene oxide) (PPO), PS, and PA changes selectivity and permeability of membranes made from these polymers in gas separation and pervaporation processes [3, 28–30]. Ultrafiltration membranes made from polysulfone [25], poly(ethersulfone) [26] and poly(vinylidene fluoride) [27] containing nanoparticles of titanium or zirconium oxides demonstrate surface and performance properties which are distinctly different from those of unmodified membranes. However, there are few data on the studies of fullerene-containing polymer membranes intended for ultrafiltration (UF). The asymmetric membranes based on PPO/C_{60} were developed and used for removing estrogenic compounds from wastewater [31, 32]. In the previous works [33, 34] we compared the structure and functional characteristics of pristine PA membranes and PA membranes modified by 5 wt% of nanocarbon additives (fullerene, nanotubes or carbon black). The objects of the present study were to produce poly(phenylene isophtalamide) – fullerene C_{60} composites with different fullerene content, to form asymmetric membranes based on these composites, and to investigate the influence of fullerene C_{60} on the casting solution properties and membrane characteristics. To reveal the specific character of fullerene C_{60} influence on the functional properties of the membranes, a comparative study using membranes of similar polymers modified by carbon black was carried out.

2. Experimental

Poly(phenylene isophtalamide) (PA, commercial Fenylon® sample, Vecton, Saint Petersburg, Russia), fullerene of 99,9% purity (C_{60}, Fullerene Technologies, Saint Petersburg, Russia), and carbon black (Fullerene Technologies, Saint Petersburg, Russia) were used for membrane preparation. Composites containing 2, 5, and 10 wt% of nanocarbons were obtained by intensive and thorough mixing of PA with fullerene or carbon black powders in porcelain mortar for one hour. After the solid-phase interaction, these composites were dissolved in N,N-dimethylacetamide (DMAc) containing ~0.7 wt% of LiCl added for stabilization of the solution; the solutions were kept during two days in a refrigerator. The prepared solutions were intensely stirred up before membrane preparation.These final solutions were used for the formation of asymmetric membranes by phase inversion technique, i.e. by immersion precipitation in the water bath at ambient temperature. The thickness of polymer layers before immersion and that of dried membrane were 0.35 mm and 0.20–0.22 mm, respectively. Fullerene-containing membranes were brown in color, and membranes containing carbon black were grey. The color intensity depended on the content of additives.

Static light scattering studies of polymer solutions were carried out using photogoniodiffusometer (FPS-3M, Science and Technical Association RAS, Saint Petersburg, Russia) equipped with a photoelectrical system of light scattering intensity registration at scattering angles in the 40–140° range and at the incident light wavelength $\lambda = 578$ nm. Calibration was made with respect to benzene (Rayleigh ratio at the given wavelength was $13.06\cdot10^{-6}$ cm^{-1}). Two parameters of scattering medium were calculated on the basis of the Debye-Stein theory [35] using the method described elsewhere [36]. The parameter av (the mean correlation radius of the polarizability fluctuation) is related to the dimensions of clusters, and the parameter $<\nu^2>$ (the average square of polarizability fluctuations) is related to the optical heterogeneity of solution.

The intrinsic viscosities ($[\eta]$) of different polymer-fullerene complexes were determined using Ubbelohde capillary viscometer in benzene or chloroform solution at 25°C. The dynamic viscosity (η) measurements of pristine polymer solution and the similar solution kept for twenty days were performed using rheogoniometer (PIRSP, Institute of Petrochemical Synthesis of RAS, Moscow, Russia) with cone-plate (cone angle 1°, diameter 40 mm), at the temperature of 25°C and different shear rates.

N,N-dimethylacetamide of ultra-pure grade (DMAc, Sigma-Aldrich Inc), benzene and chloroform of pure grade (Vecton, Saint Petersburg, Russia) were used without further purification.

Scanning electron microscopy (SEM) micrographs of membrane samples were obtained using electron microscope (JSM-35, Jeol, Japan). Ultrafiltration experiments were carried out in a dead-end stirred cell (FM-01, Science and Technical Association RAS, Saint Petersburg, Russia) (membrane diameter 25 mm, initial filtration volume 10 ml, transmembrane pressure 0.1 MPa, stirring speed 300 rpm).

The 0.4 wt% solution of the following mixture in the 0.05 M phosphate buffer (pH 7.4) was used in the experiment: tryptophan (M_w 204 Da), vitamin B12 (M_w 1340 Da), cytochrome C (M_w 12.5 kDa), chymotrypsinogen (M_w 24 kDa), ovalbumin (M_w 44.5 kDa), bovine serum albumin (M_w 67 kDa), γ-globulin (M_w 160 kDa) (all Sigma-Aldrich Inc). Static sorption of proteins was performed by dipping membrane into the hermetically closed cell containing 4 ml of protein mixture solution. These solutions were periodically stirred. The solute concentration was controlled periodically by determination the optical density of the solutions at λ = 280 nm and λ = 415 nm. Optical density was measured using the spectrophotometer (Specord M-40, Carl Zeiss, Jena, Germany). Equilibrium concentration was reached in 4 hours. The total duration of the experiment was 20 hours. Each experiment was repeated three times and the average result was reported.

3. Results and discussion

PA/C_{60} composites with different C_{60} content (up to 10 wt%) were prepared by solid-phase method. Mechanical destruction of particles increases their surface area and, correspondingly, the surface energy. Contacts between the polymer and carbon nanoadditives occur in the solid phase. The excess of the surface energy enhances activity and solubility of fine particles, thus providing formation of a material with the properties different from those of the pristine polymer. Figure 1 shows SEM images of (A) C_{60}, (B) PA, and (C) PA/C_{60}(10%) powders (the last sample - after thorough mixing). The comparison of images confirms that the surface interaction between PA and C_{60} powders takes place already at the solid-phase mixing stage.

As stated in the Introduction, fullerene molecule possesses the unique π-electron structure. Several authors used spectroscopy data to prove the existence of donor-acceptor interactions between polymer and fullerene in PS/C_{60} [4] and PVP/C_{60} [37] complexes. The authors of review [38] analyzed the data concerning changes of polymers properties in fullerene-doped polymer systems and suggested that the interaction between 'aromatic' C_{60} and phenylene rings of polymers takes place. Poly(phenylene isophtalamide) chain also contains phenylene rings. The possibility of donor-acceptor interaction of fullerene C_{60} with several active centers of a single PA molecule as well as with neighbor macromolecules in the pervaporation membrane matrix was discussed elsewhere [30].

The occurrence of fullerene – PA interaction will be taken into account in the analysis of our results

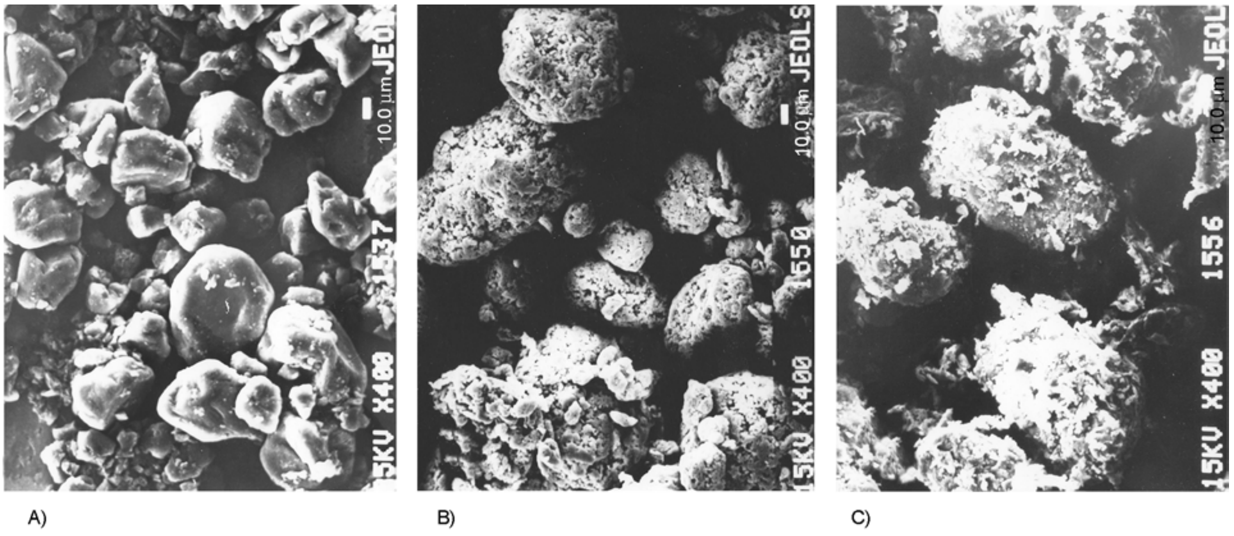

Figure 1. SEM images of powders: (A) C_{60}, (B) PA, and (C) PA/C_{60}(10%)

obtained during the study of properties of PA/C_{60} solutions and membranes.

3.1 Properties of PA/C_{60} solutions

Properties of PA/C_{60} complexes in DMAc solution were studied both by static (light scattering) and dynamic (viscometry and rheological study) methods. The supramolecular structure of polymer solutions was studied by static light scattering. Asymmetric indicatrixes of isotropic light scattering were obtained for dilute PA and PA/C_{60} solutions in DMAc at concentrations ranging from 0.01 to 0.1 wt%. The M_w of PA does not exceed 100 kDa, and the size of macromolecule is substantially less than the light wavelength. Therefore, the contribution of individual macromolecules to the light scattering asymmetry is negligibly small [39, 40]. We can conclude that clusters were already present in dilute PA/C_{60} solutions. Table 1 shows that the dimensions of clusters (a_v) in unperturbed dilute DMAc solutions increase with increasing C_{60} content. It should be mentioned that similar results were obtained in the study of water-soluble complexes of PVP with C_{60} or C_{70} [5, 7, 8]. Optical heterogeneity of solutions ($<\nu^2>$) also tends to rise with increasing C_{60} content. DMAc ($\varepsilon = 37.8$) is a polar solvent, as well as water, and the presence of soluble supramolecular structures is in agreement with the results reported in [16]. Intrinsic viscosities of solutions of various polymers and their complexes with fullerene are compared in Table 2 where both original and published data are given. It was found that the intrinsic viscosity of PA/C_{60} decreases with increasing C_{60} content. The decrease in [η] values of the polymer-fullerene complexes was observed for polymers of different chemical nature, M_w, various fullerene content, and in different solvents [7, 13, 14, 34]. The higher the polymer M_w, the more substantial decrease in the inherent size of polymer-fullerene complex takes place. For PVP with M_w = 12 kDa the [η]

Table 1. Sizes of intermolecular associates and optical heterogeneity parameters in DMAc solutions

Sample	PA	PA/C_{60}(2%)	PA/C_{60}(5%)
a_v [nm]	31	49	57
$< \nu^2 > \cdot 10^{10}$	6.7	6.8	6.9

Table 2. Intrinsic viscosity of polymers and their complexes with fullerene (cited and original data)

Polymer – solvent	Pristine polymer M_W [kg/mol]	C_{60} content [wt%]	[η] of composite [dl/g]	[η] of pristine polymer [dl/g]	Ref.
PA – DMAc	100	2.0 5.0 10.0	2.86 2.70 2.52	2.93	[34]
Poly(α-methyl styrene) – chloroform	500	6.1	0.76	0.87	
PVP – chloroform	360	0.4	0.90	1.32	
PVP – water	12	0.2	0.102	0.102	[7]
PPO – benzene	30 140	0.5 0.5	0.47 0.86	0.59 0.99	[13]
PS – benzene	1130	6.2	1.90	2.40	[14]

value of its fullerene-containing complexes remains virtually constant (Table 2) [7]. These results are in good agreement with the model of polymer-fullerene interaction suggested in [4]. It should be emphasized that for polydisperse compositions the [η] value is an integral parameter that allows rather comparing macromolecular sizes than determining them precisely.

Rheological behavior of PA/C_{60}(10%) casting solutions used for membrane preparation shows that the increase in fullerene C_{60} content leads to a slight increase in the dynamic viscosity of casting solution. This characteristic indicates the interaction between polymer molecules, polymer-fullerene and polymer-solvent interaction. On the contrary, carbon black as inert additive had virtually no influence on the dynamic viscosity of 10 wt% casting solutions. Figure 2 shows the dependences of dynamic viscosities of fresh casting solutions on velocity gradient. The differences in dynamic viscosities of PA solutions and PA solutions containing from 2 to 10 wt% C_{60} were more pronounced at minimal hydrodynamic action. With increasing velocity gradient, the values of dynamic viscosity descend and approach each other. The casting solutions of polysulfone with porous ZrO_2 nanoparticles also revealed shear thinning under rheological experiments [25]. In both cases a polymer-particle network was broken by the applied force. It would seem that the rheological behavior of PA/C_{60} solutions with different C_{60} content and the values of their intrinsic viscosity are in conflict. However, here the value of velocity gradient (γ) should be taken into account. In rheological experiments, it did not exceed 220 s^{-1}, whereas in intrinsic viscosity measurements the γ value reached 700 s^{-1} [7]. Apparently, clusters having dimensions proportional to fullerene content (in the absence of hydrodynamic action) dissociate at these velocity gradients; therefore, the [η] values characterize the individual molecules.

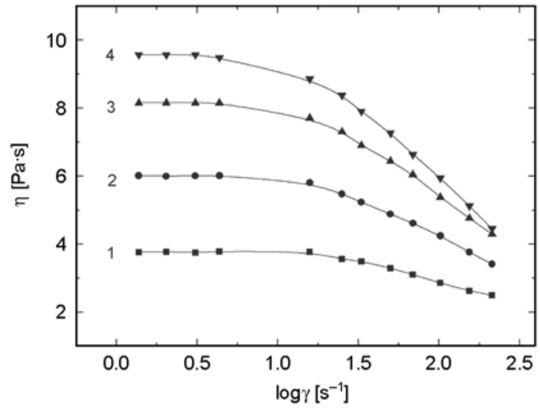

Figure 2. Viscosity vs. velocity gradient for casting solutions of (1) PA and PA/C_{60} with various C_{60} content: (2) 2%; (3) 5%; (4) 10%

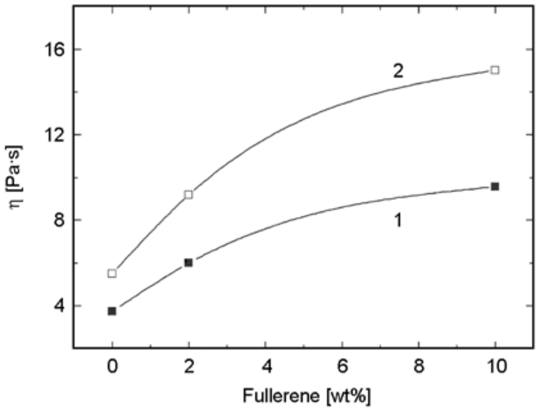

Figure 3. Viscosity vs. C_{60} content in 10% casting solution of PA/C_{60}. (1) pristine solutions and (2) kept 20 days casting solutions.

Rheological data characterizing the instability of casting solutions are shown in Figure 3. After 20 days the dynamic viscosity of PA casting solutions increased to a lesser extent than that of fullerene–containing solutions. The initial values of dynamic viscosity were reached after ultrasonic treatment of these solutions. This observation can serve as another proof of the lability of clusters formed in polymer solutions. It should be added that precipitation of PVP/C_{60} complex from chloroform solution as well as precipitation of poly(α-methyl styrene)/C_{60} complex from benzene – tetrahydrofuran mixture was also observed after storage for several days. The structure-forming ability of complexes can be crucial in technological applications; and, consequently, the long-term storage of solutions should be avoided.

3.2. Structural properties of membranes

The discussion about correspondence between the properties of complex solution and composite membrane characteristics will be based on the results given in this paper and on the data published before [33, 34].

The properties of casting solution determine structural and functional characteristics of the membrane obtained. To support this proposition, we will use the data shown in Figures 4–7 as well as the results published earlier (Table 1 [33]).

All studied membranes were prepared by phase inversion method. The porous structure of membranes was formed during the immersion of polymer solution layer into precipitating water bath. The slower the membrane precipitation, the higher the density of the obtained membrane [41, 42]. The rate of water diffusion primarily depends on the viscosity of polymer solution. Casting solutions with higher C_{60} content were more viscous (Figure 2), leading to the formation of asymmetric membranes with lower overall porosity. The density of nonporous films prepared from the same solutions by evaporation also increased with increasing C_{60} content. (The data about membrane porosity and films density were provided in Table 1 [33]). These data are in agreement with published results [25].

The SEM images of PA/C_{60} membranes show homogeneous surfaces. The membrane morphology does not change with increasing fullerene amount in composite. The surface pore size of ultrafiltration membrane can be evaluated using calibration curve obtained in a previous study (Figure 4 [34]). The inclusion of carbon additives into membranes did not influence the shape of calibration curve and retained the molecular weight cut-off (MWCO) in the range of 40–50 kDa. (The value of MWCO is equal to M_w of protein rejected by 90%). Taking into account the size of rejected globular proteins, the surface pore size was estimated using a method described elsewhere [43]. The pore size was about 17 nm. SEM resolution used in our experiments (magnification up to 40 000) did not allow to see the distinctions in active layers of membranes having different composition. The tendency towards increasing active layer density (Figure 4) was observed for membrane containing 5 wt% C_{60} as compared with the pure PA membrane. During preparation of SEM samples, the fullerene-containing membranes exhibited higher strength and ability to preserve their internal structure. It should be noted that SEM does not allow observing all changes in membrane structure. For example, while gas separation membranes based on polysulfone with different carbon additives were of similar morphology they demonstrated different transport properties [44].

3.3. Functional properties of membranes

The effect of fullerene C_{60} present in PA membranes on their main functional characteristics (flux and protein sorption) was studied. Figure 5 (curve 1) shows water flux through membranes with different fullerene C_{60} content. The data given in Table 1 [33]

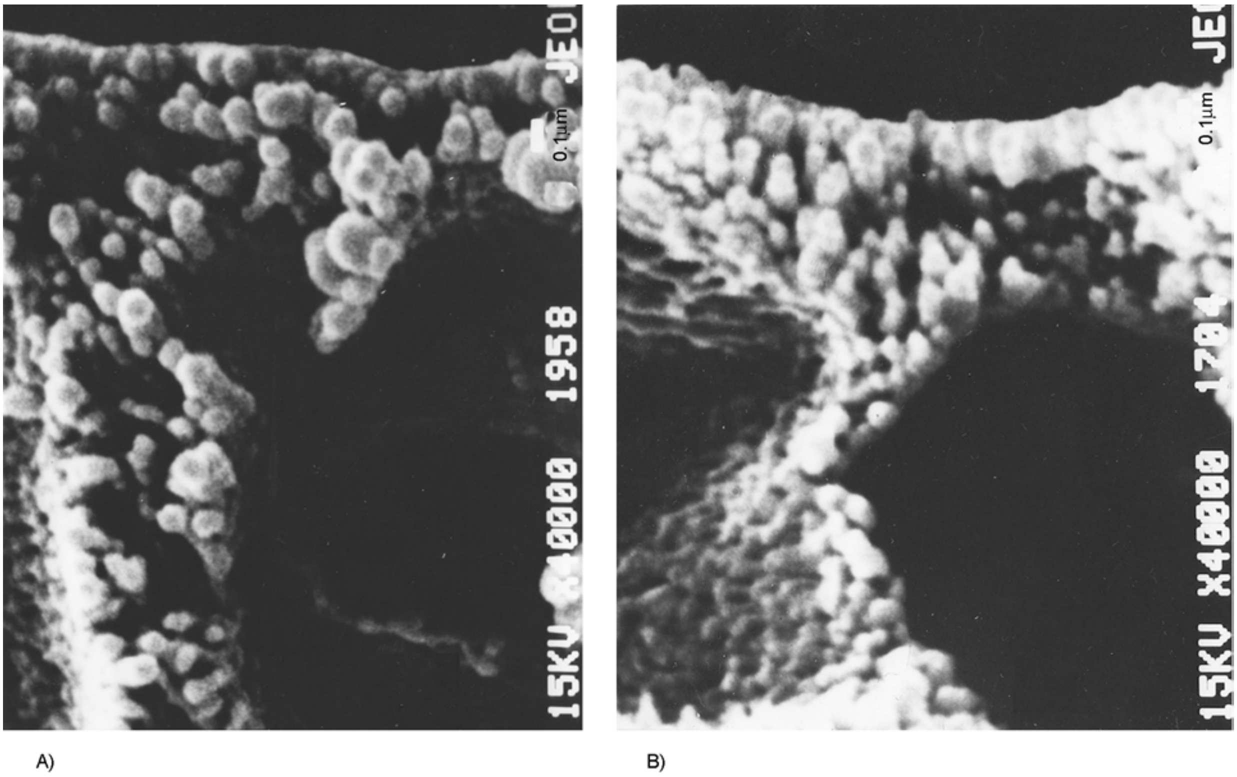

Figure 4. SEM images of (A) PA and (B) PA/C_{60}(5%) membranes active layer cross-section

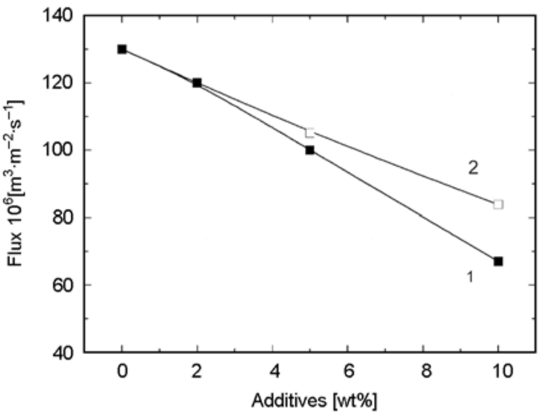

Figure 5. Water flux through composite membranes vs. carbon additives content. (1) fullerene, (2) carbon black.

show that the polymer-fullerene interaction slightly affects the membrane porosity and structure. Membranes with higher C_{60} content have lower porosity and demonstrate lower flux. To reveal the specific character of C_{60} influence on the functional properties of the membranes, the comparative study was carried out using similar membranes modified by carbon black. Figure 5 (curve 2) shows that the water flux through membranes containing carbon black additives is higher than that in the case of fullerene-containing membranes. Carbon black is an inert filler that causes mechanical obstructions against the liquid flow through porous structure of the membrane. If fullerene molecule were also inert with respect to polymer, the obstructions against flow would be similar in both cases. The presence of donor-acceptor interactions (for example, between fullerene and PA phenylene groups) leads to arising intermolecular attraction inside membrane matrix. These interactions cause lowering water flux through fullerene-containing membrane as compared with membrane containing inert carbon black.

Stability of membrane flux during filtration is one of the important technological characteristics of membrane process. Principal sources of decreasing the flux through the ultrafiltration membrane are concentration polarization, cake layer deposition on membrane surface, and adsorptive fouling [45, 46]. In the final stages of technological processes the flux characteristics are determined mainly by cake layer deposition, its degree depending on the composition of filtered mixture. The adsorptive fouling is an important cause of decreasing the protein flux [47, 48] especially on the initial stages of ultrafiltration [49]. In our work, the membrane fouling was studied under similar conditions (filtrate volume did not exceed 0.9 of initial proteins solution volume). We assumed that the adsorption of proteins on the membrane surface and pores caused decrease in flux, and this assumption was confirmed by determination of phosphate buffer flux reduced recovery (FRR). FRR was estimated after the contact between membrane and protein solution in ultrafiltration process and in static sorption tests, when membranes were held in protein solution for 20 hours. Both types of tests included measurements of phosphate buffer flux before (Q_0) and after (Q_1) contact between membranes and protein solution. Flux reduced recovery was calculated using Equation (1):

$$FRR = \frac{Q_1}{Q_0} \cdot 100 \qquad (1)$$

Figure 6 shows the phosphate buffer flux reduced recovery for membranes which contacted with protein solution in ultrafiltration and static sorption tests. Evidently, the curves obtained in ultrafiltration experiments lie below the ones obtained in sorption tests. The mass transfer conditions are different in both tests. Under pressure gradient during ultrafiltration the greater part of protein molecules flows into the pores, as opposed to static sorption experiments. Internal membrane fouling is generally irreversible [45]. In our experiment the adsorptive fouling of membranes of different composition was influenced mainly by the chemical nature of

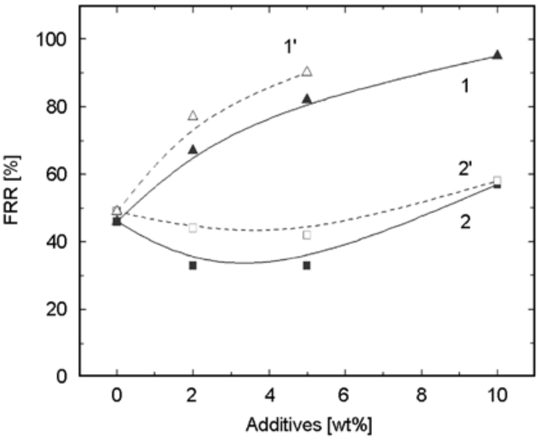

Figure 6. Flux reduced recovery of (1, 1′) PA/C_{60} and (2, 2′) PA/carbon black membranes vs. carbon additives content in (1, 2) ultrafiltration and (1′, 2′) static sorption

constituents, other factors (surface pore size, pressure, stirring rate, pH, ionic strength) being equal.

The membranes modified by fullerenes demonstrated high value of *FRR* equal to 70–90% (curves 1 and 1′). At the same time, *FRR* was close to 30–50% for the membranes of pure PA and modified by carbon black (curves 2 and 2′). Low *FRR* values indicate that membranes of pure PA and those modified by carbon black adsorb proteins strongly, and thus, their phosphate buffer flux decreased by a factor of 2 or 3. It should be noted that the similar behavior is common to the majority of known polymer membranes [48–50]. Membranes modified by fullerene adsorb proteins much less effectively than pure PA. We suppose that this phenomenon is caused by 'interlocking' fullerene sorption centers in PA which should adsorb proteins. On the surface of polyamide membrane both hydrophobic (phenylene) and hydrophilic (amide) groups are present. Fullerene interacts with phenylene group and changes surface profile, thus hindering adsorption of protein functional groups.

High *FRR* value of PA/C_{60} membranes is a very important operating characteristic that could facilitate process of membrane regeneration and promote decrease of target product losses. The resistance of the porous structure of the membranes to different solvents was estimated by filtration of various solvents through the membranes. The viscosities (η, 10^{-3} Pa·s) of the liquids used in this experiment were the following: 1.0 (water), 1.13 (ethanol), and 2.43 (*iso*-propanol). It should be noted that these solvents are often used in processes including ultrafiltration membranes for concentration, purification, and separation of proteins and similar compounds. In the previous paper [33] we reported that only negligible swelling of PA membranes with 5% of nanoadditives takes place in the liquids used. Here we estimated the stability of membrane structure by comparing the values of viscosity-normalized flux dispersion for the membranes with different composition. The viscosity-normalized flux (Q_n) is the product of the liquid viscosity and its flux through the membrane. The values of viscosity were adjusted to 22°C. Figure 7 shows the relative dispersions of viscosity-normalized flux (δQ_n). It was calculated by standard formula for root-mean square deviation. The mean value of normalized flux for definite membrane composition in these calculations was determined by averaging all normalized flux values for all solvents and all membranes used in the experiment. It is clear that relative dispersion of viscosity-normalized flux for PA and fullerene-containing membranes does not exceed 10% and decreases with increasing fullerene content. For membranes modified by carbon black, the relative dispersion does not correlate with the carbon black concentration and averages out 18%. Therefore, the modification by fullerene improves characteristics of membranes by increasing their resistance to different solvents.

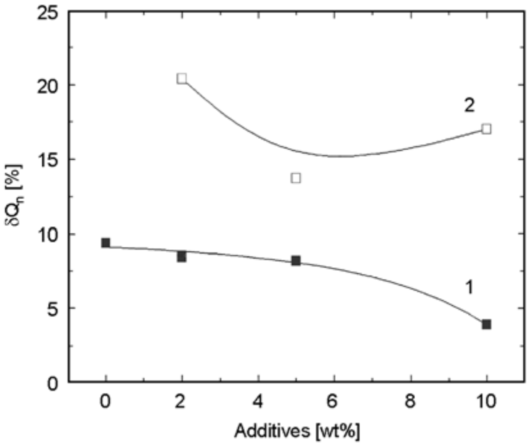

Figure 7. Relative dispersion of viscosity-normalized flux vs. carbon additives content. (1) fullerene, (2) carbon black

4. Conclusions

Asymmetric ultrafiltration membranes based on PA/fullerene C_{60} composites were prepared. The relationship between properties of casting solutions and the structure and characteristics of resulting asymmetric membranes was confirmed. It was established that increase in C_{60} content in the composite leads to the formation of rigid membranes and increases membrane resistance to organic solvents. Ultrafiltration of aqueous protein solutions, as well as static sorption experiments, showed that increase in C_{60} content in membrane causes decrease in protein adsorption on the membrane surface and inside pores. Therefore, the obtained membranes modified by fullerene demonstrate improved antifouling properties as compared with the membranes made from pure PA and those modified by carbon black. Hence, modification by fullerene improved technological parameters of membranes.

Acknowledgements

The authors are grateful to Dr. I.G. Silinskaya for performing light scattering experiments, Dr. N. N. Saprykina for providing SEM images and Ministry of Education and Science of Russian Federation (grant № 2011-1.3.1-207-008-058) for partial support of this work.

References

[1] Hammond G. S., Kuck V. J.: Fullerenes: Synthesis, properties, and chemistry of large carbon clasters. ACS Symposium Series, Washington (1992).

[2] Konarev D. V., Lyubovskaja R. N.: Donor–acceptor complexes and radical ionic salts based on fullerenes (in Russian). Russian Chemical Reviews, **68**, 23–44 (1999).
DOI: 10.1070/RC1999v068n01ABEH000460

[3] Sterescu D. M., Stamatialis D. F., Mendes E., Wübbenhorst M., Wessling M.: Fullerene-modified poly(2,6-dimethyl-1,4-phenylene oxide) gas separation membranes: Why binding is better than dispersing. Macromolecules, **39**, 9234–9242 (2006).
DOI: 10.1021/ma061300p

[4] Chubarova E. V., Melenevskaya E. Yu., Sudareva N. N., Andreeva O. A., Malachova I. I., Ratnikova O.V.: Degradation of macromolecular chains in fullerene C_{60}–polystyrene composites. Journal of Macromolecular Science Part B: Physics, **44**, 455–469 (2005).
DOI: 10.1081/MB-200061627

[5] Yamakoshi J. N., Yagami T., Fukuhara K., Sueyoshi S., Miyata N.: Solubilization of fullerenes into water with polyvinylpyrrolidone applicable to biological tests. Journal of the Chemical Society, Chemical Communications, **4**, 517–518 (1994).
DOI: 10.1039/C39940000517

[6] Biryulin Yu. F., Melenevskaya E. Yu., Mikov S. N., Orlov S. E., Petrikov V. D., Syckmanov D. A., Zgonnik V. N.: Optical properties of polydimethylphenyleneoxide free-standing films containing fullerene. Semiconductors, **37**, 108–111 (2003).

[7] Ratnikova O. V., Tarasova E. V., Melenevskaya E. Yu., Zgonnik V. N., Baranovskaya I. A., Klenin S. I.: Behavior of poly-n-vinylpyrrolidone-fullerene C_{60} composites in aqueous solutions. Polymer Science Series A, **46**, 752–756 (2004).

[8] Ong S. L., Hu J. Y., Biryulin Yu. F., Polotskaya G. A.: Fullerene-containing polymer membranes for rejection of estrogenic compounds in water. Fullerenes, Nanotubes and Carbon Nanostructures, **14**, 463–466 (2006).
DOI: 10.1080/15363830600666159

[9] Chung T-C., Chan S. S., Wang R., Lu Z., He C.: Characterization of permeability and sorption in Matrimid/C_{60} mixed matrix membranes. Journal of Membrane Science, **211**, 91–99 (2003).
DOI: 10.1016/S0376-7388(02)00385-X

[10] Tarassova E., Aseyev V., Tenhu H., Klenin S.: Poly (vinylpyrrolidone)-C_{70} complexes in aqueous solutions. Polymer, **44**, 4863–4870 (2003).
DOI: 10.1016/S0032-3861(03)00477-4

[11] Tarassova E., Aseyev V., Filippov A., Tenhu H.: Structure of poly(vinyl pyrrolidone) – C_{70} complexes in aqueous solutions. Polymer, **48**, 4503–4510 (2007).
DOI: 10.1016/j.polymer.2007.05.069

[12] Tarabukina E., Krasnov I., Ratnikova O., Melenevskaya E., Filippov A.: Effect of centrifugal field upon hydrodynamic characteristics of fullerene C_{60} and poly(N-vinylpyrrolidone) complex in aqueous solutions. International Journal of Polymer Analysis and Characterization, **12**, 203–220 (2007).
DOI: 10.1080/10236660701266997

[13] Lavrenko P. N., Evlampieva N. P., Volokhova D. M., Vinogradova L. V., Melenevskaya E. Yu., Zgonnik V. N.: Hydrodynamic and electrooptical properties of the C_{60}-poly(phenylene oxide) complex in solution. Polymer Science Series A, **44**, 173–178 (2002).

[14] Yevlampieva N. P., Dmitrieva T. S., Melenevskaya E. Yu., Zaitseva I. I., Ryumtsev E. I.: Interaction of polystyrene and fullerene C_{60} in benzene: Composition and molecular properties of the product. Polymer Science Series A, **49**, 284–291 (2007).
DOI: 10.1134/S0965545X0703008X

[15] Sushko M. L., Tenhu H., Klenin S. I.: Static and dynamic light scattering study of strong intermolecular interactions in aqueous solutions of PVP/C_{60} complexes. Polymer **43**, 2769–2775 (2002).
DOI: 10.1016/S0032-3861(02)00074-5

[16] Duval M., Sarazin D.: Properties of PEO in dilute solution under stirring. Macromolecules, **36**, 1318–1323 (2003).
DOI: 10.1021/ma0208638

[17] Krasnou I., Tarabukina E., Melenevskaya E., Filippov A., Aseyev V., Hietala S., Tenhu H.: Rheological behavior of poly(vinylpyrrolidone)/fullerene C_{60} complexes in aqueous medium. Journal of Macromolecular Science Part B: Physics, **47**, 500–510 (2008).
DOI: 10.1080/00222340801955289

[18] Nakano A., Minoura Y.: Degradation of aqueous poly(vinylpyrrolidone) solution by high-speed stirring. Journal of Applied Polymer Science, **21**, 2877–2884 (1977).
DOI: 10.1002/app.1977.070211103

[19] Vankayala R. R., Lai W-J. P, Cheng K-Ch., Hwang K. Ch.: Enhanced electrical conductivity of nylon 6 composite using polyaniline-coated multi-walled carbon nanotubes as additives. Polymer, **52**, 3337–3343 (2011).
DOI: 10.1016/j.polymer.2011.05.007

[20] Tasaki K., Gasa J., Wang H., DeSousa R.: Fabrication and characterization of fullerene–Nafion composite membranes. Polymer, **48**, 4438–4448 (2007).
DOI: 10.1016/j.polymer.2007.05.049

[21] Saga S., Matsumoto H., Saito K., Minagava M., Tanaoka A.: Polyelectrolyte membranes based on hydrocarbon polymer containing fullerene. Journal of Power Sources, **176**, 16–22 (2008).
DOI: 10.1016/j.jpowsour.2007.10.017

[22] Higuchi A., Agatsuma T., Uemiya S., Kojima T., Mizoguchi K., Pinnau I., Nagai K., Freeman B. D.: Preparation and gas permeation of immobilized fullerene membranes. Journal of Applied Polymer Science, **77**, 529–537 (2000).
DOI: 10.1002/(SICI)1097-4628(20000718)77:3<529::AID-APP8>3.0.CO;2-Y

[23] Cong H., Zhang J., Radosz M., Shen Y.: Carbon nanotube composite membranes of brominated poly(2,6-diphenyl-1,4-phenylene oxide) for gas separation. Journal of Membrane Science, **294**, 178–185 (2007).
DOI: 10.1016/j.memsci.2007.02.035

[24] Qiu S., Wu L., Pan X., Zhang L., Chen H., Gao C.: Preparation and properties of functionalized carbon nanotube/PSF blend ultrafiltration membranes. Journal of Membrane Science, **342**, 165–172 (2009).
DOI: 10.1016/j.memsci.2009.06.041

[25] Aerts P., Kuypers S., Genné I., Leysen R., Mewis J., Vankelecom I. F. J., Jacobs P. A.: Polysulfone–ZrO_2 surface interactions. The influence on formation, morphology and properties of zirfon-membranes. The Journal of Physical Chemistry B, **110**, 7425–7430 (2006).
DOI: 10.1021/jp053976c

[26] Razmjou A., Mansouri J., Chen V.: The effects of mechanical and chemical modification of TiO_2 nanoparticles on the surface chemistry, structure and fouling performance of PES ultrafiltration membranes. Journal of Membrane Science, **378**, 73–84 (2011).
DOI: 10.1016/j.memsci.2010.10.019

[27] Oh S. J., Kim N., Lee Y. T.: Preparation and characterization of PVDF/TiO_2 organic–inorganic composite membranes for fouling resistance improvement. Journal of Membrane Science, **345**, 13–20 (2009).
DOI: 10.1016/j.memsci.2009.08.003

[28] Polotskaya G. A., Penkova A. V., Toikka A. M.: Fullerene-containing polyphenylene oxide membranes for pervaporation. Desalination, **200**, 400–402 (2006).
DOI: 10.1016/j.desal.2006.03.347

[29] Polotskaya G. A., Gladchenko S. V., Zgonnik V. N.: Gas diffusion and dielectric studies of polystyrene-fullerene compositions. Journal of Applied Polymer Science, **85**, 2946–2951 (2002).
DOI: 10.1002/app.10906

[30] Penkova A. V., Polotskaya G. A., Toikka A. M., Trchová M., Šlouf M., Urbanová M., Brus J., Brožová L., Pientka Z.: Structure and pervaporation properties of poly(phenylene-*iso*-phthalamide) membranes modified by fullerene C_{60}. Macromolecular Materials and Engineering, **294**, 432–440 (2009).
DOI: 10.1002/mame.200800362

[31] Polotskaya G., Biryulin Yu., Rozanov V.: Asymmetric membranes based on fullerene-containing polyphenylene oxide. Fullerenes, Nanotubes and Carbon Nanostructures, **12**, 371–376 (2004).
DOI: 10.1081/FST-120027221

[32] Jin X., Hu J. Y., Tint M. L., Ong S. L., Biryulin Y., Polotskaya G.: Estrogenic compounds removal by fullerene-containing membranes. Desalination, **214**, 83–90 (2007).
DOI: 10.1016/j.desal.2006.10.019

[33] Penkova A., Toikka A., Kostereva T., Sudareva N., Polotskaya G.: Structure and transport properties of fullerene–polyamide membranes. Fullerenes, Nanotubes and Carbon Nanostructures, **16**, 666–669 (2008).
DOI: 10.1080/15363830802314251

[34] Polotskaya G. A., Pen'kova A. V., Sudareva N. N., Polotskii A. E., Toikka A. M.: Polyamide ultrafiltration membranes modified with nanocarbon additives. Russian Journal of Applied Chemistry, **81**, 236–240 (2008).
DOI: 10.1134/S1070427208020146

[35] Stein R. S., Wilson P. R.: Scattering of light by polymer films possessing correlated orientation fluctuations. Journal of Applied Physics, **33**, 1914–1922 (1962).
DOI: 10.1063/1.1728869

[36] Sabaneeva N. V., Kalinina N. A., Silinskaya I. G.: Polarized light scattering and supermolecular order in dilute polymer solutions. Polymer Science Series B, **37**, 549–551 (1995).

[37] Vinogradova L. V., Melenevskaya E. Yu., Khachaturov A. S., Kever E. E., Litvinova L. S., Novokreshchenova A. V., Sushko M. A., Klenin S. I., Zgonnik V. N.: Water-soluble complexes of C_{60} fullerene with poly(N-vinylpyrrolidone). Polymer Science Series A, **40**, 1154–1159 (1998).

[38] Wang C., Guo Z-X., Fu S., Wu W., Zhu D.: Polymers containing fullerene or carbon nanotube structures. Progress in Polymer Science, **29**, 1079–1141 (2004).
DOI: 10.1016/j.progpolymsci.2004.08.001

[39] Kallistov O. V., Silinskaya I. G.: Novel parameter characterizing supermolecular order in macroisotropic polymer systems. Polymer Science, **34**, 557–558 (1992).

[40] Eskin V. E.: Light scattering by polymer solutions and macromolecular properties (in Russian). Nauka, Leningrad (1986).

[41] Mulder M. H. V.: Phase inversion membranes. in 'Membrane preparation' (ed.: Mulder M. H. V.) Academic Press, New York, 3331–3346 (2000).

[42] Nunes S. P., Peinemann K-V.: Membrane preparation. in 'Membrane technology in the chemical industry' (eds.: Nunes S. P., Peinemann K-V.) Wiley-VCH, Weinheim, 6–11 (2001).

[43] Cherkasov A. N.: Ultrafiltration mechanism of solutions selective separation (in Russian). Kolloid Journal, **47**, 363–368 (1985).

[44] Bhardwaj V., Macintosh A., Sharpe I. D., Gordeev S. A., Shilton S. J.: Polysulfone hollow fiber gas separation membranes filled with submicron particles. Annals of New York Academy of Sciences, **984**, 318–328 (2003).
DOI: 10.1111/j.1749-6632.2003.tb06009.x

[45] Baker R. W.: Membrane technology and applications. Wiley, Chichester (2004).

[46] Zularisam A. W., Ismail A. F., Salim M. R., Sakinah M., Ozaki H.: The effects of natural organic matter (NOM) fractions on fouling characteristics and flux recovery of ultrafiltration membranes. Desalination, **212**, 191–208 (2007).
DOI: 10.1016/j.desal.2006.10.010

[47] Chan R., Chen V., Bucknall M. P.: Quantitative analysis of membrane fouling by protein mixtures using MALDI-MS. Biotechnology and Bioengineering, **85**, 190–201 (2003).
DOI: 10.1002/bit.10866

[48] Kwon B., Molek J., Zydney A. L.: Ultrafiltration of PEGylated proteins: Fouling and concentration polarization effects. Journal of Membrane Science, **319**, 206– 213 (2008).
DOI: 10.1016/j.memsci.2008.03.035

[49] Huisman I. H., Prádanos P., Hernández A.: The effect of protein–protein and protein–membrane interactions on membrane fouling in ultrafiltration. Journal of Membrane Science, **179**, 79–90 (2000).
DOI: 10.1016/S0376-7388(00)00501-9

[50] Ma X., Su Y., Sun Q., Wang Y., Jiang Z.: Preparation of protein-adsorption-resistant polyethersulfone ultrafiltration membranes through surface segregation of amphiphilic comb copolymer. Journal of Membrane Science, **292**, 116–124 (2007).
DOI: 10.1016/j.memsci.2007.01.024

eXPRESS Polymer Letters Vol.6, No.3 (2012) 189–197
Available online at www.expresspolymlett.com
DOI: 10.3144/expresspolymlett.2012.21

Influence of the ionic character of a drug on its release rate from hydrogels based on 2-hydroxyethylmethacrylate and acrylamide synthesized by photopolymerization

M. L. Gómez[1]*, *R. J. J. Williams*[2], *H. A. Montejano*[1], *C. M. Previtali*[1]

[1]Departamento de Química, Universidad Nacional de Río Cuarto y CONICET, Campus Universitario, 5800 Río Cuarto, Argentina
[2]Institute of Materials Science and Technology (INTEMA), University of Mar del Plata and National Research Council (CONICET), J. B. Justo 4302, 7600 Mar del Plata, Argentina

Received 11 July 2011; accepted in revised form 24 September 2011

Abstract. The influence of the ionic character of a specific drug on its release rate from a hydrogel based on 2-hydroxyethylmethacrylate (HEMA) and acrylamide (AAm) is analyzed. The hydrogel was synthesized by photopolymerization employing visible light, safranine O (Saf), as sensitizer, and a silsesquioxane functionalized with amine and methacrylate groups (SFMA), as co-initiator and crosslinker. Safranine O (Saf) was employed as a model of a cationic drug and the anionic form of resorufin (Rf) as a model of an anionic drug. Saf exhibited a larger affinity with functional groups of the hydrogel than that of Rf. This produced a lower loading and a faster release rate of Rf with respect to Saf. Besides, the release rate of Rf followed a Fickian behavior, while that of Saf exhibited a non-Fickian behavior. By hydrolyzing the hydrogel at pH = 13, amide groups supplied by AAm were irreversibly converted into carboxylic acid groups. Higher loadings and slower release rates of Saf from the hydrolyzed hydrogels were observed, making them particularly suitable for the slow drug-delivery of cationic drugs.

Keywords: *polymer gels, hydrogels, drug release, hydroxyethylmethacrylate, acrylamide*

1. Introduction

Hydrogels are crosslinked hydrophilic polymers that constitute an important class of materials in biotechnology and medicine because of their excellent biocompatibility [1–2]. Over the past three decades, a variety of hydrogels differing in structure, composition, and properties were developed [3–4]. Hydrogels exhibiting a swelling response to environmental changes such as temperature, pH, electric field, UV or visible light-radiation, solvent composition, salt concentration and type of surfactants are attracting increasing interest in various applications such as drug delivery systems, separation operations in biotechnology, processing of agricultural products, conductive or superabsorbent composites, and sensors and actuators [1, 5–7]. HEMA (2-hydroxyethylmethacrylate) was the first monomer used to synthesize hydrogels for biomedical applications [8]. Its water swelling properties are improved by co-polymerization with more hydrophilic monomers [7, 9–10].

Hydrogels may be synthesized via various polymerization techniques, such as thermal polymerization [11], oxidation-reduction (redox) polymerization [12] and photopolymerization [13–14]. Photopolymerization has several advantages over conventional polymerization techniques. These include spatial and temporal control over polymerization

---

*Corresponding author, e-mail: mlgomez@exa.unrc.edu.ar and fast curing rate at room or physiological temperatures. One major advantage of photopolymerization is that hydrogels can be synthesized in the presence of an active principle, facilitating the incorporation of drugs during the synthesis of the hydrogels. Photopolymerization has been employed to obtain hydrogels for drug delivery applications using a variety of mono functional monomers such as HEMA [7–12, 15], and crosslinkers such as poly (ethylene glycol) dimethacrylate [16], and poly(ethylene glycol) diacrylate [17]. The co-polymerization of HEMA, acrylamide (AAm) and a suitable crosslinker provides a unique combination of properties of the resulting hydrogels, making them capable of swelling especially at high pH values [18–19].

Water-soluble photoinitiator systems for vinyl polymerizations, above all those active in the visible region of the spectrum, have gained increasing interest in recent years [20]. Among them, the most commonly employed photoinitiators are those generating radicals by a bimolecular process comprising an excited state of a synthetic dye or natural pigment, and a co-initiator that behaves as electron donor. Particularly, safranine O, an azine dye, was extensively studied for its use as sensitizer of photopolymerization in organic and aqueous media employing visible light as energy source and different amines as co-initiators [21–24].

In a previous study we reported the synthesis of a silsesquioxane functionalized with methacrylate and amine groups (SFMA) that was employed as crosslinker/co-initiator to obtain poly(HEMA-*co*-AAm) hydrogels by visible-light photopolymerization, employing safranine O (Saf) as sensitizer [19]. The swelling behavior of the poly(HEMA-*co*-AAm) hydrogels at different pHs was also reported [19]. The present study focuses on the way in which the release rate of a specific compound retained inside the poly(HEMA-*co*-AAm) hydrogel is affected by the ionic character of the active species, using dyes as model drugs. Two dyes were used: safranine-O (Saf) as an axample of a cationic active group and resorufin (Rf) as an example of an anionic active group. While Saf is a strong base, resorufin is an acid with a $pKa = 7.9$. A significant fraction of Saf persists in its cationic form even at high values of pH. This is not the case for Rf, where the fraction of the conjugated base (anion) is very low at low values of pH. Therefore, experimental results with Rf were obtained at pH = 7.

The influence of pH and temperature on the release rate of dyes and drugs from specific hydrogels (including those based on HEMA) has been reported in a large number of papers [e.g., 7, 15, 25–40]. However, to the best of our knowledge there are no comparative studies of the release rate of salts with large ions and small counterions from a specific hydrogel under defined pH and temperature conditions. This is an important concept because several drugs are used as salts. The following are examples of release rate studies of cationic drugs: pralidoxime chloride [28], salbutamol sulfate [30], gentamicin sulfate [25], and anionic drugs: sodium sulfacetamide [25]. We employed safranine (Saf) as a model of a cationic drug and the anionic form of resorufin (Rf) as a model of an anionic drug.

The election of poly(HEMA-*co*-AAm) hydrogels for this study was based on two facts: a) this is a classic system for drug delivery studies, b) they can be hydrolyzed at pH = 13 to irreversibly transform their amide functionalities into carboxylate groups [19], a possibility that can be used to compare the behavior of poly(HEMA-*co*-AAm) and poly(HEMA-*co*-AA) hydrogels of the same composition.

2. Experimental

2.1. Materials

The silsesquioxane functionalized with methacrylate and amine groups (SFMA) was synthesized as described in a previous paper [19]. Acrylamide (AAm – Code: A8887 – Assay ≥99%) and 2-hydroxyethylmethacrylate (HEMA – Code: 128635 – Assay: 97%) were provided by Aldrich, Steinheim, Germany and used as received. Safranine O (Saf – Code: S2255) and the anionic form of resorufin (Rf – Code: R3257) were purchased from Aldrich, Steinheim, Germany and employed without further purification. Water was purified through a Millipore Milli-Q system. Buffer solutions were provided by Laboratorios Oliveri, Buenos Aires, Argentina and used as received. The structures of a representative molecule of SFMA, monomers and dyes are presented in Figure 1.

2.2. Synthesis of hydrogels

Hydrogels were synthesized employing the following proportions of monomers by weight: HEMA

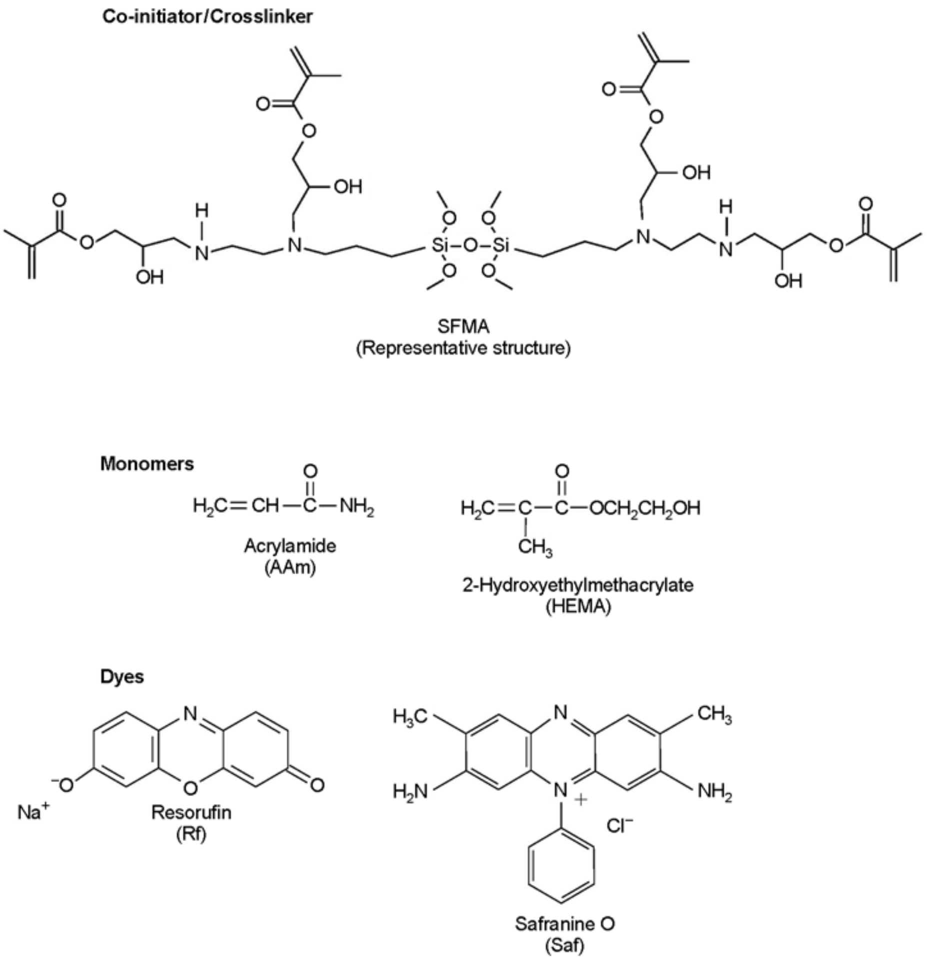

Figure 1. Structures of SFMA, monomers and model drugs

90%, AAm 9% and photoinitiator/crosslinker 1%. The photoinitiator/crosslinker was composed of Saf/SFMA in similar proportions as in our previous study [19]. Typically, 2 mL of a deaerated aqueous solution (50 by volume) of this formulation was irradiated for 2 h in a homemade merry-go-round photochemical reactor supplied with eight green LEDs (λ_{max} = 530 nm).

2.3. Swelling

Uniform disks, 10.5 mm diameter and 2.5 mm thickness, were cut from the hydrogels and immersed in Milli-Q water to remove unreacted monomers, Saf and SFMA; water was daily replaced for one week. After this period hydrogels were washed with Milli-Q water and dried in a vacuum oven at 37°C for 48 h. Dried disks were weighed (W_{pol}) and immersed in commercial buffer solutions at room temperature. At specified times samples were removed from the solutions, blotted with filter paper to eliminate excess of solution and weighed (W_t). Three samples were used per point of the swelling curve. The degree of swelling (S_w) was calculated accoding to Equation (1):

$$S_w = \frac{W_t - W_{pol}}{W_{pol}} = \frac{W_{water}}{W_{pol}} \tag{1}$$

To visualize the pore structure of the hydrogels in the swollen state, a JEOL JSM-6460 LV SEM, from Jeol Technics Ltd., Tokyo, Japan was employed. Samples were swollen to equilibrium in buffer solutions, blotted with filter paper, frozen at –18ºC and freeze-dried for 24 h in a Virtis Benchtop SLC, SP Industries, New York, USA. Freeze-dried samples were loaded on the surface of an aluminum SEM specimen holder and sputter coated with Au-Pd for 35 s before observation. A working distance about 20–25 mm, an accelerating voltage of 15 kV, and a chamber pressure of 10^{-9} Torr were found to be suitable for obtaining high-resolution images.

2.4. Loading and release of dyes

Disks of dried hydrogels were immersed for 24 h in aqueous solutions of the dyes with a concentration giving a maximum value of absorbance equal to 1.2, measured with an optical path of 1 cm. Disks were removed from the solution and dried under vacuum at 37°C for 48 h. The amount of dye that was loaded was determined from the residual absorbance of the solution employing a calibration curve following Lambert-Beer's law. UV-vis spectra were recorded with an Agilent 8453 diode array spectrophotometer, Waldbronn, Germany. Samples were placed in a 1 cm × 1 cm × 3 cm quartz cell and spectra recorded at room temperature.

Release experiments were carried out by transferring the dried dye-loaded disks into 10 mL buffer solutions of different pHs at room temperature. At specified time intervals, 3 mL aliquots were removed from every solution (three aliquots of different solutions for any single point of the release curve), and their absorbance determined by ultraviolet-visible (UV-vis) spectroscopy at the maximum absorption wavelength of each dye. After measuring the absorbance, aliquots were returned to the original solutions to keep volume constant. Calibration curves were used to transform absorbance determinations into concentrations.

3. Results and discussion

3.1. Swelling behavior of hydrogels

The swelling of the hydrogel in water at different pH values can be related to its behavior as a drug-delivery material. Preliminary swelling results of the synthesized hydrogels were reported in our previous study [19]. A significant increase in the swelling capacity was observed at pH 13, explained by the almost complete conversion of acrylamide into carboxylate groups [19]. The repulsion of the anionic groups fixed in the gel structure and the increase in hydrophilicity produced by the presence of ionic species inside the gel led to an increase in swelling. Morphologies of hydrogels swollen at different pH values are shown in Figure 2 (although SEM is useful to reveal the hydrogel structure, care must be taken to avoid affecting the morphology during sample preparation [41]).

The hydrogel swollen at pH = 2 shows a compact and collapsed structure with few pores of about 10 µm diameter (Figure 2A). The material swollen at pH = 7 (Figure 2B) shows a distribution of pores with an average diameter close to 10 µm. The hydrogel swollen at pH = 13 (Figure 2C) presents larger pores (diameters higher than 20 µm) and thinner walls, in agreement with its high swelling capacity. Based on these results it was considered of interest to compare the behavior of non-hydrolyzed hydrogels,

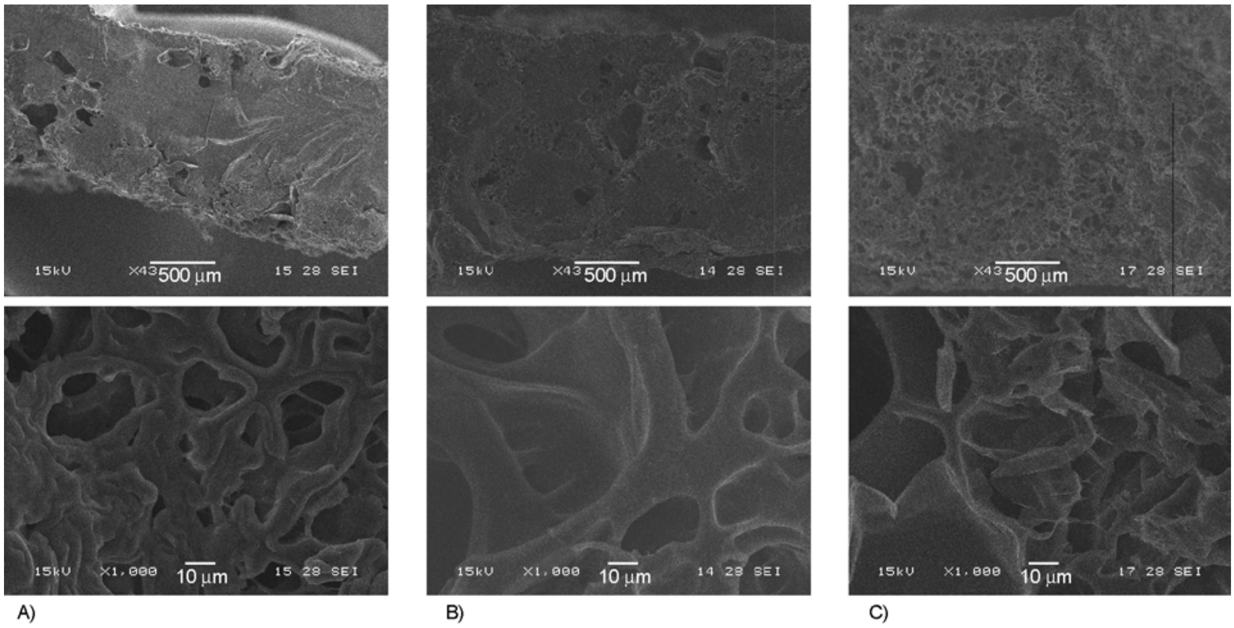

Figure 2. SEM micrographs of freeze-dried hydrogels after reaching equilibrium at: A) pH = 2, B) pH = 7 and C) pH =13

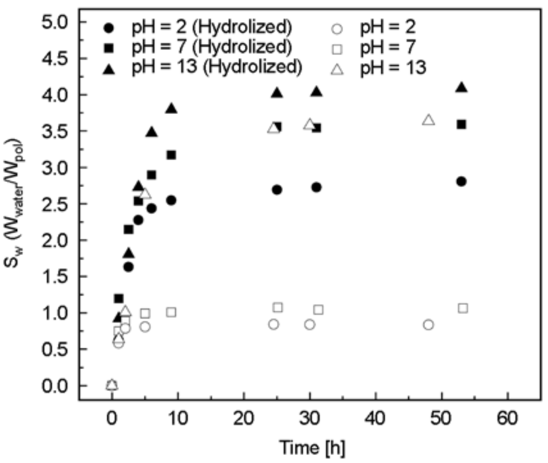

Figure 3. Swelling of hydrolyzed and non-hydrolyzed hydrogels at pH = 2, 7 and 13

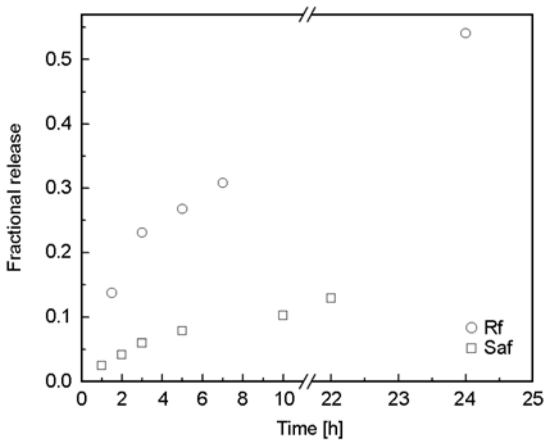

Figure 4. Fractional release of Rf and Saf at pH = 7 from non-hydrolyzed hydrogels

poly(HEMA-*co*-AAm), and hydrolyzed hydrogels, poly(HEMA-*co*-AA), obtained by immersing the non-hydrolyzed hydrogels in a buffer solution of pH = 13 for 48 h, followed by a water extraction and drying procedure similar to the one used for the non-hydrolyzed hydrogels described in the experimental section.

A comparison of the swelling behavior of hydrolyzed and non-hydrolyzed hydrogels at different pHs is shown in Figure 3. In hydrolyzed hydrogels amide groups were converted to carboxylic acid groups [19, 42–45] whose degree of ionization depends on the pH of the swelling test. The particular curve obtained for the non-hydrolyzed gel at pH = 13 should not be considered for the discussion because partial conversion of amide to carboxylate groups takes place during the swelling test. Hydrolyzed hydrogels exhibited a larger swelling capacity than non-hydrolyzed hydrogels at any pH. This can be ascribed to the higher hydrophilicity of carboxylic acid groups compared to amide groups and their partial ionization when increasing pH.

3.2. Release of dyes from non-hydrolyzed hydrogels

After 24 h immersion in a water solution of a particular dye, the amount that was loaded to the hydrogel (defined as M_∞ in mass per unit mass of polymer), was M_∞ (Saf) = 42 mg/g and M_∞ (Rf) = 5 mg/g. The significant loading observed for Saf evidences the presence of specific electrostatic interactions between the cation and functional groups of the hydrogel. This also causes a significant slower release rate of Saf with respect to Rf as is shown in Figure 4 for pH = 7. The cumulative fractional release of Saf and Rf, M_t/M_∞, in a buffer medium at pH = 7 are shown in Figure 4. Therefore, the poly (HEMA-*co*-AAm) hydrogel might be suitable for the loading and slow release of cationic drugs.

An empiric equation developed by Peppas and coworkers for the release rate assumes a time-dependent power law function [46–47] presented in Equation (2):

$$\frac{M_\mathrm{t}}{M_\infty} = kt^\mathrm{n} \qquad (2)$$

The fitting of experimental results with Equation (2) written in logarithmic form is shown in Figure 5. The resulting parameters are summarized in Table 1. When the value of the exponent is $n = 0.5$, the release rate follows Fick's law. Within experimental error the release rate of the anionic dye follows a

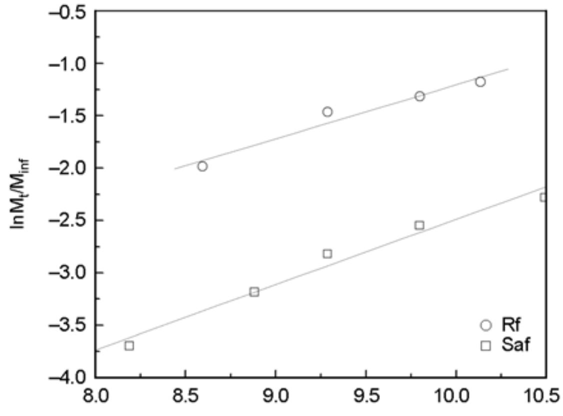

Figure 5. Logarithmic expression of the fractional release of Rf and Saf at pH = 7 from non-hydrolyzed hydrogels against natural logarithm of time expressed in seconds

Table 1. Release characteristics of model drugs from poly(HEMA-co-AAm) hydrogels

Drug	k [h^{-n}]	n	R	D [$cm^2 \cdot s^{-1}$]
Rf	$1.74 \cdot 10^{-3}$	0.52	0.978	$1.98 \cdot 10^{-8}$
Saf	$1.63 \cdot 10^{-4}$	0.62	0.987	–

Fickian behavior while the cationic dye exhibits a non-Fickian mechanism. The departure from Fick's law can again be explained by the presence of electrostatic interactions between the positive charge of Saf and functional groups of the hydrogel. Similar results were observed for crystal violet when it was employed as model drug in poly(HEMA-*co*-AA) hydrogels [7]. The non-Fickian mechanism was ascribed to electrostatic interactions between the positive charge of the dye with carboxylic groups of the hydrogel [7].

For systems following a Fickian behavior, diffusion coefficients (D) may be calculated from the slope of the plot of M_t/M_∞ *vs*. $t^{1/2}$ (the initial slope is equal to $4D^{1/2}/(\pi^{1/2}L)$, where L is the slab thickness [25]). The diffusion coefficient of Rf reported in Table 1 lies in the same range as some of the values reported in the literature [25, 32].

3.3. Release of Saf from a hydrolyzed hydrogel

The possibility of varying the specific interactions of Saf by converting amide groups into carboxylic acid groups was investigated. It was found that the value of M_∞ increased from 42 mg/g for the non-hydrolyzed hydrogel to 80 mg/g for the hydrolyzed hydrogel, implying that carboxylic acid groups promoted higher specific interactions with Saf than amide groups. This was confirmed by comparing release rates of Saf from hydrolyzed and non-hydrolyzed hydrogels at pH 2, 7 and 13 (Figure 6). Again the partial conversion of amide to carboxylate groups, that takes place during the swelling test, must be considered for the curves at pH = 13.

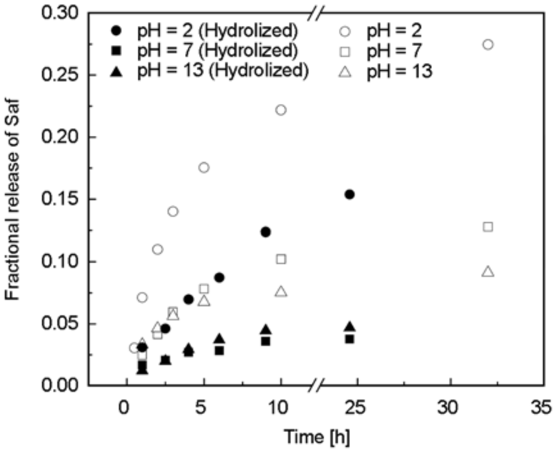

Figure 6. Fractional release of Saf for hydrolyzed and non-hydrolyzed hydrogels at pH = 2, 7 and 13

For both types of hydrogels release rates were higher under acid conditions where the lowest swelling had been observed. This means that release rate depends more on specific interactions of the dye with the functional groups of the gel than on the swelling of the materials. Specific interactions between Saf and carboxylic acid groups should be stronger than the ones of Saf and acrylamide groups as evidenced by the significant decrease of the fractional release rate observed for hydrolyzed hydrogels at all pH values. This agrees with the higher loading capacity for Saf exhibited by hydrolyzed hydrogels. Specific interactions should decrease their strength under acid conditions to explain the highest release rate observed at pH = 2. This means that specific interactions of Saf should decrease in the sequence $COO^- > COOH > CONH_2$. Poly(HEMA-*co*-AA) hydrogels are therefore suitable for the very slow release of a cationic drug, particularly under neutral or alkaline pH values.

4. Conclusions

In conclusion, we showed that tuning the ionic character of a drug and the conversion of amide groups into carboxylate groups enables to control the loading capacity and the release rate from poly(HEMA-*co*-AAm) hydrogels used in drug-delivery applications. These hydrogels are more affine with cationic than with anionic drugs. This leads to a higher loading capacity and a slower release rate of cationic dyes with respect to anionic dyes. Conversion of the hydrogel to poly(HEMA-*co*-AA) by hydrolysis at pH = 13, produced a significant increase in swelling and loading capacity and a decrease of the release rate, particularly under neutral or alkaline conditions. This means that specific interactions of the cationic dye decrease in the sequence $COO^- > COOH > CONH_2$.

Acknowledgements

The financial support of Universidad Nacional de Mar del Plata, Universidad Nacional de Río Cuarto, CONICET and ANPCyT (PICT 07-346), Argentina, is gratefully acknowledged.

References

[1] Hoffman A. S.: Applications of thermally reversible polymers and hydrogels in therapeutics and diagnostics. Journal of Controlled Release, **6**, 297–305 (1987). DOI: 10.1016/0168-3659(87)90083-6

[2] Peppas N. A., Hilt J. Z., Khademhosseini A., Langer R.: Hydrogels in biology and medicine: From molecular principles to bionanotechnology. Advanced Materials, **18**, 1345–1360 (2006). DOI: 10.1002/adma.200501612

[3] Peppas N. A.: Hydrogels in medicine and pharmacy. CRC Press, Boca Raton (1987).

[4] Oh J. K., Drumright R., Siegwart D. J., Matyjaszewski K.: The development of microgels/nanogels for drug delivery applications. Progress in Polymer Science, **33**, 448–477 (2008). DOI: 10.1016/j.progpolymsci.2008.01.002

[5] Tanaka T., Filmore D. J.: Kinetics of swelling of gels. Journal of Chemical Physics, **70**, 1214–1218 (1979). DOI: 10.1063/1.437602

[6] Tang Q., Wu J., Lin J., Li Q., Fan S.: Two-step synthesis of polyacrylamide/polyacrylate interpenetrating network hydrogels and its swelling/deswelling properties. Journal of Materials Science, **43**, 5884–5890 (2008). DOI: 10.1007/s10853-008-2857-x

[7] Yue Y., Sheng X., Wang P.: Fabrication and characterization of microstructured and pH sensitive interpenetrating networks hydrogel films and application in drug delivery field. European Polymer Journal, **45**, 309–315 (2009). DOI: 10.1016/j.eurpolymj.2008.10.038

[8] Wichterle O., Lim D.: Hydrophilic gels for biological use. Nature, **185**, 117–118 (1960). DOI: 10.1038/185117a0

[9] Kabra B. G., Gehrke S. H., Hwang S. T., Ritschel W. A.: Modification of the dynamic swelling behavior of poly(2-hydroxyethyl methacrylate) in water. Journal of Applied Polymer Science, **42**, 2409–2416 (1991). DOI: 10.1002/app.1991.070420906

[10] Wang J., Wu W.: Swelling behaviors, tensile properties and thermodynamic studies of water sorption of 2-hydroxyethyl methacrylate/epoxy methacrylate copolymeric hydrogels. European Polymer Journal, **41**, 1143–1151 (2005). DOI: 10.1016/j.eurpolymj.2004.11.034

[11] Huang C-W., Sun Y-M., Huang W-F.: Curing kinetics of the synthesis of poly(2-hydroxyethyl methacrylate) (PHEMA) with ethylene glycol dimethacrylate (EGDMA) as a crosslinking agent. Journal of Polymer Science Part A: Polymer Chemistry, **35**, 1873–1889 (1997). DOI: 10.1002/(SICI)1099-0518(19970730)35:10<1873::AID-POLA2>3.0.CO;2-P

[12] Podual K., Doyle III F. J., Peppas N. A.: Dynamic behavior of glucose oxidase-containing microparticles of poly(ethylene glycol)-grafted cationic hydrogels in an environment of changing pH. Biomaterials, **21**, 1439–1450 (2000). DOI: 10.1016/S0142-9612(00)00020-X

[13] Anseth K. S., Scott R. A., Peppas N. A.: Effects of ionization on the reaction behavior and kinetics of acrylic acid polymerizations. Macromolecules, **29**, 8308–8312 (1996). DOI: 10.1021/ma960840r

[14] Li L., Lee L. J.: Photopolymerization of HEMA/DEGDMA hydrogels in solution. Polymer, **46**, 11540–11547 (2005). DOI: 10.1016/j.polymer.2005.10.051

[15] Lu S., Anseth K. S.: Photopolymerization of multilaminated poly(HEMA) hydrogels for controlled release. Journal of Controlled Release, **57**, 291–300 (1999). DOI: 10.1016/S0168-3659(98)00125-4

[16] Bryant S. J., Anseth K. S.: The effects of scaffold thickness on tissue engineered cartilage in photocrosslinked poly(ethylene oxide) hydrogels. Biomaterials, **22**, 619–626 (2001). DOI: 10.1016/S0142-9612(00)00225-8

[17] Burdick J. A., Anseth K. S.: Photoencapsulation of osteoblasts in injectable RGD-modified PEG hydrogels for bone tissue engineering. Biomaterials, **23**, 4315–4323 (2002). DOI: 10.1016/S0142-9612(02)00176-X

[18] Nizam El-Din H. M., El-Naggar A. W. M.: Synthesis and characterization of hydroxyethyl methacrylate/acrylamide responsive hydrogels. Journal of Applied Polymer Science, **95**, 1105–1115 (2005). DOI: 10.1002/app.21326

[19] Gómez M. L., Fasce D. P., Williams R. J. J., Erra-Balsells R., Fatema M. K., Nonami H.: Silsesquioxane functionalized with methacrylate and amine groups as a crosslinker/co-initiator for the synthesis of hydrogels by visible-light photopolymerization. Polymer, **49**, 3648–3653 (2008). DOI: 10.1016/j.polymer.2008.07.001

[20] Salomone J. C.: Polymeric materials encyclopedia, Vol 7. CRC press, Boca Raton (1996).

[21] Encinas M. V., Rufs A. M., Neumann M. G., Previtali C. M.: Photoinitiated vinyl polymerization by safranine T/triethanolamine in aqueous solution. Polymer, **37**, 1395–1398 (1996). DOI: 10.1016/0032-3861(96)81137-2

[22] Encinas M. V., Previtali C. M., Gehlen M. H., Neumann M. G.: The interaction of aliphatic amines with safranine T in aqueous solution. Journal of Photochemistry and Photobiology A: Chemistry, **94**, 237–241 (1996). DOI: 10.1016/1010-6030(95)04218-0

[23] Previtali C. M., Bertolotti S. G., Neumann M. G., Pastre I. A., Rufs A. M., Encinas M. V.: Laser flash photolysis study of the photoinitiator system safranine T-aliphatic amines for vinyl polymerization. Macromolecules, **27**, 7454–7458 (1994).
DOI: 10.1021/ma00103a031

[24] Gómez M. L., Avila V., Montejano H. A., Previtali C. M.: A mechanistic and laser flash photolysis investigation of acrylamide polymerization photoinitiated by the three component system safranine-T/triethanolamine/diphenyliodonium chloride. Polymer, **44**, 2875–2881 (2003).
DOI: 10.1016/S0032-3861(03)00212-X

[25] Tomić S. L., Dimitrijević S. I., Marinković A. D., Najman S., Filipović J. M.: Synthesis and characterization of poly(2-hydroxyethyl methacrylate/itaconic acid) copolymeric hydrogels. Polymer Bulletin, **63**, 837–851 (2009).
DOI: 10.1007/s00289-009-0123-2

[26] Moogooee M., Ramezanzadeh H., Jasoori S., Omidi Y., Davaran S.: Synthesis and in vitro studies of cross-linked hydrogel nanoparticles containing amoxicillin. Journal of Pharmaceutical Sciences, **100**, 1057–1066 (2011).
DOI: 10.1002/jps.22351

[27] Abd Alla S. G., Nizam El-Din H. M., El-Naggar A. W. M.: Structure and swelling-release behaviour of poly (vinyl pyrrolidone) (PVP) and acrylic acid (AAc) copolymer hydrogels prepared by gamma irradiation. European Polymer Journal, **43**, 2987–2998 (2007).
DOI: 10.1016/j.eurpolymj.2007.04.016

[28] Agarwal S., Sumana G., Gupta D. C.: Poly (2-hydroxyethyl methacrylate)-based hydrogels for slow release of pralidoxime chloride. Journal of Applied Polymer Science, **66**, 267–270 (1997).
DOI: 10.1002/(SICI)1097-4628(19971010)66:2<267::AID-APP7>3.0.CO;2-U

[29] Sastre R. L., Blanco M. D., Gómez C., del Socorro J. M., Teijón J. M.: Cytarabine trapping in poly(2-hydroxyethyl methacrylate-*co*-acrylamide) hydrogels: Drug delivery studies. Polymer International, **48**, 843–850 (1999).
DOI: 10.1002/(SICI)1097-0126(199909)48:9<843::AID-PI225>3.0.CO;2-8

[30] Suhag G. S., Bhatnagar A., Singh H.: Poly(hydroxyethyl methacrylate)-based co-polymeric hydrogels for transdermal delivery of salbutamol sulphate. Journal of Biomaterials Science, Polymer Edition, **19**, 1189–1200 (2008).
DOI: 10.1163/156856208785540118

[31] Xu J., Li X., Sun F.: Cyclodextrin-containing hydrogels for contact lenses as a platform for drug incorporation and release. Acta Biomaterialia, **6**, 486–493 (2010).
DOI: 10.1016/j.actbio.2009.07.021

[32] Kalagasidis Krušić M., Ilić M., Filipović J.: Swelling behavior and paracetamol release from poly(*N*-isopropylacrylamide-itaconic acid) hydrogels. Polymer Bulletin, **63**, 197–211 (2009).
DOI: 10.1007/s00289-009-0086-3

[33] Krishna Rao K. S. V., Ha C. S.: pH sensitive hydrogels based on acryl amides and their swelling and diffusion characteristics with drug delivery behavior. Polymer Bulletin, **62**, 167–181 (2009).
DOI: 10.1007/s00289-008-0011-1

[34] Harling S., Schwoerer A., Scheibe K., Daniels R., Menzel H.: A new hydrogel drug delivery system based on hydroxyethylstarch derivatives. Journal of Microencapsulation, **27**, 400–408 (2010).
DOI: 10.3109/02652040903367301

[35] García D. M., Escobar J. L., Noa Y., Bada N., Hernáez E., Katime I.: Timolol maleate release from pH-sensible poly(2-hydroxyethyl methacrylate-co-methacrylic acid) hydrogels. European Polymer Journal, **40**, 1683–1690 (2004).
DOI: 10.1016/j.eurpolymj.2004.03.012

[36] García O., Blanco M. D., Martín J. A., Teijón J. M.: 5-fluorouracil trapping in poly(2-hydroxyethyl methacrylate-co-acrylamide) hydrogels: In vitro drug delivery studies. European Polymer Journal, **36**, 111–122 (2000).
DOI: 10.1016/S0014-3057(99)00037-3

[37] Qiu Y., Park K.: Environment-sensitive hydrogels for drug delivery. Advanced Drug Delivery Reviews, **53**, 321–339 (2001).
DOI: 10.1016/S0169-409X(01)00203-4

[38] Lin G., Chang S., Kuo C-H., Magda J., Solzbacher F.: Free swelling and confined smart hydrogels for applications in chemomechanical sensors for physiological monitoring. Sensors and Actuators B: Chemical, **136**, 186–195 (2009).
DOI: 10.1016/j.snb.2008.11.001

[39] Liu F., Urban M. W.: Recent advances and challenges in designing stimuli-responsive polymers. Progress in Polymer Science, **35**, 3–23 (2010).
DOI: 10.1016/j.progpolymsci.2009.10.002

[40] Wang J., Gao P., Ye L., Zhang A-Y., Feng Z-G.: Dual thermo-responsive polyrotaxane-based triblock copolymers synthesized via ATRP of N-isopropylacrylamide initiated with self-assemblies of Br end-capped Pluronic F127 with β-cyclodextrins. Polymer Chemistry, **2**, 931–940 (2011).
DOI: 10.1039/C0PY00360C

[41] Hong P-D., Chen J-H.: Network structure and chain mobility of freeze-dried polyvinyl chloride/dioxane gels. Polymer, **39**, 5809–5817 (1998).
DOI: 10.1016/S0032-3861(98)00031-7

[42] Lee W-F., Shieh C-H.: pH-thermoreversible hydrogels. I. Synthesis and swelling behaviors of the (*N*-isopropylacrylamide-*co*-acrylamide-*co*-2-hydroxyethyl methacrylate) copolymeric hydrogels. Journal of Applied Polymer Science, **71**, 221–231 (1999).
DOI: 10.1002/(SICI)1097-4628(19990110)71:2<221::AID-APP5>3.0.CO;2-W

[43] Kizilay M. Y., Okay O.: Effect of hydrolysis on spatial inhomogeneity in poly(acrylamide) gels of various crosslink densities. Polymer, **44**, 5239–5250 (2003).
DOI: 10.1016/S0032-3861(03)00494-4

[44] Pourjavadi A., Amini-Fazl M. S., Hosseinzadeh H.: Partially hydrolyzed crosslinked alginate-*graft*-polymethacrylamide as a novel biopolymer-based superabsorbent hydrogel having pH-responsive properties. Macromolecular Research, **13**, 45–53 (2005).
DOI: 10.1007/BF03219014

[45] Marandi G. B., Esfandiari K., Biranvand F., Babapour M., Sadeh S., Mahdavinia G. R.: pH sensitivity and swelling behavior of partially hydrolyzed formaldehyde-crosslinked poly(acrylamide) superabsorbent hydrogels. Journal of Applied Polymer Science, **109**, 1083–1092 (2008).
DOI: 10.1002/app.28205

[46] Peppas N. A., Bures P., Leobandung W., Ichikawa H.: Hydrogels in pharmaceutical formulations. European Journal of Pharmaceutics and Biopharmaceutics, **50**, 27–46 (2000).
DOI: 10.1016/S0939-6411(00)00090-4

[47] Siepmann J., Peppas N. A.: Mathematical modeling of controlled drug delivery. Advanced Drug Delivery Reviews, **48**, 137–138 (2001).
DOI: 10.1016/S0169-409X(01)00111-9

eXPRESS Polymer Letters Vol.6, No.3 (2012) 198–203
Available online at www.expresspolymlett.com
DOI: 10.3144/expresspolymlett.2012.22

Loading rate effects on the fracture of Ni/Au nano-coated acrylic particles

J. Y. He[1], *S. Nagao*[1], *H. Kristiansen*[2], *Z. L. Zhang*[1]*

[1]NTNU Nanomechanical Lab, Department of Structural Engineering, Norwegian University of Science and Technology (NTNU), 7491 Trondheim, Norway
[2]Conpart As, 2013 Skjetten, Norway

Received 7 July 2011; accepted in revised form 25 September 2011

Abstract. Mechanical failure of monodisperse Ni/Au coated acrylic particles has been investigated by individual compression tests using nanoindentation-based technique equipped with a flat diamond punch. We have found that both fracture property and morphology of particles depend on the compression loading rate. The breaking strain of the metal coating decreases with increasing loading rate, while the breaking stress increases. Two obvious fracture patterns with cracking in meridian or latitude direction are identified according to the loading rate, and attributed respectively to tension- or bending-dominated deformation of the coating. The findings reported here give a significant guiding to the manufacture design of metal coated polymer particles for Anisotropic Conductive Adhesive (ACA) packaging.

Keywords: *nanocomposites, nanoindentation, loading rate, mechanical properties, fracture and fatigue*

1. Introduction

Metal coated polymer particles have been increasingly used in new electronic packaging technologies, for example, Anisotropic Conductive Adhesive (ACA) [1]. As a substitute for compact metal particles, the use of such composite particles in ACA possesses a number of advantages in terms of reducing the package size, increasing the reliability of the interconnections, and developing the environmentally friendly process by replacing formerly used tin-lead solders [2]. In ACA, the electrical conductivity is established by the contact between particles and electrodes on chips/substrates. A sufficient contact area is preferred to achieve a low resistance connection; thus a large deformation of particles is required although an excess deformation of particles may cause a significant impact to the electrical property. How the metal coated polymer particles behave under such large deformation is a key issue for the ACA performance. This consideration has motivated us to study the fracture property of the metal coated polymer particles undergoing large deformation.

The metal coated polymer particle used in ACA typically consists of a monodisperse micron-sized polymer core ranged from 3 to 10 μm for improving contact compliance, a nanoscale Ni inner layer for developing electrical conductivity and yielding adhesion to the polymer core, and a nanoscale Au outer layer for protecting inner layer from the oxidation and hence enhancing contact reliability and efficiency [3, 4]. Most of studies in this field exist related to the preparation and the plating process of metal coated polymer particles [5–7]. The literature concerning mechanical properties of nanostructured composite particles is relatively sparse. However, mechanical characterization of single micron-sized particles has to cope with the challenges of

---

*Corresponding author, e-mail: zhiliang.zhang@ntnu.no

small volume, spherical geometry, composite structure and large deformation. A nanoindentation-based flat punch method has been developed to measure mechanical properties of single micron-sized polymer particles by the authors [8–11]. In a previous study, we have identified a three-stage deformation process of single Ni/Au coated acrylic particles under compression [12]. Subject to a compression stress, the Ni/Au coated acrylic particles shows failure including the rupture of the metal coating at a critical deformation and the collapse of the polymer core at a considerably larger deformation. Due to the viscoelasticity of the polymer core, the deformation behaviour of particles is rate dependent [13–15]. Moreover, the adhesion between the metal coating and the polymer core is influenced by the loading rate because of the substantial difference between the deformation resistance of metal and polymer to the external stress. Therefore the rate sensitivity of the particle behaviour is critical for the use of particles in ACA. The aim of this study is to reveal fracture properties and failure mechanisms of single Ni/Au coated acrylic particles at different loading rates.

2. Experimental setup

The particles used in this study contained an acrylic polymer core (Concore™, Conpart AS, NO) sized 3.8 μm in diameter and a Ni/Au bilayer coating of around 80 nm thickness. The chemical composition of the polymer core was 40% acrylic strongly crosslinked with 60% diacrylic. The glass transition temperature of the core was around 40°C and hence the core was in an amorphous type at room temperature. The coefficient of variance (C.V.) of the core size distribution was less than 2% where C.V. was defined as the ratio of the standard deviation to the mean. The Ni/Au coating with the Ni inner layer of about 50 nm thick and the Au outer layer of about 30 nm was deposited on the acrylic particle surface through an electroless plating process. The dispersion process previously established for polymer particles was used to obtain isolated particles [9]. Based on a nanoindentation device (TriboIndenter®, Hysitron Inc., MN, USA), the compression test was performed by using a diamond flat punch of 100 μm in diameter rather than a sharp tip commonly used for nanohardness measurement [16, 17]. The standard load-control mode was employed, in which the normal load followed a predefined load function. Three loading rates 0.02, 0.2 and 2 $\mathrm{mN \cdot s^{-1}}$ were applied to compress single particles to the same peak load 10 mN. The contact load-displacement relationships were directly obtained. For each set of experimental conditions, flat punch test was replicated on different single particles in order to check the repeatability of the results. It has previously been shown that the polymer particles from the same manufacturing batch display remarkably consistent behaviour [8, 9]. This indicates a homogeneous material microstructure and a uniform particle size, as well as highly reproducible test setup. After 12 days of the mechanical test, the surface morphology of the compressed particles was observed by using a field emission scanning electron microscope (SEM) (Zeiss Ultra 55 LE FeSEM, Germany).

3. Results and discussion

The representative stress-strain relationships of particles at three sampling loading rates are plotted in Figure 1. From the current experiment the real contact area between the particle and diamond flat punch (or silicon chip) was unknown hence the true stress-strain relationship of particles could not be derived. Instead, the nominal compression stress σ_C and strain ε_C of the particles were calculated by normalizing the contact load to the maximum cross-section area of undeformed particles and the displacement to the initial diameter of particles [18], as shown in Equations (1) and (2):

$$\sigma_C = \frac{P}{\pi R^2} \tag{1}$$

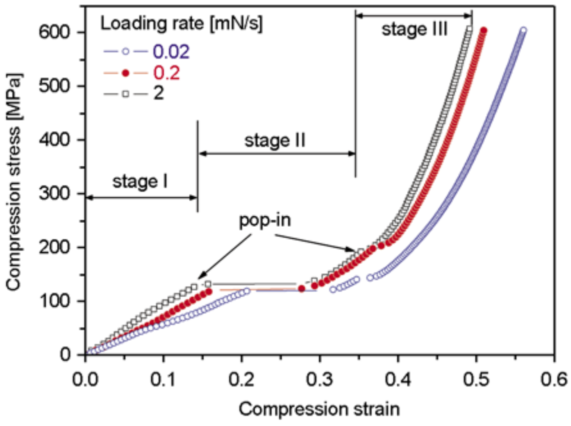

Figure 1. Representative compression stress-strain curves of Ni/Au coated acrylic particles at three loading rates

$$\varepsilon_C = \frac{D}{2R} \tag{2}$$

where P was the applied load, D was the contact displacement and R was the radius of undeformed particles, respectively. The particle displays a strong rate dependence that the faster the compression is, the stiffer the particle behaves. According to the effect of the metal coating, the deformation process of the particle can be clearly divided into three stages [12]. At the initiation of the compression, shown as stage I, the contact stress monotonously increases with strain. The metal coating has a strengthening effect on the Ni/Au coated acrylic particles in comparison with the deformation of the uncoated counterpart. Thereafter, the pop-in appears and the coating effect is significantly reduced in stage II. It has been clarified that the pop-in represents cracking and delamination of the Ni/Au coating from the acrylic core [12]. Finally the coating effect disappears completely and the coated particle behaves the same as the uncoated counterpart in stage III.

The corresponding SEM images of compressed particles are shown in Figure 2. The images were taken from top view, namely in the direction of the compression. Unlike the compact metal, it can be observed that the metal coating is constituted by tiny particles adhering and clustering on the surface of the acrylic core. All images show the severe cracking of the Ni/Au coating and its delamination from the acrylic core, and furthermore cracking and delamination are aggravated with the increase of loading rate. The arrows in the images point out the cracking initiating location and propagating direction. For the particles compressed at two higher loading rates, shown in Figure 2b and 2c, a flattened surface area is clearly observed, while it is not apparent in Figure 2a which represents the slowest compression. The flattened area indicates the expected contact area during the compression and the residual deformation after unloading. The thickness of the fragmented section measured by SEM is in a range of 70 to 100 nm, which is in agreement with the coating characteristics after plating. It implies that the delamination happens at the metal–polymer interface where there is a weaker adhesion than the Ni–Au interface. However, there are significant differences on the fracture pattern between the particle shown in Figure 2a and those in Figure 2b

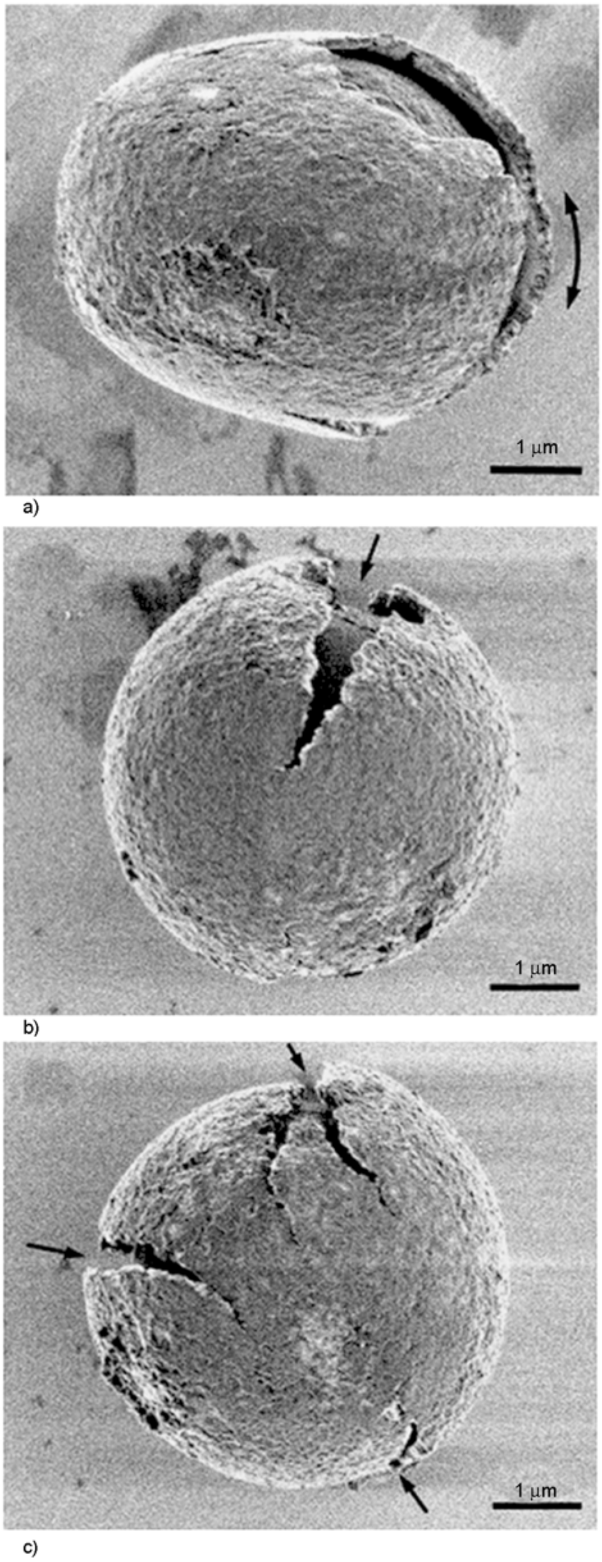

Figure 2. The corresponding SEM images of particles after compression at loading rate (a) 0.02 mN·s^{-1}, (b) 0.2 mN·s^{-1} and (c) 2 mN·s^{-1}. The images are taken from top view (in the direction of compression). Electron high tension (EHT) = 0.5 kV; working distance (W_D) = 2 mm.

and 2c. The cracking of the Ni/Au coating propagates at different directions, depending on loading rates. While the coating is disrupted in meridian direction at loading rates 0.2 and 2 mN·s^{-1}, cracking grows in the latitude direction under the compression with loading rate 0.02 mN·s^{-1}, if considering the compression on two geographic poles. Moreover, the metal coating is expanded in different directions due to the varied cracking paths. As a result, the particles exhibit different projected shapes after compression: elliptic at the smallest loading rate and round at two higher loading rates. Further tests prove that the current observation of two fracture patterns at the corresponding loading rate are repeatable and are the intrinsic response of the Ni/Au coated acrylic particles.

Figure 1 clearly shows that the fracture properties of particles are influenced by the loading rate. The effect of varying loading rates on the fracture properties, such as breaking stress and breaking strain of the Ni/Au coating, is summarized in Figure 3. The breaking strain and the breaking stress were read directly from the corresponding values at the starting point of the first pop-in on the stress-strain curve. While the breaking stress increases with the loading rate, the breaking strain decreases. These results further prove rate dependent behaviour of these particles.

The mechanical behaviour of Ni/Au coated acrylic particles is connected to both composite materials and spherical geometry. The responses of metal and polymer to the external stress are constitutively different. The metal coating of composite particles consists of coagulated nanoparticles to form a heterogeneous shell and it is not as strong as the compact metals with a continuous phase. The dependence of particle behaviour to the loading rate is mainly contributed by the polymer core due to its viscoelastic nature. It has been demonstrated that the highly crosslinked polymer particles under compression experience a viscoelastic deformation which is highly rate dependent. However, the observation of two distinct fracture patterns of particles suggests that the metal coating possesses different deformation mechanisms when varying the loading rate.

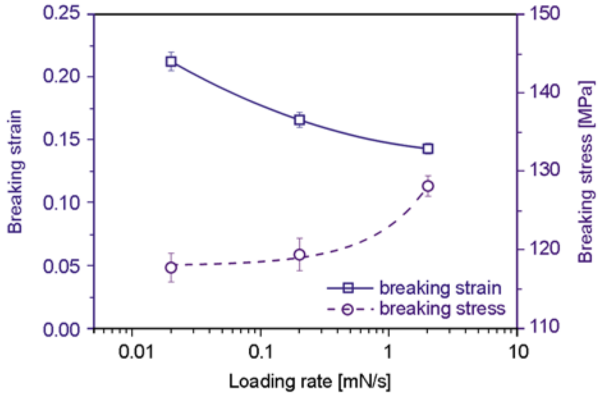

Figure 3. Plots of particle fracture properties versus loading rate. The lines in the figures are guides for the eye

The compression of the Ni/Au coated acrylic particle is schematically illustrated in Figure 4, in which f_1, f_2 and f_3 are the resultant forces on the metal coating and M represents the bending moment, respectively. During the flat punch test, the coating suffers concomitant bending and tension resulting from both the external stress applied on the particle and the internal pressure of the core. The observed cracking propagation in different directions indicates that the dominating factor at varied loading rates is alternating between bending (M) and coating tension (f_3). When the loading rate is up to 0.2 and 2 mN·s^{-1}, the propagation of the coating cracking in meridian direction, as shown in Figure 2b and 2c, implies there is a relatively high tension in latitude direction and thus f_3 dominates the coating fracture. At the loading rate of 0.02 mN·s^{-1}, the coating opening in latitude direction, as shown in Figure 2a, suggests that the bending moment M controls the coating deformation. The exact analysis of coating fracture pattern relies on the viscoelastic properties of the polymer, the mismatch of the properties between the coating and polymer as well as the rate-dependent fracture toughness.

Besides, the adhesion quality between the metal coating and the polymer core might influence the particle response to the external stress. The good

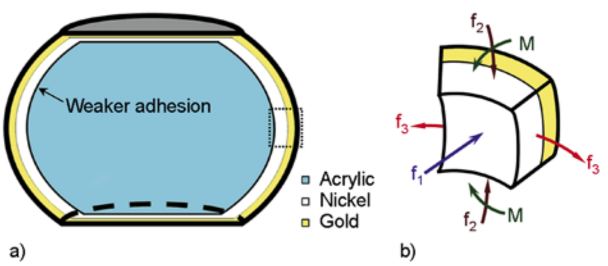

Figure 4. The schematic plots of (a) the vertical section of a compressed particle in compound view and (b) stress illustration of a coating element. The Ni/Au coating is considered as one material and the interactional effect between Ni and Au layers is neglected.

adhesion of the Ni/Au coating bonded to the acrylic core may retard local strain concentrations in the coating and hence increases the apparent consistency of the coating with the core. Due to the absence of the experimental results for the adhesion strength, the effect of the adhesion quality has not been quantified in this study. The assumption that the mechanical contact between the particles and flat punch/substrate is frictionless has been made.

It is worth noting that a theoretical or analytical model to describe large deformation and failure behaviour of metal coated polymer particles is still missing. The reported studies in the literature used finite element modeling to analyze the response of coated spheres and focused on elastic contact and yielding inception [19, 20]. These studies give indication of stresses distribution at the coating/core interface, which improve the understanding of particle deformation. But they only consider the small strain behaviour of coated spheres with the assumption of elastic and elastic-plastic material properties, the continuous phase of the coating and the perfect-bonding of the coating to the spherical substrate. In contrast, in this work the breaking strain of the metal coating is over 15% and even large deformation up to 60% is achieved on the particles. The viscoelastic nature of the core material and the granular microstructure of the metal coating greatly complicate the analysis. The electroless plating prepares heterogeneous bilayer coating on the polymer core with weak bonding. The lack of material constants, such as interfacial adhesion property, elastic modulus and Poisson's ratio of the metal coating, moreover limits the use of these models. Therefore the existing models are not applicable to the current study and further development of physically based model is necessary to verify the deformation mechanism of the metal coated polymer particles at different loading rate.

4. Conclusions

In conclusion, we have conducted the nanoindentation-based flat punch experiments on the Ni/Au coated acrylic particle to investigate the loading rate effect on particle fracture properties under large deformation. The compression stress-strain relationship of single micron-sized particles has shown significant rate dependence which states that the faster compression leads to the stiffer behaviour, associated with the viscoelasticity of the polymer core. The fracture parameters of the metal coating are also sensitive to the loading rate: whereas the breaking stress increases, the breaking strain and the fracture energy decreases as the loading rate increases. Two fracture patterns of particles due to different loading rate have been identified that the cracking of the metal coating propagates in the latitude direction under the slowest compression but in the meridian direction at two higher loading rates. This reveals that the metal coating experiences a bending-dominated deformation at the smallest loading rate while a tension-dominated deformation at two larger sampling loading rates.

Acknowledgements

This work has been supported by The Research Council of Norway, Conpart AS and Invitrogen Dynal AS via a NANOMAT KMB Project (Grant No. NANOMAT-169737/S10). The authors gratefully acknowledge Dr. Yingda Yu for assistance with SEM operation.

References

[1] Forrest S. R.: The path to ubiquitous and low-cost organic electronic appliances on plastic. Nature, **428**, 911–928 (2004).
DOI: 10.1038/nature02498

[2] Lin Y. C., Zhong J.: A review of the influencing factors on anisotropic conductive adhesives joining technology in electrical applications. Journal of Materials Science, **43**, 3072–3093 (2008).
DOI: 10.1007/s10853-007-2320-4

[3] Kim D. O., Jin J. H.: Mechanical property investigation of single polymer particles with the variation of molecular structure of crosslinking monomer. Journal of Applied Polymer Science, **105**, 783–789 (2007).
DOI: 10.1002/app.26133

[4] Dou G., Whalley D. C., Liu C.: Mechanical characterization of individual Ni/Au coated microsize polymer particles. Applied Physics Letters, **92**, 104108/1–104108/3 (2008).
DOI: 10.1063/1.2898219

[5] Lee J-H., Kim D. O., Song G-S., Lee Y., Jung S. B., Nam J-D.: Direct metallization of gold nanoparticles on a polystyrene bead surface using cationic gold ligands. Macromolecular Rapid Communications, **28**, 634–640 (2007).
DOI: 10.1002/marc.200600757

[6] Lee J-H., Lee Y., Nam J-D.: Tunable surface metal morphologies and electrical properties of monodispersed polystyrene beads coated with metal multilayers via electroless deposition. Intermetallics, **17**, 365–369 (2009).
DOI: 10.1016/j.intermet.2008.11.019

[7] Lee J-H., Choi H., Nam J-D.: Tunable electrical properties of polystyrene/gold core-shell structure by in situ metallization of cationic gold complex on selective ion-exchange sites. Journal of Materials Research, **24**, 253–259 (2009).
DOI: 10.1557/JMR.2009.0028

[8] He J. Y., Zhang Z. L., Kristiansen H.: Mechanical properties of nanostructured polymer particles for anisotropic conductive adhesives. International Journal of Materials Research, **98**, 389–392 (2007).

[9] He J. Y., Zhang Z. L., Midttun M., Fonnum G., Modahl G. I., Kristiansen H., Redford K.: Size effect on mechanical properties of micron-sized PS–DVB polymer particles. Polymer, **49**, 3993–3999 (2008).
DOI: 10.1016/j.polymer.2008.07.015

[10] He J. Y., Zhang Z. L., Kristiansen H.: Nanomechanical characterization of single micron-sized polymer particles. Journal of Applied Polymer Science, **113**, 1398–1405 (2009).
DOI: 10.1002/app.29913

[11] He J. Y., Zhang Z. L., Kristiansen H.: Compression properties of individual micron-sized acrylic particles. Materials Letters, **63**, 1696–1698 (2009).
DOI: 10.1016/j.matlet.2009.05.013

[12] He J. Y., Helland T., Zhang Z. L., Kristiansen H.: Fracture of micrometre-sized Ni/Au coated polymer particles. Journal of Physics D: Applied Physics, **42**, 085405/1–085405/5 (2009).
DOI: 10.1088/0022-3727/42/8/085405

[13] Flory A., McKenna G. B.: Microscopic origins of the normal force responses of glassy polymers in the subyield range of deformation. Macromolecules, **38**, 1760–1766 (2005).
DOI: 10.1021/ma047995g

[14] Jeusette M., Leclère P., Lazzaroni R., Simal F., Vaneecke J., Lardot T., Roose P.: New 'all-acrylate' block copolymers: Synthesis and influence of the architecture on the morphology and the mechanical properties. Macromolecules, **40**, 1055–1065 (2007).
DOI: 10.1021/ma061613k

[15] Kashiwagi T., Mu M., Winey K., Capriano B., Raghavan S. R., Pack S., Rafailovich M., Yang Y., Grulke E., Shields J., Harris R., Douglas J.: Relation between the viscoelastic and flammability properties of polymer nanocomposites. Polymer, **49**, 4358–4368 (2008).
DOI: 10.1016/j.polymer.2008.07.054

[16] Yang B., Wadsworth J., Nieh T-G.: Thermal activation in Au-based bulk metallic glass characterized by high-temperature nanoindentation. Applied Physics Letters, **90**, 061911/1–061911/3 (2007).
DOI: 10.1063/1.2459383

[17] Mao W. G., Shen Y. G., Lu C.: Deformation behavior and mechanical properties of polycrystalline and single crystal alumina during nanoindentation. Scripta Materialia, **65**, 127–130 (2011).
DOI: 10.1016/j.scriptamat.2011.03.022

[18] Zhang Z. L., Kristiansen H., Liu J.: A method for determining elastic properties of micron-sized polymer particles by using flat punch test. Computational Materials Science, **39**, 305–314 (2007).
DOI: 10.1016/j.commatsci.2006.06.009

[19] Liu S. B., Peyronnel A., Wang Q. J., Keer L. M.: An extension of the Hertz theory for three-dimensional coated bodies. Tribology Letters, **18**, 303–314 (2005).
DOI: 10.1007/s11249-004-2757-4

[20] Goltsberg R., Etsion I., Davidi G.: The onset of plastic yielding in a coated sphere compressed by a rigid flat. Wear, **271**, 2968–2977 (2011).
DOI: 10.1016/j.wear.2011.06.025

eXPRESS Polymer Letters Vol.6, No.3 (2012) 204–212
Available online at www.expresspolymlett.com
DOI: 10.3144/expresspolymlett.2012.23

High-resolution solid-state NMR study of isotactic polypropylenes

O. Fričová[1]*, M. Uhrínová[1], V. Hronský[1], M. Kovaľaková[1], D. Olčák[1], I. Chodák[2], J. Spěváček[3]

[1]Department of Physics, Faculty of Electrical Engineering and Informatics, Technical University of Košice, Park Komenského 2, 042 00 Košice, Slovakia
[2]Polymer Institute, Slovak Academy of Sciences, Dúbravská cesta 9, 842 36 Bratislava, Slovakia
[3]Institute of Macromolecular Chemistry, Academy of Sciences of the Czech Republic, Heyrovsky Sq. 2, 162 06 Prague 6, Czech Republic

Received 11 July 2011; accepted in revised form 25 September 2011

Abstract. The high-resolution solid-state ^{13}C NMR spectra were recorded for metallocene (m) and Ziegler-Natta (ZN) isotactic polypropylenes (iPP) in pelletized form using cross polarization (CP) and magic angle spinning (MAS) techniques within the temperature range of 20–160°C. Besides the CP MAS experiments also the MAS ^{13}C NMR spectra (without CP), MAS ^{1}H NMR spectra and rotating frame spin-lattice relaxation times $T_{1\rho}$ (^{13}C) were measured at elevated temperatures. With the rise of temperature the splitting of CH_2, CH and CH_3 signals into two components was detected in ^{13}C NMR spectra and assigned to amorphous and crystalline phases. The temperature dependences of chemical shifts and integral intensities obtained from the deconvoluted spectra provided information on the main chain and CH_3 groups motions in amorphous and crystalline regions of studied samples. While $T_{1\rho}$ (^{13}C) values show that the rate of segmental motion in amorphous regions in m-iPP and ZN-iPP is virtually the same, larger linewidths in ^{13}C and ^{1}H NMR spectra indicate somewhat larger restraints of the motion in amorphous regions of ZN-iPP.

Keywords: *material testing, metallocene isotactic polypropylene, Ziegler-Natta isotactic polypropylene, solid state NMR, segmental motion*

1. Introduction

Since the commercialization of Ziegler-Natta process of polypropylene synthesis, this technology was for decades almost the only source of all grades of polypropylene (PP). Only at the end of the last century a new process was developed, based on metallocene catalysis. This process provides new types of metallocene PP (m-PP) different from previous Ziegler Natta PP types (ZN-PP), the main difference consisting in the production of grades with different stereoregularity (isotactic, syndiotactic, hemi-isotactic, atactic) [1] or narrow polydispersity of the polymer chains, compared to Ziegler-Natta catalysts, which produces only highly polydisperse isotactic polymers. The tacticity of isotactic (i) m-PP and ZN-PP is virtually the same (98% of isotactic diads), though the configurational defects are more frequent in m-iPP [2]; this might be reflected in a lower melting temperature of m-iPP in comparison with ZN-iPP.

Comparing to ZN-iPP, m-iPP offers a unique balance of stiffness, transparency, and organoleptic properties which is not achievable with ZN-iPP. On the other hand, m-iPP is usually less rigid than ZN-iPP homopolymers. Thus, any additional information on similarity or differences in m-iPP vs. ZN-iPP behaviour seems to be of scientific as well as

---

*Corresponding author, e-mail: olga.fricova@tuke.sk commercial importance. NMR investigation is considered to be one of the basic relevant methods.

The high-resolution solid-state ^{13}C NMR studies of iPP reported NMR spectra recorded with combination of magic angle spinning (MAS), cross polarisation (CP) and dipolar decoupling (DD) techniques [3–14]. Since iPP can crystallize in several crystalline forms, depending on the crystallization temperature and on the presence of specific nucleating agents, the shape of the spectra was found to depend strongly on the physical treatment of the sample and the temperature at which the NMR experiment was carried out.

Three symmetrical resonance lines related to the CH_2, CH and CH_3 groups were observed in the ^{13}C NMR spectra measured on iPP sample crystallizing in the hexagonal β-form at room temperature. On the other hand, the sample crystallizing in monoclinic structure (α-form) prepared by an annealing procedure gives the spectra with the CH_2 and CH_3 lines split into the doublets. This splitting which appeared in NMR experiments carried out with CP as well as without the application of the CP technique, was shown to be associated with two different packing sites in crystals [4, 7, 11]. With increasing temperature the lines of the CH_2 and CH_3 doublets with lower chemical shifts were shown to be gradually shifted to the positions with higher chemical shifts and merged into singlet lines. A more vigorous molecular motion activated by the rise of temperature, averaged each crystalline carbon resonance over the two sites, and resulted in the disappearance of the doublets [11]. An absence of the abovementioned crystalline doublets in iPP crystallizing in the hexagonal (β-form) was explained by the absence of different packing sites of chains in crystals [4].

It was shown that the increase of the temperature gives rise to new resonance lines of the CH_2 and CH groups with chemical shifts between the lines observed at room temperature and those observed in the iPP solution. These lines detected as separated lines in the MAS DD spectra and as shoulders of the original lines in the CP MAS DD experiment, were assigned to the carbons in amorphous regions of the partially crystalline iPP [7].

To reveal if there are some differences in the structure and molecular motion between m-iPP and ZN-iPP we report the high-resolution ^{13}C NMR study of the m-iPP and ZN-iPP crystallizing predominantly in the hexagonal β-form, based on CP MAS DD and single pulse MAS DD techniques at temperatures ranging from room temperature up to the melting point of the polymer. According to our knowledge, m-iPP was not studied by solid-state NMR until now.

2. Experimental

2.1. Materials

Two samples of predominantly isotactic PP prepared in pelletized form were used for the study – METOCENE HM 562 N (m-iPP, Lyondellbasell) prepared by metallocene-catalysed polymerization and TATREN HG 1007 (ZN-iPP, Slovnaft, Slovakia) prepared by Ziegler-Natta polymerization. The degree of crystallinity X_c, taking the value of 209 J/g [15] as the heat of fusion of 100% crystalline iPP, and melting temperature T_m of the samples were determined by DSC (Mettler Toledo DSC 821 (Greifensee, Switzerland), second run, heating rate 10°C/minute), the glass transition temperature T_g was determined by DMTA experiment (TA Analysis Q800 (New Castle, DE, USA), heating rate 2°C/minutes, frequency 10 Hz). The values are listed in Table 1. The samples were not treated prior to NMR experiments except the cutting of pellets into smaller pieces in order to achieve stable spinning of the NMR rotor.

Table 1. The degree of crystallinity X_c, melting temperature T_m and glass transition temperature T_g of m-iPP and ZN-iPP samples

Sample	X_c [%]	T_m [°C]	T_g [°C]
m-iPP	52	145.2	12
ZN-iPP	55	163.6	10

2.2. NMR measurements

The high-resolution solid-state ^{13}C NMR measurements were carried out on a 400 MHz Varian solid-state NMR spectrometer (Palo Alto, CA, USA). The high-resolution ^{13}C NMR spectra were recorded at the resonance frequency of approximately 100 MHz with the use of 4 mm rotors and magic angle spinning frequency of 6 kHz. In CP experiments the Hartmann-Hahn condition was obtained with the radio frequency field strength of 51 kHz, a contact time 1 ms and relaxation delay between two consecutive scans 5 s. The high power proton-decoupling field of 85 kHz was applied during data acquisition.

The CP MAS ^{13}C NMR experiments were carried out within the temperature range of 20–160°C and the MAS ^{13}C NMR (without CP) spectra were recorded at the temperatures 20, 90 and 160°C with relaxation delay 240 s. It has to be stressed that the measurement at 160°C was performed on the molten sample of m-iPP. Besides the high-resolution solid-state ^{13}C NMR spectra also a rotating frame spin–lattice relaxation times $T_{1\rho}$ (^{13}C) were measured at 64 and 90°C. A spin locking experiment was performed under CP and MAS conditions. During spin-lock pulse, which was up to 50 ms, and detection period the dipolar decoupling fields of 85 and 100 kHz were applied, respectively. The ^{13}C spins were locked with the field of 77 kHz.

The chemical shifts and integral intensities were acquired from the deconvoluted spectra. All deconvolutions were done assuming the Lorentzian's lineshapes. The chemical shifts were referenced to the TMS using adamantane as an external standard and they were determined with accuracy better than 0.02 ppm. The calibration of the temperature inside the rotor was performed with the use of the measured temperature dependence of the ^{207}Pb NMR chemical shift of lead nitrate [16]. The temperature was controlled by the variable temperature system unit with the accuracy of ±0.1°C, however, the gradient of the temperature along the axis of the rotor is significantly larger and depends on the temperature.

^{1}H MAS NMR spectra were measured on the same instrument at the frequency 400 MHz. The duration of the 90° radio-frequncy pulse was 2.7 μs, spinning frequency was 6 kHz.

3. Results and discussion

The CP MAS ^{13}C NMR spectra measured at different temperatures on the solid m-iPP sample and the MAS ^{13}C NMR spectrum measured at 160°C without CP (due to the fact that the sample was molten at this temperature and high molecular mobility made the CP inefficient at this temperature) are depicted in Figure 1. In the spectrum measured at room temperature three broad symmetrical resonance lines can be observed with the chemical shifts of 44.45, 26.63 and 22.20 ppm related to CH_2, CH and CH_3 carbons, respectively. They reflect broad distributions of possible conformations of iPP chains at room temperature which is slightly above the glass transition. A small asymmetry of the CH_3 line will be discussed later. Three resonance lines are also observed in the spectrum recorded at 160°C, however, they are considerably narrower and with higher chemical shifts of 47.09, 29.48 and 22.36 ppm when compared with those observed in the spectrum measured at room temperature. The conspicuous line narrowing observed in this spectrum reflects the rapid changes of conformations in the molten sample.

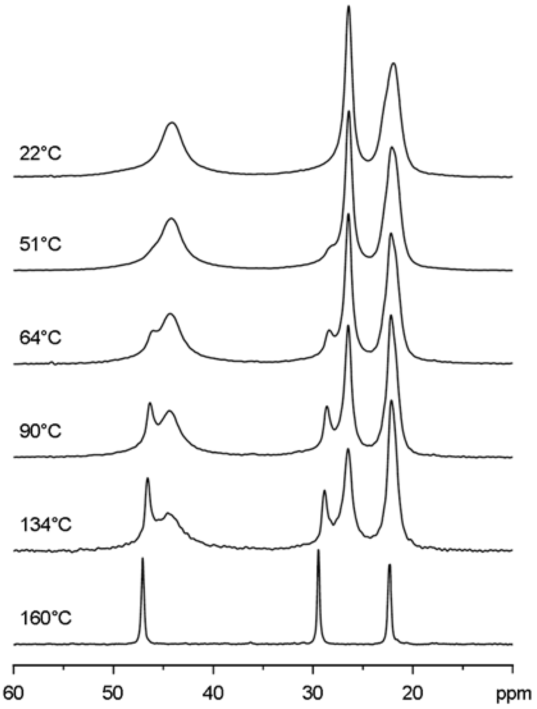

Figure 1. CP MAS ^{13}C NMR spectra of m-iPP measured at temperatures as indicated, except the spectrum measured at 160°C for the molten sample using single pulse MAS ^{13}C NMR technique. CP MAS ^{13}C NMR spectra were normalized

Figure 1 shows that besides the lines observed at room temperature, the new resonance lines of CH_2 and CH carbons appear in the measured spectra with the rise of temperature. Similar effect was in the past observed in the spectra obtained using MAS DD ^{13}C NMR technique, i. e., without CP, on the PP crystallizing in α-form and these lines were assigned to the carbons within the chains of amorphous regions [7, 11]. Therefore, additional lines detected for m-iPP at temperatures above 51°C can be associated with the CH_2 and CH carbons in amorphous regions of m-iPP.

The main characteristics of the spectra measured for ZN-iPP exhibit a similar behaviour as those shown for m-iPP confirming that both iPP samples are in the hexagonal β-form [4, 6, 7]. However, small differences between the spectra measured at the same temperature can be found. In spectra measured at elevated temperatures the resonance lines related to the CH_2 and CH carbons in amorphous regions of m-iPP are better resolved than those of ZN-iPP. The CH_2 lines of the spectra measured on both samples at 64°C depicted in Figure 2 illustrate mentioned differences. Therefore, it can be deduced that the onset of the molecular processes in the amorphous regions, which are associated with appearance of new lines, is observed in m-iPP at lower temperature as compared with that in ZN-iPP. The resonance lines discussed above apply to the main chain carbons of both polymers and therefore the changes observed in the spectra have to be associated with segmental motion in iPP samples. The differences discussed above can then indicate somewhat higher chain mobility in the amorphous regions of m-iPP. Alternative explanation that the observed differences might be in connection with the dispersion of chemical shifts seems to be for two highly-isotactic polymers rather improbable. The segmental motion in amorphous regions of iPP is related to the glass transition relaxation (β-relaxation) that was recently studied by wide-line ^1H NMR [17]. To confirm a difference discussed above we also measured ^1H NMR spectra under MAS with the spinning rate of 6 kHz at 71°C. The splitting of the amorphous signal into components related to the protons of different PP groups can be seen in Figure 2. Evidently, due to the larger restrictions in chain mobility of ZN-iPP in comparison with m-iPP the better resolution of the spectrum is observed in the case of m-iPP.

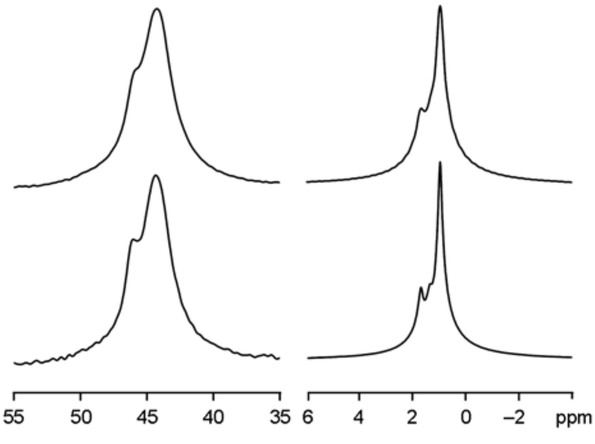

Figure 2. The CH_2 lines of the normalized CP MAS ^{13}C NMR spectra (left) and ^1H MAS NMR spectra (right) measured at 64 and 71°C, respectively, for m-iPP (bottom) and ZN-iPP (top)

In spite of the fact that no splitting of the CH_3 lines was observed in the spectra, the change of this line shape, which is very similar for both samples, is of interest. At 22°C at the left hand side of this peak and at higher temperature at the right hand side of this peak a shoulder is formed, at 134°C the line seems to be symmetrical. The CH_3 line therefore consists of two overlapping lines shown in Figure 3 whose intensities strongly depend on temperature. The line indicated as the left hand side shoulder at 22°C can be related to the most mobile CH_3 groups in the amorphous regions and that indicated as the right hand side shoulder at higher temperatures to less mobile CH_3 groups in crystalline and probably also amorphous regions. With increasing temperature, a mobility of the less mobile CH_3 groups increases and therefore also the intensity of the right hand side shoulder decreases. At sufficiently high temperatures only a small fraction of CH_3

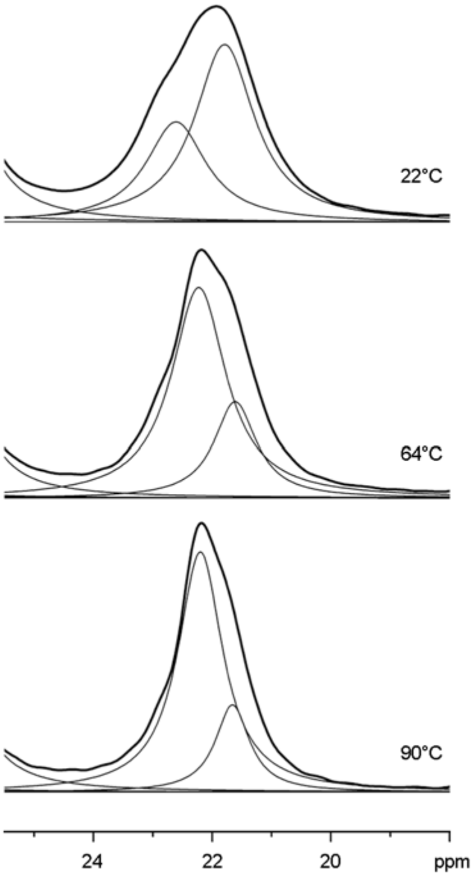

Figure 3. Deconvolutions of CH_3 lines of the CP MAS ^{13}C NMR spectra measured on m-iPP at different temperatures

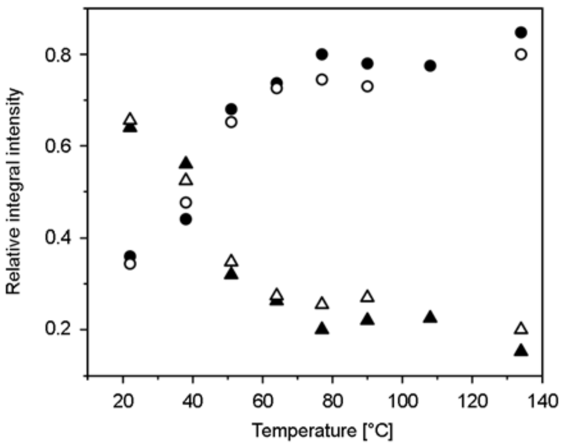

Figure 4. The temperature dependences of the relative integral intensity of the CH_3 resonance lines related to the more mobile (circles) and less mobile CH_3 groups (triangles) of m-iPP (solid symbols) and ZN-iPP (open symbols)

groups has still a low mobility. The temperature dependences of the relative integral intensities of both CH_3 lines obtained by deconvolution, which are shown in Figure 4, support assumption described above. Generally, intensities can be influenced by the transfer of magnetisation during the cross polarisation. However, only a slight difference in motion of CH_3 groups in amorphous and crystalline regions can be deduced from CH_3 peaks which are detected without splitting, therefore it is possible that the transfer of magnetization from the protons to carbons within the CH_3 groups in amorphous and crystalline regions is essentially the same. An agreement between intensities obtained for CH_3 carbons from experiments with CP (Figure 4) and without CP (mentioned in further text) supports this assumption.

The $T_{1\rho}$ (^{13}C) measurements at elevated temperatures are also relevant in this connection. The CH_2, CH and CH_3 resonance lines of the spectra detected after increasing spin-lock pulses were deconvoluted into two lines and the integral intensities versus spin-lock pulse duration were plotted for all peaks. The relaxation curves were fitted by single exponential decays. The $T_{1\rho}$ (^{13}C) data are summarised in Table 2. The $T_{1\rho}$ (^{13}C) relaxation times associated with the left side peaks of the CH_2, CH and CH_3 carbon types in amorphous regions are at 64°C shorter than that associated with the respective right side peaks corresponding to crystalline regions. In the case of the CH_2 and CH groups at 64°C the shorter and the longer relaxation times can be assigned to the relaxation processes in the amorphous and the crystalline phase, respectively, and the two types of CH_3 carbons relax with different relaxation times reflecting two different molecular processes. For amorphous CH_2 and CH carbons the $T_{1\rho}$ (^{13}C) values at 90°C are substantially longer than those at 64°C resulting in similar relaxation times of both components of CH_2 and CH signals. This result confirms that for the amorphous component we operate in the high-temperature part of the relaxation curve where a higher $T_{1\rho}$ (^{13}C) corresponds to higher mobility (shorter correlation time). Subsequently, from comparison of $T_{1\rho}$ (^{13}C) values obtained for main chain CH_2 and CH carbons in m-iPP and ZN-iPP (cf. Table 2) it follows that the rate of the segmental motion in mid-kHz region is in m-iPP and ZN-iPP virtually the same.

The CP MAS ^{13}C NMR spectra measured for m-iPP and ZN-iPP at different temperatures were deconvoluted in the same manner as mentioned above and the chemical shifts of the separated lines were determined. The temperature dependences of the chemical shifts depicted in Figure 5 show that the chemical shifts of CH carbons in the crystalline regions of the sample are the same in the whole temperature range investigated, however, the chemical shifts of the CH_2 and CH_3 lines show slight gradual increase as a function of the temperature within the whole temperature range and within the temperature range above 55°C, respectively.

Table 2. The rotating frame spin lattice relaxation times $T_{1\rho}$ (^{13}C) in m-iPP and ZN-iPP related to CH_2, CH and CH_3 carbons in amorphous and crystalline regions. Measurements were carried out at 64 and 90°C

Sample	T [°C]	$T_{1\rho}$ (^{13}C)^a [ms]					
		CH_2		CH		CH_3	
		amorphous	crystalline	amorphous	crystalline	amorphous	crystalline
m-iPP	64	3.3	26.1	6.1	26.9	20.1	40.5
	90	17.0	23.0	22.2	22.6	21.1	39.8
ZN-iPP	64	3.6	29.8	7.0	30.2	23.6	47.6
	90	17.4	29.6	23.2	29.4	23.8	46.1

^{a}Estimated error ±10%.

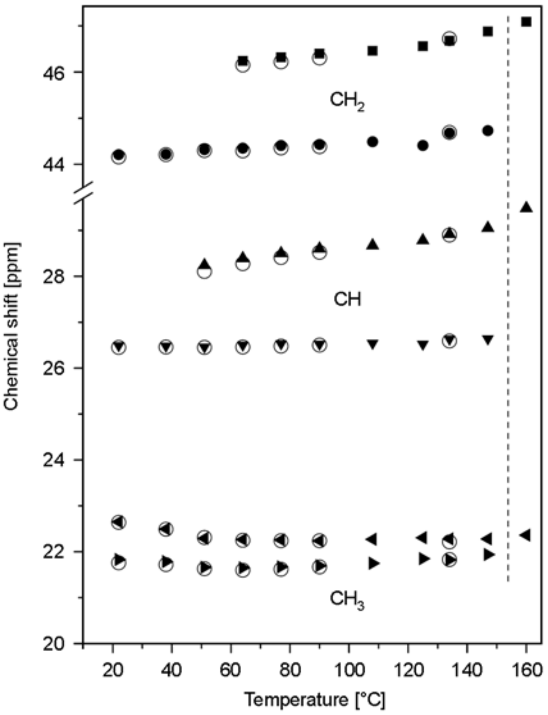

Figure 5. The temperature dependences of the chemical shift of the lines related to the particular carbon types of m-iPP (solid symbols) and ZN-iPP (open circles). For all carbon types larger chemical shifts correspond to amorphous carbons and smaller chemical shifts correspond to crystalline carbons. A vertical dashed line separates the values obtained for solid polymers from those obtained for the molten m-iPP sample

The chemical shifts of the CH_2 and CH lines related to the amorphous regions as a function of temperature show increasing tendency and the chemical shift of the amorphous CH_3 groups is constant within the broad temperature range above 55°C. It is evident, however, that the chemical shifts of all amorphous resonance lines approach very closely the chemical shifts observed for the molten m-iPP at 160°C.

Based on the results mentioned above it can be concluded that at room temperature, which is slightly above the glass transition temperature, m-iPP and ZN-iPP samples behave in the NMR experiments as if they were in the glassy state with undistinguished motion between the amorphous and crystalline regions. The rise of the temperature results in more conspicuous enhancement of the mobility of the chain segments in the amorphous regions and the quick conformation changes associated with the motion in these regions result in the new resonance lines in close proximity to the lines observed at room temperature. The fact that the chemical shifts of the lines related to the CH_2 and CH groups in amorphous regions gradually increase up to the chemical shift observed for the molten sample indicates that the conformation changes between the glassy and molten state are implemented gradually in the amorphous regions and, on the other hand, the abrupt change of conformations in crystalline domains in the process of melting can be drawn from the data in Figure 5.

The temperature dependence of the chemical shift of the resonance lines related to the CH_3 groups in amorphous regions where the values in the solid polymer are indistinguishable from that in molten state indicates that the CH_3 groups in amorphous regions can rotate virtually freely within a broad temperature range. In the case of crystalline regions the increase of the temperature causes that CH_3 groups rotate gradually in a similar way as in molten sample. All but fluent change of the CH_3 group mobility between crystalline and molten state can be deduced from Figure 5.

The relative integral intensities of the lines related to the particular groups were estimated for both samples from the spectra obtained by deconvolution. Under the applied CP the relative integral intensities of the lines related to the CH_2 and CH groups in amorphous regions and the intensities of the lines related to these groups in crystalline regions are at variance with the values of the degree of crystallinity as obtained by DSC (cf. Figure 1 and Table 1). As mentioned above, a motion restricts the magnetisation transfer from the ^1H spin system to that of the ^{13}C in the CP MAS NMR experiment. This is the reason why relative integral intensities of the lines related to crystalline regions are higher in CP MAS NMR spectra than the respective degrees of crystallinity. For the molten sample m-iPP the CP is completely inefficient.

For quantitative evaluations, the MAS DD ^{13}C NMR spectra (without CP) were measured at temperature 90°C (Figure 6). The evident difference between the spectra measured by the two different techniques at the same temperature can be seen comparing the spectra measured without CP and with CP as shown in Figure 6. Besides higher intensities of the lines of the CH_2 and CH carbons in amorphous regions also

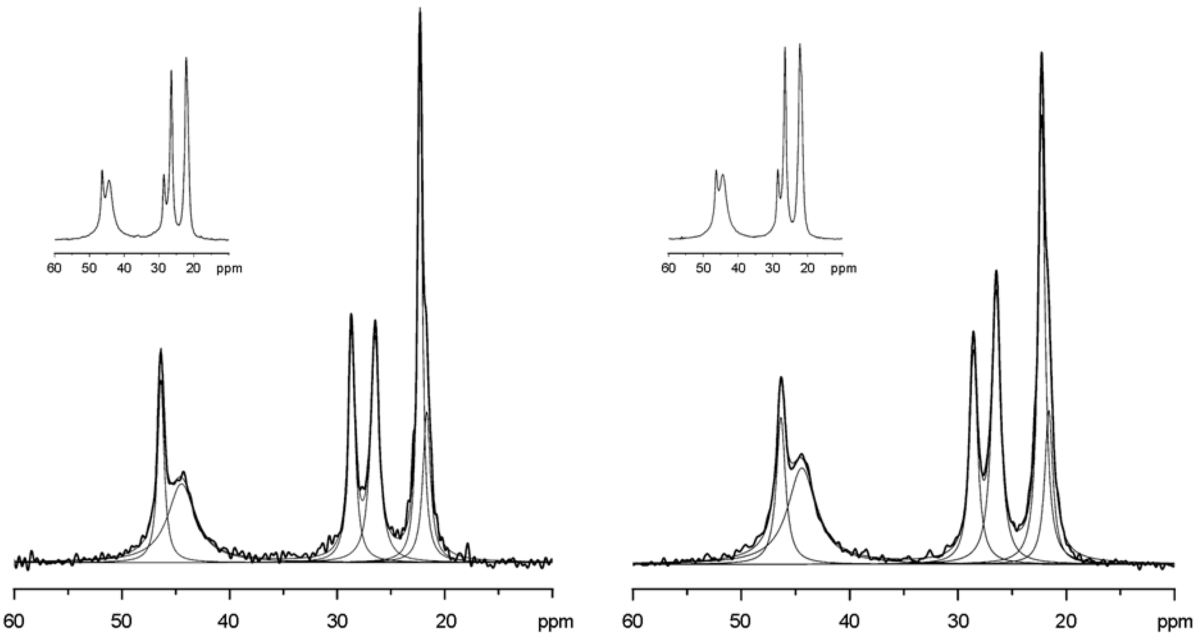

Figure 6. Deconvolutions of the normalized DD MAS (without CP) ^{13}C NMR spectra of m-iPP (left) and ZN-iPP (right) measured at 90°C. Corresponding DD CP MAS ^{13}C NMR spectra measured at the same temperature are shown in the insets for comparison

better resolved two signal components of the CH_3 carbons are observed in MAS DD ^{13}C NMR spectra without CP.

Deconvolution of the spectra measured for the m-iPP and ZN-iPP is also shown in Figure 6 and the relative integral intensities of the individual lines determined by this procedure are summarized for both studied samples in Table 3. In spite of the fact that we have used a two-phase model of polymer with crystalline and amorphous regions only, while three-phase model takes into account also interphase regions of the partially crystalline polymer [7, 11, 17], the relative integral intensities of the lines related to the main chain CH_2 and CH groups in the crystalline regions of both samples are in accordance with the degree of the crystallinity obtained by DSC (cf. Table 1). No changes of the degree of the crystallinity with time were observed in the NMR spectra.

Table 3. The relative integral intensities of the lines of CH_2 and CH carbons as obtained by deconvolution of the MAS DD ^{13}C NMR spectra measured for m-iPP and ZN-iPP at 90°C

Sample	Integral intensity			
	CH_2		CH	
	amorphous	crystalline	amorphous	crystalline
m-iPP	0.44	0.56	0.46	0.54
ZN-iPP	0.41	0.59	0.41	0.59

The line widths should be also briefly mentioned. The fact that the resonance lines related to the amorphous regions at 90°C are narrower than the corresponding lines related to the crystalline regions (cf. Figure 6) was expected and it applies to both CH_2 and CH groups and both samples. The higher mobility of the amorphous chain segments in comparison with the helix chains in the crystalline domains accounts for the differences of the line widths. Somewhat larger spatial restraints of the chain motion in ZN-iPP can be deduced from the broader amorphous CH_2 and CH lines for ZN-iPP in comparison with m-iPP (by 22 and 7 Hz for CH_2 and CH carbons, respectively).

4. Conclusions

High resolution ^{13}C NMR spectra were obtained for m-iPP and ZN-iPP samples using CP and MAS techniques. The CP MAS NMR spectra were recorded in the temperature range from room temperature up to 160°C. Three resonance lines corresponding to CH_2, CH a CH_3 groups were observed in the spectra measured at room temperature which is approximately 10 K above the glass transition temperature of studied samples and also at 160°C for molten sample. The relatively large widths of resonance lines detected at room temperature reflect low mobility of iPP chains and wide distribution of chains conformations. On contrary very narrow resonance lines detected in molten sample reflect fast conformational changes. In the spectra measured above 50°C the resonance lines corresponding to CH_2 and CH carbons were split into two components and assigned to chains in amorphous and crystalline regions of iPP. Temperature dependences of chemical shifts of split lines show that the conformation changes between the glassy and molten state are implemented gradually with increasing temperature while in crystalline regions the conformational changes are observed only under melting process. The existence of two components was revealed also for CH_3 carbons. The crystallinity of the studied samples was determined from the deconvoluted MAS ^{13}C NMR spectra measured without CP at 90°C. Deconvolutions of CH_2 and CH lines give essentially the same crystallinities; the obtained values agree well with those determined using DSC. While virtually the same rate of the segmental motion in mid-kHz region in amorphous m-iPP and ZN-iPP chains follows from $T_{1\rho}$ (^{13}C) values, larger CH_2 and CH linewidths in ^{13}C and ^{1}H NMR spectra indicate somewhat larger restraints of the motion in ZN-iPP in comparison with m-iPP.

Acknowledgements

We support research activities in Slovakia/Project is co-financed from EU funds. This paper was developed within the Project ‘Centre of Excellence of the Integrated Research & Exploitation of the Advanced Materials and Technologies in the Automotive Electronics’, ITMS 26220120055.
One of the authors (IC) appreciates the financial support of this research through Slovak Research and Development Agency (grant APVV-0226-06).

References

[1] Kaempfer D., Thomann R., Mülhaupt R.: Melt compounding of syndiotactic polypropylene nanocomposites containing organophilic layered silicates and in situ formed core/shell nanoparticles. Polymer, **43**, 2909–2916 (2002).
DOI: 10.1016/S0032-3861(02)00113-1

[2] Bond E. B., Spruiell J. E.: The effects of atacticity, comonomer content, and configurational defects on the equilibrium melting temperature of monoclinic isotactic polypropylene. Journal of Applied Polymer Science, **81**, 229–236 (2001).
DOI: 10.1002/app.1433

[3] Bunn A., Cudby M. E. A., Harris R. K., Packer K. J., Say B. J.: Solid-state high-resolution ^{13}C n.m.r. spectra of polypropene. Journal of the Chemical Society, Chemical Communications, 15–16 (1981).
DOI: 10.1039/C39810000015

[4] Bunn A., Cudby M. E. A., Harris R. K., Packer K. J., Say B. J.: High resolution ^{13}C n.m.r. spectra of solid isotactic polypropylene. Polymer, **23**, 694–698 (1982).
DOI: 10.1016/0032-3861(82)90053-2

[5] Lyerla J. R., Yannoni C. S.: High-resolution carbon-13 NMR of polymers in the solid state. IBM Journal of Research and Development, **27**, 302–312 (1983).
DOI: 10.1147/rd.274.0302

[6] Gomez M. A., Tanaka H., Tonelli A. E.: High-resolution solid-state ^{13}C nuclear magnetic resonance study of isotactic polypropylene polymorphs. Polymer, **28**, 2227–2232 (1987).
DOI: 10.1016/0032-3861(87)90378-8

[7] Saito S., Moteki Y., Nakagawa M., Horii F., Kitamura R.: High-resolution solid-state ^{13}C NMR study of isotactic polypropylenes isothermally crystallized from the melt. Macromolecules, **23**, 3256–3260 (1990).
DOI: 10.1021/ma00215a010

[8] Tanaka H.: ^{13}C magnetic relaxation times in isotactic polypropylene. European Polymer Journal, **27**, 565–572 (1991).
DOI: 10.1016/0014-3057(91)90137-D

[9] Zeigler R. C.: Dynamics of polypropene and propene-ethylene copolymers at temperatures above ambient. Macromolecular Symposia, **86**, 213–227 (1994).
DOI: 10.1002/masy.19940860117

[10] Tonelli A. E.: High resolution NMR as a local probe of structure, conformation, and mobility in solid polymers. Journal of Molecular Structure, **355**, 105–119 (1995).
DOI: 10.1016/0022-2860(95)08901-7

[11] Kitamaru R.: Phase structure of polyethylene and other crystalline polymers by solid-state ^{13}C NMR. Advances in Polymer Science, **137**, 41–102 (1998).
DOI: 10.1007/3-540-69685-7_2

[12] Alamo R. G., Blanco J. A., Carrilero I., Fu R.: Measurement of the ^{13}C spin-lattice relaxation time of the non-crystalline regions of semicrystalline polymers by a cp MAS-based method. Polymer, **43**, 1857–1865 (2002).
DOI: 10.1016/S0032-3861(01)00761-3

[13] Miyoshi T., Mamun A., Hu W.: Molecular ordering and molecular dynamics in isotactic-polypropylene characterized by solid state NMR. The Journal of Physical Chemistry B, **114**, 92–100 (2010).
DOI: 10.1021/jp908649y

[14] Hu W-G., Schmidt-Rohr K.: Polymer ultradrawability: The crucial role of α-relaxation chain mobility in the crystallites. Acta Polymerica, **50**, 271–285 (1999).
DOI: 10.1002/(SICI)1521-4044(19990801)50:8<271::AID-APOL271>3.0.CO;2-Y

[15] Zhang X., Zhao Y., Wang Z., Zheng C., Dong X., Su Z., Sun P., Wang D., Han C. C., Xu D.: Morphology and mechanical behavior of isotactic polypropylene (iPP)/syndiotactic polypropylene (sPP) blends and fibers. Polymer, **46**, 5956–5965 (2005).
DOI: 10.1016/j.polymer.2005.05.004

[16] Bielecki A., Burum D. P.: Temperature dependence of ^{207}Pb MAS spectra of solid lead nitrate. An accurate, sensitive thermometer for variable-temperature MAS. Journal of Magnetic Resonance, Series A, **116**, 215–220 (1995).
DOI: 10.1006/jmra.1995.0010

[17] Ševčovič L., Mucha L'.: Study of stretched polypropylene fibres by ^{1}H pulsed and CW NMR spectroscopy. Solid State Nuclear Magnetic Resonance, **36**, 151–157 (2009).
DOI: 10.1016/j.ssnmr.2009.09.001

eXPRESS Polymer Letters Vol.6, No.3 (2012) 213–223
Available online at www.expresspolymlett.com
DOI: 10.3144/expresspolymlett.2012.24

Multiwall carbon nanotube-filled natural rubber: Electrical and mechanical properties

L. Bokobza[*]

Laboratoire PPMD, ESPCI ParisTech, 10 rue Vauquelin, 75231 Paris Cedex, France

Received 11 July 2011; accepted in revised form 25 September 2011

Abstract. The influence of multiwall carbon nanotube (MWNTs) contents on electrical and mechanical properties of MWNTs-reinforced natural rubber (NR) composites is studied. The volume resistivity of the composites decreases with increasing the MWNTs content and the electrical percolation threshold is reached at less than 1 phr of MWNTs (phr = parts of filler by weight per hundred parts of rubber). This is caused by the formation of conductive chains in the composites. Electrical measurements under uniaxial deformation of a composite carried out at a filler loading above the percolation threshold, indicate a gradual disconnection of the conducting network with the bulk deformation. The drop in the storage modulus G' with the shear strain amplitude (Payne effect) is also attributed to a breakdown of the filler network. Considerable improvement in the stiffness is obtained upon incorporation of MWNTs in the polymer matrix but the main factor for reinforcement of NR by MWNTs appears to be their high aspect ratio rather than strong interfacial interaction with rubber. The tensile strength and the elongation at break of the composites are reduced with regard to the unfilled sample. This is probably due to the presence of some agglomerates that increase with the nanotube content. This hypothesis is confirmed by a cyclic loading of the composites where it is seen that the deformation at break occurs at a much higher level of strain in the second stretch than in the first one. The overall significant property improvements are the result of a better nanotube dispersion attributed to the combined use of tip sonication and cyclohexane as dispersion aids during composite processing.

Keywords: *polymer composites, rubber, reinforcements, carbon nanotubes*

---

1. Introduction

Polymer nanocomposites have attracted a huge scientific interest because they allow the design of high-performance materials that exhibit significant improved properties with regard to the pristine polymer. The extent of improvement generally depends on several parameters including the size of the particles, their aspect ratio, their state of dispersion and their surface chemical characteristics that determine the interaction between the filler and the polymer chains and thus the interface of the polymer-filler system [1, 2].

Polymer-carbon nanotube composites have attracted particular interest because the structural characteristics of carbon nanotubes such as their high aspect ratio, high surface area available for stress transfer as well as their exceptionally high Young's modulus and excellent electrical and thermal properties, are expected to allow the emergence of a new generation of ultra-lightweight and extremely strong composite materials [3–5]. In fact, one of the biggest challenges is to obtain a homogeneous dispersion of CNTs in a polymer matrix because van der Waals interactions between individual tubes lead to significant aggregation and agglomeration that reduce the expected property improvements. A homogeneous distribution and a good dispersion are essential for mechanical reinforcement of polymers. In the case of anisotropic electrical conductive inclusions, a good dispersion allows the formation of an inter-

---

[*] Corresponding author, e-mail: Liliane.Bokobza@espci.fr

connecting filler network at a low filler content characterized by a sharp drop, by several orders of magnitude, in the electrical resistivity of the composites reaching the so-called percolation threshold. In fact, it is one of the major attributes of carbon nanotubes to provide electrical conduction at a very low filler loading, this property being required in commercial applications to dissipate electrostatic charge.

This paper reports investigations carried out on natural rubber filled with multiwall carbon nanotubes. The state of nanotube dispersion is evaluated from transmission electron microscopy and electrical properties in the isotropic and uniaxially stretched states of the composite are examined in addition to mechanical measurements.

2. Experimental part

2.1. Materials

Multiwall carbon nanotubes (MWNTs) were purchased from Nanocyl S.A. (Belgium). In this study, we have used the Nanocyl 7000 series (purity: 90%) produced via the catalytic carbon vapor deposition process without any further purification. Their average diameter and length are around 10 nm and 1.5 μm respectively and their surface area between 250 and 300 $m^2 \cdot g^{-1}$.

Non-vulcanized natural rubber, containing all the vulcanization ingredients was provided by Formix (Orléans, France). It was compounded with sulfur (1.5 phr), zinc oxide (3 phr), stearic acid (2 phr), cyclohexylbenzothiazole sulfenamide (1.5 phr), (phr = parts by weight per hundred parts of rubber).

2.2. Composite processing

One of the main factors that have a large influence on the physical performance of a filled composite is the state of filler dispersion within the host polymer matrix. Carbon nanotubes can easily form bundles and this aggregation decreases their aspect ratio and reduces their efficiency as reinforcing agents for high strength polymer composites. Different processing methods, including *in-situ* polymerization, solution mixing, surfactant-assisted processing and melt compounding, have been used to optimize the dispersion of CNTs in the polymeric medium in order to fully exploit the potential of these materials.

In this work, solution mixing which is one of the most common methods, has been used for fabricating MWNTs/NR composites. The general protocol is to mix both components in a suitable solvent and evaporate the latter before proceeding to the cross-linking process and film formation. The most efficient dispersion of the nanotubes in a solvent is achieved by tip sonication with sonication conditions determined in such a way not to degrade the nanotubes.

An appropriate amount of MWNTs was dispersed into cyclohexane (0.1 mg/ml) by sonicating the suspension for 30 min (3 times separated by a rest of 30 min) using a Vibra-Cell VCX 500 operating at 40% amplitude with on and off cycles respectively equal to 4 and 2 seconds. Cyclohexane was used to disperse the nanotubes because it can also dissolve natural rubber and is less dangerous than toluene well known to be is a good solvent for rubbers.

The gum containing the rubber and all the ingredients of formulation was mixed separately in cyclohexane under magnetic stirring until complete dissolution then mixed with the MWNTs dispersion. The mix of polymer and MWNTs dispersions is stirred until evaporation of the major part of cyclohexane then put under vacuum at 50°C for one day for total removal of remaining solvent.

The unfilled and filled samples were then cured into plaques at 170°C during 20 min under a pressure of 120 bar in a standard hot press.

2.3. Characterization techniques

The state of dispersion of the filler particles was examined by transmission electron microscopy (TEM) by means of a JEOL JEM-2010 Electron Microscope, operating at 200 kV. Ultrathin sections (50–60 nm) were cut at –90°C by using an Ultracut S ultramicrotome from Leica fitted with a diamond knife from Diatome.

Electrical resistivity measurements were determined on samples of $10 \times 20 \times 0.2$ mm^3 by measuring their resistance on a high resistance meter (Keithley 6517A) between two conductive rubber electrodes with an alternating voltage of 1 V. This alternating voltage is needed to avoid a background current effect. The measured resistances R were then converted into volume resistivity ρ by using Equation (1):

$$\rho = \frac{RS}{d} \tag{1}$$

where S is the cross-sectional area perpendicular to the current and d the thickness of the sample between the two electrodes.

The strain dependence of electrical resistivity was carried out on strips (size: 40 mm × 6 mm × 0.3 mm) stretched with a manual stretching machine. The film under study is clamped between the jaws of the stretching machine and two copper plates attached to the jaws of the machine are connected to the high-resistance meter.

Under the assumption that the volume remains constant during deformation, the resistivity was obtained from the measured resistance, R, from Equation (2):

$$\rho = \frac{RS_0}{\alpha^2 L_0} \qquad (2)$$

where S_0 and L_0 are respectively, the initial cross-sectional area and length between the two clamps and α is the extension ratio, which is the ratio of the length of the sample in the direction of strain to the initial length before deformation.

The dynamic properties of the vulcanizates were measured by means of a Anton Paar Rheometer at 1 Hz sinusoidal oscillation, using disc specimens with thicknesses of 2 mm, diameters of 8 mm, operated in a shear mode.

The tensile tests were performed at room temperature on a standard tensile Instron machine, model 5565 equipped with a 10 N load cell and a video extensometer. The strips (length around 20 mm between the jaws, width around 5 mm and thickness between 200 and 300 µm) were marked with two dots with a white marker for their recognition by the video extensometer then stretched at a strain rate of 0.1 s^{-1}.

3. Results and discussion

3.1. Transmission electron microscopy analysis (TEM)

The state of dispersion, which significantly affects the electrical and mechanical properties of the material, can be evidenced by TEM analysis of the composites.

TEM images, taken at different scales for the NR composite filled with 3 phr of MWNTs, are seen in Figure 1. Figures 1a–c show a rather homogeneous

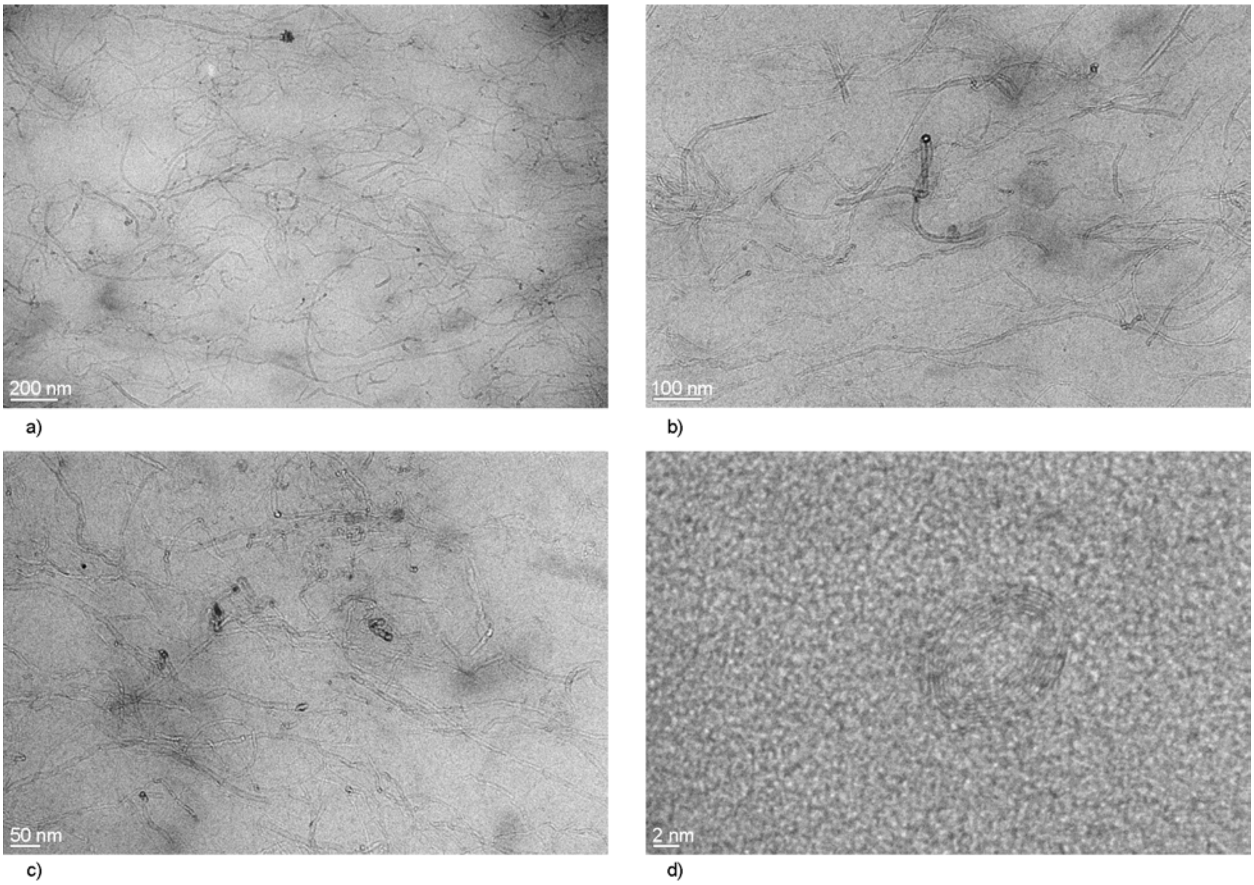

Figure 1. TEM images of NR filled with 3 phr of MWNTs taken at different (a, b, c) scales. d) shows the graphene layers of an individual tube

distribution of the nanotubes in the elastomeric matrix and in Figure 1d are magnified the graphene shells with the hollow core of an individual tube.

3.2. Electrical properties

Carbon nanotubes have largely demonstrated their ability to provide electrical conduction when incorporated into polymeric media usually considered as electrical insulators. From a great number of results in the literature, it is now evident that very small quantities of carbon nanotubes are required to get relatively high values of electrical conductivity and this property is expected to open the way for a wide range of industrial applications.

The electrical conduction process depends on several parameters, mainly on filler concentration. But processing techniques intended to improve dispersion of CNTs in the host matrix also influence the electrical conductivity of the final material. On the other hand, factors such as nanotube type, polymer matrix, filler-matrix interactions and filler orientation are key factors in determining the electrical properties. At a given amount of conductive particles (carbon black or carbon nanotubes), called the percolation threshold, a continuous network of filler is formed across the matrix and the material undergoes a sudden transition from an insulator to a conductor. For composites containing conventional conducting fillers such as carbon black (CB), carbon nanofibers or graphite, depending on the structural properties of the particles, the percolation threshold is achieved for a filler content as high as 10–50 wt%, which may result in a composite with poor mechanical properties and high density. Thongruang *et al.* [6] showed that the percolation-threshold concentration in composites is around 10–15 wt% for carbon fiber and high structure carbon black and around 40–50 wt% for low structure carbon black and graphite. Carbon nanotubes yield adequate conductivity at a much lower filler content on account of their high aspect ratios thus retaining the desired mechanical properties of the resulting material. Another way to enhance electrical conductivity has been shown to incorporate simultaneously hybrid fillers of carbon nanotubes and carbon black [7, 8]. It was demonstrated that when CB particles are added into the nanocomposites containing CNTs, the result is a better overall dispersion due to synergistic effects arising between the two different fillers and the formation of connected structures by bridging uncontacted particles. But, the replacement of carbon black by carbon nanotubes alone for the synthesis of electrically conducting polymer composites is very promising for the design of lightweight materials for numerous future applications.

As seen in Figure 2 which shows the effect of filler loading on the volume resistivity of MWNTs-filled composites based on insulating natural rubber, the decrease in resistivity is observed from 0.5 to 1 phr. According to Mamunya *et al.* [9], at the beginning of the transition region, an infinite conductive cluster is formed and, consequently, the composite becomes conductive. The higher aspect ratio of the nanotube bundles which increases the probability of particle-particle contacts explain the low percolation threshold. With regard to previous reported results [10], thanks to improved dispersion methods, the percolation threshold is shifted to a lower nanotube content and from this point of view, measurements of electrical resistivity appears as an indirect tool to evaluate the state of dispersion. As mentioned above, an important factor that controls the performance and especially the electrical properties of CNTs-reinforced composites is the state of dispersion of CNTs.

Because the resistivity is very sensitive to any change in filler distribution, electrical properties of composite filled with conductive particles should be affected by a mechanical deformation. Significant changes in electrical conductivity against degree of elongational strain have already been reported in the literature [11–15].

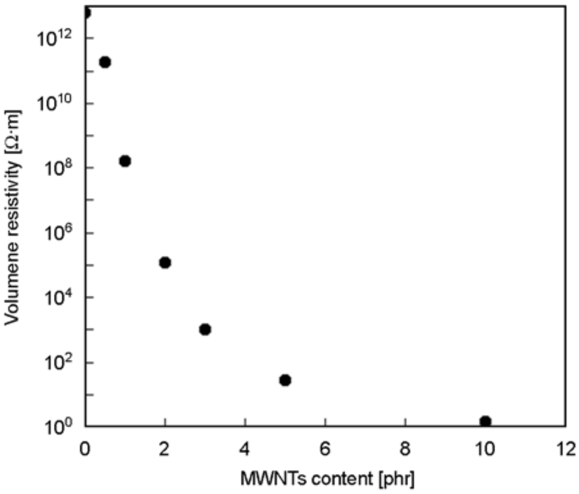

Figure 2. Volume resistivity against nanotube loading for NR composites

Typical strain dependences of volume resistivity are shown in Figure 3: the results are related to a NR sample filled with 3 phr of MWNTs that is at a filler content above the percolation threshold (determined around 0.5 phr of filler). Tests are performed as follows:

- 1: stretching to ε = 100% then release,
- 2 and 3: second stretching to ε = 200% then release,
- 4 and 5: third stretching until failure.

A gradual increase in resistivity is obtained in the first step as result of a breakdown of contacts and increasing distances between the conducting inclusions. After total unloading of the sample (step 2), the resistivity is much higher than that observed for the undeformed material thus showing that the contacts are not reformed after removal of the stress. A second stretching leads to a decrease in resistivity until the point where the first and second stretching meet. At this point, we can consider that the sample is in the same state as it was at the first stretching. It is interesting to point out that this part of the curve (unloading + second stretch) is completely reversible as shown in the paper of Ciselli *et al.* [16] related to composites based on ethylene-propylene-diene-monomer (EPDM) filled with MWNTs. After the point where the first and second stretchings meet, the curve join up the first stretching curve till ε = 200% (step 3) and the resistivity increases again due to the breakdown of new contacts that were not affected during the first stretching. A further removal of the stress leads to a higher value of resistivity than that obtained in the first unloading cycle and the third stretching displays a decreease (step 4) then increase (step 5). The strain dependence of electrical resistivity described here for NR composites is quite similar to that obtained in other rubbery matrices like SBR [17] or EPDM [18].

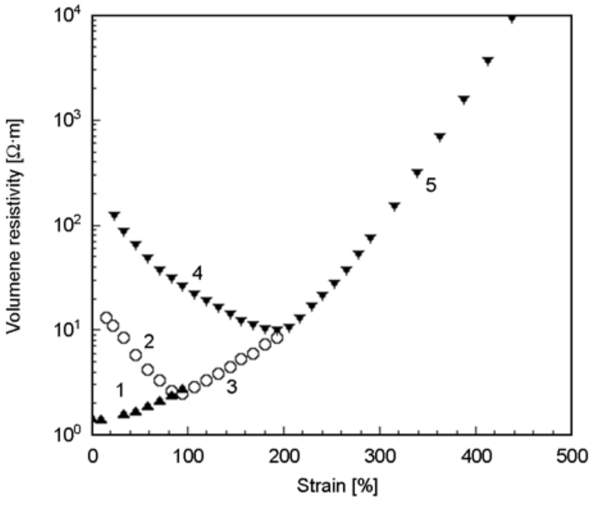

Figure 3. Strain dependence of the electrical resistivity for NR filled with 3 phr of MWNTs

3.3. Mechanical properties

3.3.1. Low-strain dynamic behavior

Filled elastomers have the specific ability to dissipate an important part of mechanical energy during deformation. At small strains (typically for shear strains below 100%), those materials exhibit a non-linear viscoelastic behavior, known as the 'Payne effect' and characterized by a drop in the elastic modulus G' when the shear strain amplitude increases.

The Payne effect in composites filled with conventional fillers (carbon black or silica) has been the subject of numerous studies on both experimental and theoretical aspects [19–22] but its origin is still controversial. The most commonly accepted picture is the breakdown of a filler network formed by filler-filler interactions. The percolated network is progressively broken by increasing the strain amplitude.

Figure 4 displays the strain dependence of the storage modulus of the unfilled NR and of MWNTs-filled composites. While the unfilled elastomer does not display any change in the storage modulus with strain amplitude, at least in the investigated strain domain, the observed behaviors for filled compounds are similar to what was mentioned in the lit-

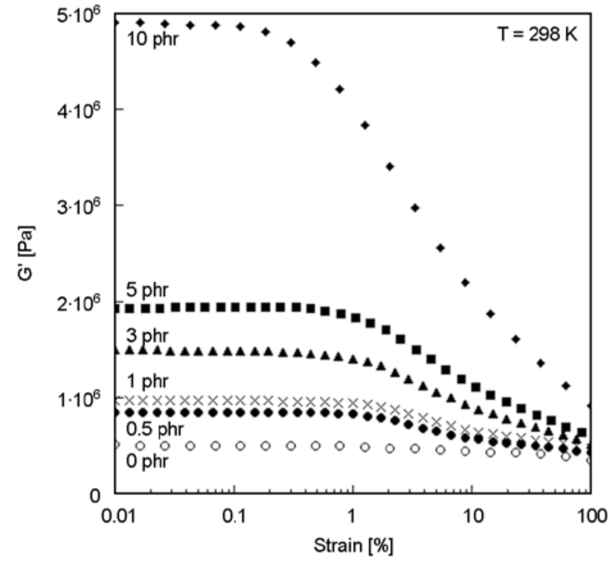

Figure 4. Strain dependence of the storage modulus of unfilled NR and of MWNTs/NR composites at room temperature

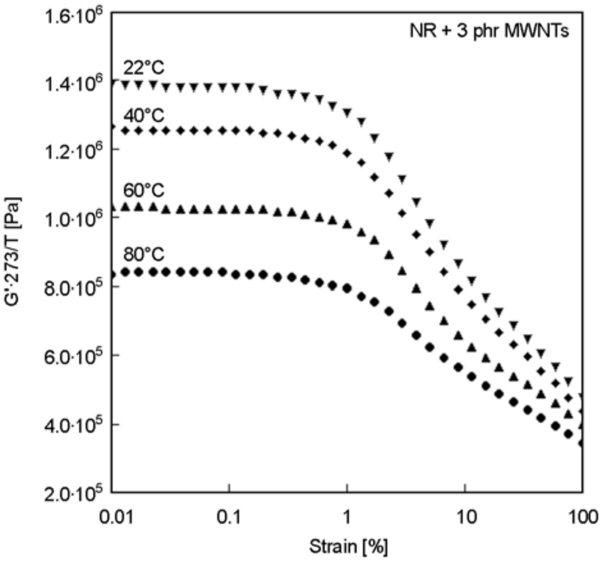

Figure 5. Temperature dependence of the storage modulus for NR filled with 3 phr of MWNTs

erature for carbon-black filled rubbers, that is an increase in amplitude of the Payne effect with the amount of reinforcing particles, because the linear part of the storage modulus typically below 0.1% strain strongly increases with the filler loading. But as shown in Figure 4, a Payne effect is observed till 0.5 phr while much larger amounts of carbon black are required to give rise to a storage modulus drop with the strain amplitude [23].

In the case of an unfilled rubber network, the modulus should increase proportionally with temperature because of its entropic nature. For all the filled systems, the modulus values should then be corrected by the entropic factor 273/T, in order to get rid of the modulus dependence of the rubber part due to temperature [20]. As a typical example, the temperature dependence of the storage modulus is shown in Figure 5 for the 3 phr MWNTs/NR composite. As already observed in conventional composites, the amplitude of the Payne effect decreases with increasing temperature which is opposite to the entropic variation characteristic of the unfilled network [23-25]. The decrease of the Payne effect results from a weakening of filler-filler interactions by raising the temperature.

3.3.2. Tensile properties

A common objective for adding fillers into polymers is to increase the modulus or stiffness. Composite theories have been developed in order to predict the performance of the composite by taking into account various filler parameters including geometry, stiffness and orientation [26–28]. In polymer-clay nanocomposites, it was demonstrated that the superior reinforcement provided by exfoliated layered aluminosilicates with regard to a conventional filler like glass fibers, arises primarily from the combination of high modulus and aspect ratio of the nanofiller [27].

As seen in Figure 6a which represents the strain dependence of the nominal stress for pure NR and for composites, considerable improvement in stiffness is observed upon addition of MWNTs in the NR matrix. In order to evaluate the extent of improvement with the nanotube loading, the stress at 100% strain is displayed in Figure 6b.

The stress-strain curve for unfilled NR exhibits a large increase in stress at higher deformations. NR

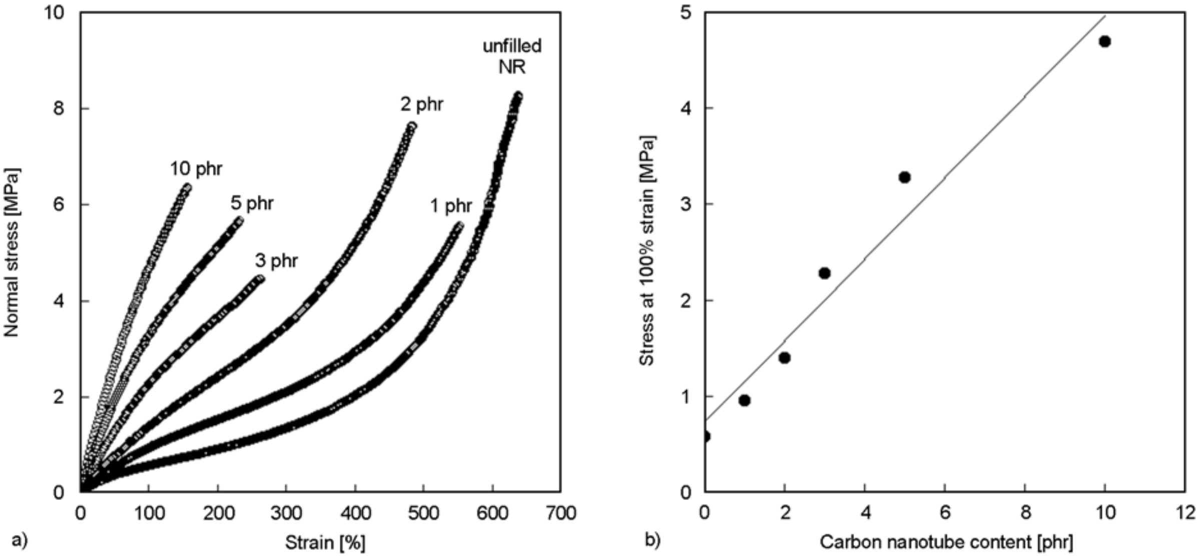

Figure 6. Stress-strain curves (a) and stress at 100% for pure NR and MWNTs composites (b)

displays, due to its uniform microstructure, a very unique important characteristic, that is, the ability to crystallize under strain, a phenomenon known as strain-induced crystallization. This phenomenon is responsible for the large and abrupt increase in the reduced stress observed at higher deformation corresponding, in fact, to a self-toughening of the elastomer because the crystallites act as additional cross-links in the network. This process can be better visualized by using a Mooney-Rivlin representation, based on the so-called Mooney-Rivlin equation (Equation (3)):

$$[\sigma^\star] = \frac{\sigma}{\alpha - \alpha^{-2}} = 2C_1 + 2C_2\alpha^{-1} \qquad (3)$$

where σ is the nominal stress, α is the extension ratio and $2C_1$ and $2C_2$ are constants independent of α. The curves of the unfilled vulcanizate displays, at higher deformations, an upturn in the modulus ascribed to the strain-induced crystallization of polymer chains (Figure 7). For the composites filled with 1 and 2 phr, the upturn is still observed but it starts at a lower extension ratio than that of the unfilled sample. That means that the addition of carbon nanotubes favors the crystallization process. This fact has already been established by infrared spectroscopy under strain [29] and by synchroton wide-angle X-ray diffraction [30]. The reduction in the strain at rupture for the other composites does not allow the observation of the tensile behaviour at high deformations. Unfortunately, the rupture properties are negatively affected by the nanotubes probably on account of the presence of some agglomerates which act as failure points and lead to a degradation of the mechanical properties of the materials. The stress at 100% deformation is seen to increase linearly with the MWNTs loading (Figure 6b). With regard to the pure polymer, 10 phr of MWNTs leads to more than a 700% increase in the stress at 100% strain. The observed improvements are higher than those previously obtained in the literature for the same polymer [10, 29, 31–36].

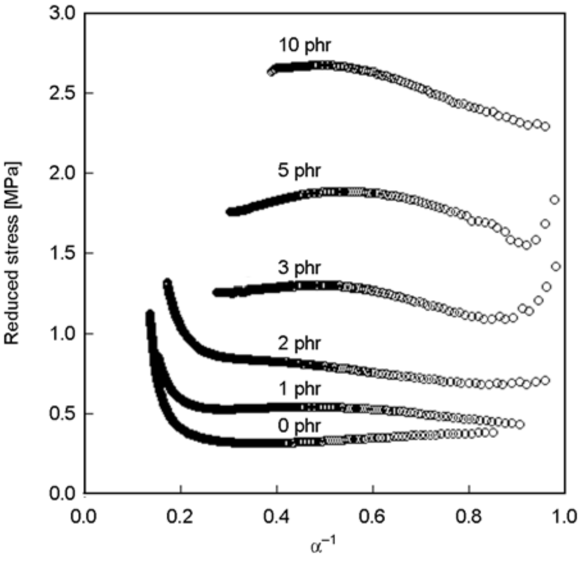

Figure 7. Mooney-Rivlin plots for pure NR and MWNTs/NR composites

Such increases in stiffness are not observed for similar loading fractions of spherical carbon black or silica particles in the same matrix, thus highlighting the effect of the high aspect ratio (length/diameter) of the nanotubes. In conventional composites, the increase in the modulus has been ascribed to a hydrodynamic effect arising from the inclusion of rigid particles in the soft matrix and to an increase in the cross-linking density created by polymer-filler interactions [1, 2, 26, 37–40]. But the anisometry of the filler structures as well as the quality of their dispersion can greatly affect the composite performance. The latter point is especially true for entangled MWNTs in which the occluded rubber trapped inside the bundles and partially shielded from deformation, increases the effective filler concentration.

To interpret the variation of stiffness of the polymeric composites with the MWNTs amount, the 100% modulus results are fitted to the model of Halpin-Tsai [41]. intended to predict the mechanical properties of fibre reinforced composites. This model (Equation (4)) yields, for aligned fibre composites and in conditions where the modulus of the fiber, E_f, is much higher than that of the unfilled matrix (as in elastomeric composites):

$$E = E_0\frac{1 + f\varphi}{1 - \varphi} \qquad (4)$$

(E and E_0 are the moduli of the composite and the unfilled elastomer respectively, f is the aspect ratio and φ, the volume fraction of filler).

The experimental values are compared with the Halpin-Tsai predictions using an aspect ratio of 90 to fit the data (Figure 8). This value is lower than expected from the average dimensions of the MWNTs but much higher than those previously pub-

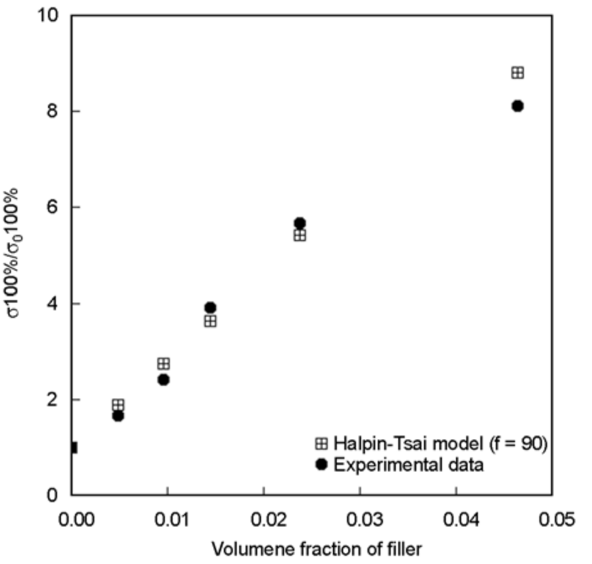

Figure 8. Dependence of the stress at 100% strain of NR/MWNTs composites on the filler volume fraction and comparison with predictions of theoretical models

lished for hydrocarbon rubber/MWNTs composites [42, 43] as a result from a better filler dispersion.

Besides the state of dispersion, another fundamental issue that determines the properties of the composite is the interfacial interaction between the polymer and the nanotubes. A good adhesion between the two phases is required and might result in better load transfer from the matrix to the nanotube [44]. Raman spectroscopy under strain has also been used to probe interactions between carbon nanotubes and polymers in nanotube-based composites. If the nanotubes are carrying strain, the Raman peaks of carbon nanotubes have been shown to exhibit shifts upon application of a mechanical deformation to the composite. Large downshifts up to 20 cm^{-1} at about 1% strain have been observed for the *G′* band of SWNTs in stiff polymers such as epoxy resins [44–46]. In our rubbery composites, no significant shift of the *G′* band has been observed which means that load transfer to the nanotubes is negligible. However, in our experiments, we obtain an upshift in frequency of the *G* mode (ascribed to the stretching of the C–C bond of the carbon materials) with an increase in strain. The upshift of the *G* mode has been attributed to nanotube-nanotube decoupling within the bundle because the upshift is not reversible with strain [47, 48].

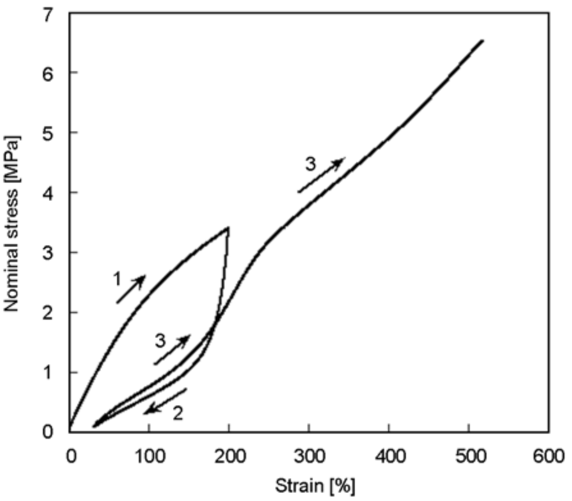

Figure 9. Loading-unloading cycles performed on NR filled with 3 phr of MWNTs

Some hysteresis (area between the first and second stretches) is also observed in carbon nanotube-filled samples while the unfilled sample does not display any significant stress softening effect. In the experiment presented in Figure 9, the composite was stretched to a strain of 200% , then released and re-stretched till the rupture of the sample. In view of our Raman results, we are in a position to believe that there is a poor adhesion between the nanotube surface and the rubber. Consequently, the stress-softening effect does not originate as in the case of conventional composites from a loss of elastic chains taking place at the polymer-filler interface [49]. In previous papers [42, 50], we have suggested a loss of nanotube orientation on releasing the strain to explain the lowering in the stress in the second stretching. Despite the fact that we cannot overlook the large contribution of orientational aspects in the stress-strain behavior of composites, we can also consider that a significant effect of the strain is a debundling of the agglomerates still remaining in the polymeric medium. This interpretation is supported by the fact that the rupture of the sample in the second stretching occurs at a much higher value of strain than that obtained in the first stretching curve (compare Figure 6a and 9).

4. Conclusions

This paper demonstrates that optimized processing conditions used to achieve good dispersion lead to composites with high mechanical and electrical properties. Nevertheless, the presence of a small number of agglomerates acting as defects are responsible of the lack of improvement in rupture properties. Comparison of the experimental tensile measurements with the Halpin-Tsai model leads an aspect ratio of 90 for carbon nanotubes. This high aspect ratio appears to be the main parameter for mechanical reinforcement and electrical conduction. The high aspect ratio also explains the formation of a filler network at a low nanotube loading. Application of an uniaxial deformation to the composite leads to an increase of electrical resistivity while a drop in the storage modulus is observed when the sample is submitted to low shear strains. Both effects are attributed to the breakdown of the filler network.

Acknowledgements

This work has been carried out with the help of the 'Prix de la Recherche Jean Langlois 2009'. The author thanks Gilles Garnaud, Bettina Subtil and Sandra Hilaire for technical assistance.

References

[1] Bokobza L.: Elastomeric composites. I. Silicone composites. Journal of Applied Polymer Science, **93**, 2095–2104 (2004).
DOI: 10.1002/app.20684

[2] Bokobza L.: The reinforcement of elastomeric networks by fillers. Macromolecular Materials and Engineering, **289**, 607–621 (2004).
DOI: 10.1002/mame.200400034

[3] Khare R., Bose S.: Carbon nanotube based composites – A review. Journal of Minerals and Materials Characterization and Engineering, **4**, 31–46 (2005).

[4] Hu Y., Shenderova O. A., Hu Z., Padgett C. W., Brenner D. W.: Carbon nanostructures for advanced composites. Reports on Progress in Physics, **69**, 1847–1895 (2006).
DOI: 10.1088/0034-4885/69/6/R05

[5] Spitalsky Z., Tasis D., Papagelis K., Galiotis C.: Carbon nanotube-polymer composites: Chemistry, processing, mechanical and electrical properties. Progress in Polymer Science, **35**, 357–401 (2010).
DOI: 10.1016/j.progpolymsci.2009.09.003

[6] Thongruang W., Balik C. M., Spontak R. J.: Volume-exclusion effects in polyethylene blends filled with carbon black, graphite, or carbon fiber. Journal of Polymer Science Part B: Polymer Physics, **40**, 1013–1025 (2002).
DOI: 10.1002/polb.10157

[7] Bokobza L., Rahmani M., Belin C., Bruneel J-L., El Bounia N-E.: Blends of carbon blacks and multiwall carbon nanotubes as reinforcing fillers for hydrocarbon rubbers. Journal of Polymer Science Part B: Polymer Physics, **46**, 1939–1951 (2008).
DOI: 10.1002/polb.21529

[8] Ma P-C., Liu M-Y., Zhang H., Wang S-Q., Wang R., Wang K., Wong Y-K., Tang B-Z., Hong S-H., Paik K-W., Kim J-K.: Enhanced electrical conductivity of nanocomposites containing hybrid fillers of carbon nanotubes and carbon black. ACS Applied Materials and Interfaces, **1**, 1090–1096 (2009).
DOI: 10.1021/am9000503

[9] Mamunya Ye. P., Davydenko V. V., Pissis P., Lebedev E. V.: Electrical and thermal conductivity of polymers filled with metal powders. European Polymer Journal, **38**, 1887–1897 (2002)
DOI: 10.1016/S0014-3057(02)00064-2

[10] Bokobza L., Kolodziej M.: On the use of carbon nanotubes as reinforcing fillers for elastomeric materials. Polymer International, **55**, 1090–1098 (2006).
DOI: 10.1002/pi.2064

[11] Das N. C., Chaki T. K., Khastgir D.: Effect of axial stretching on electrical resistivity of short carbon fibre and carbon black filled conductive rubber composites. Polymer International, **51**, 156–163 (2002).
DOI: 10.1002/pi.811

[12] Yamaguchi K., Busfield J. J. C., Thomas A. G.: Electrical and mechanical behavior of filled elastomers. I. The effect of strain. Journal of Polymer Science Part B: Polymer Physics, **41**, 2079–2089 (2003).
DOI: 10.1002/polb.10571

[13] Busfield J. J. C., Thomas A. G., Yamaguchi K.: Electrical and mechanical behavior of filled elastomers 2: The effect of swelling and temperature. Journal of Polymer Science Part B: Polymer Physics, **42**, 2161–2167 (2004).
DOI: 10.1002/polb.20085

[14] Kang J. H., Park C., Scholl J. A., Brazin A. H., Holloway N. M., High J. W., Lowther S. E., Harrison J. S.: Piezoresistive characteristics of single wall carbon nanotube/polyimide nanocomposites. Journal of Polymer Science Part B: Polymer Physics, **47**, 994–1003 (2009).
DOI: 10.1002/polb.21705

[15] Kujawski M., Pearse J. D., Smela E.: Elastomers filled with exfoliated graphite as compliant electrodes. Carbon, **48**, 2409–2417 (2010).
DOI: 10.1016/j.carbon.2010.02.040

[16] Ciselli P., Lu L., Busfield J. J. C., Peijs T.: Piezoresistive polymer composites based on EPDM and MWNTs for strain sensing applications. e-Polymers, no.014 (2010).

[17] Bokobza L.: New developments in rubber reinforcement. Kautschuk Gummi Kunststoffe, **62**, 23–27 (2009).

[18] Bokobza L.: Enhanced electrical and mechanical properties of multiwall carbon nanotube rubber composites. Polymers for Advanced Technologies, submitted (2011).

[19] Wang M-J.: Effect of polymer-filler and filler-filler interactions on dynamic properties of filled vulcanizates. Rubber Chemistry and Technology, **71**, 520–589 (1998).
DOI: 10.5254/1.3538492

[20] Clément F., Bokobza L., Monnerie L.: Investigation of the Payne effect and its temperature dependence on silica-filled polydimethylsiloxane networks. Part I: Experimental results. Rubber Chemistry and Technology, **78**, 211–231 (2005).
DOI: 10.5254/1.3547879

[21] Clément F., Bokobza L., Monnerie L.: Investigation of the Payne effect and its temperature dependence on silica-filled polydimethylsiloxane networks. Part II: Test of quantitative models. Rubber Chemistry and Technology, **78**, 232–244 (2005).
DOI: 10.5254/1.3547880

[22] Ramier J., Gauthier C., Chazeau L., Stelandre L., Guy L.: Payne effect in silica-filled styrene–butadiene rubber: Influence of surface treatment. Journal of Polymer Science Part B: Polymer Physics, **45**, 286–298 (2007).
DOI: 10.1002/polb.21033

[23] Payne A. R.: The dynamic properties of carbon black-loaded natural rubber vulcanizates. Part I. Journal of Applied Polymer Science, **6**, 57–63 (1962).
DOI: 10.1002/app.1962.070061906

[24] Payne A. R., Whittaker R. E.: Low strain dynamic properties of filled rubbers. Rubber Chemistry and Technology, **44**, 440–478 (1971).
DOI: 10.5254/1.3547375

[25] Maier P. G., Göritz D.: Molecular interpretation of the Payne effect. Kautschuk Gummi Kunststoffe, **49**, 18–24 (1996).

[26] Ahmed S., Jones F. R.: A review of particulate reinforcement theories for polymer composites. Journal of Materials Science, **25**, 4933–4942 (1990).
DOI: 10.1007/BF00580110

[27] Fornes T. D., Paul D. R.: Modeling properties of nylon 6/clay nanocomposites using composite theories. Polymer, **44**, 4993–5013 (2003).
DOI: 10.1016/S0032-3861(03)00471-3

[28] Wu Y-P., Jia Q-X., Yu D-S., Zhang L-Q.: Modeling Young’s modulus of rubber–clay nanocomposites using composite theories. Polymer Testing, **23**, 903–909 (2004)
DOI: 10.1016/j.polymertesting.2004.05.004

[29] Kolodziej M., Bokobza L., Bruneel J-L.: Investigations on natural rubber filled with multiwall carbon nanotubes. Composite Interfaces, **14**, 215–228 (2007).
DOI: 10.1163/156855407780340304

[30] Weng G., Huang G., Qu L., Nie Y., Wu J.: Large-scale orientation in a vulcanized stretched natural rubber network: Proved by in situ synchrotron X-ray diffraction characterization. The Journal of Physical Chemistry B, **114**, 7179–7188 (2010).
DOI: 10.1021/jp100920g

[31] Fakhru’l-Razi A., Atieh M. A., Girun N., Chuah T. G., El-Sadig M., Biak D. R. A.: Effect of multi-wall carbon nanotubes on the mechanical properties of natural rubber. Composite Structures, **75**, 496–500 (2006).
DOI: 10.1016/j.compstruct.2006.04.035

[32] Bhattacharyya S., Sinturel C., Bahloul O., Saboungi M-L., Thomas S., Salvetat J-P.: Improving reinforcement of natural rubber by networking of activated carbon nanotubes. Carbon, **46**, 1037–1045 (2008).
DOI: 10.1016/j.carbon.2008.03.011

[33] Cataldo F., Ursini O., Angelini G.: MWCNTs elastomer nanocomposite, Part 2: The addition of MWCNTs to an oil-extended SBR-based carbon black-filled rubber compound. Fullerenes, Nanotubes and Carbon Nanostructures, **17**, 55–66 (2009).
DOI: 10.1080/15363830802515923

[34] Nah C., Lim J. Y., Cho B. H., Hong C. K., Gent A. N.: Reinforcing rubber with carbon nanotubes. Journal of Applied Polymer Science, **118**, 1574–1581 (2010).
DOI: 10.1002/app.32524

[35] Sui G., Zhong W. H., Yang X. P., Yu Y. H.: Curing kinetics and mechanical behavior of natural rubber reinforced with pretreated carbon nanotubes. Materials Science and Engineering: A, **485**, 524–531 (2008).
DOI: 10.1016/j.msea.2007.09.007

[36] Ismail H., Ramly F., Othman N.: Multiwall carbon nanotube-filled natural rubber: The effects of filler loading and mixing method. Polymer-Plastics Technology and Engineering, **49**, 260–266 (2010).
DOI: 10.1080/03602550903413888

[37] Dannenberg E. M.: The effects of surface chemical interactions on the properties of filler-reinforced rubbers. Rubber Chemistry and Technology, **48**, 410–444 (1975).
DOI: 10.5254/1.3547460

[38] Wagner M. P.: Reinforcing silicas and silicates. Rubber Chemistry and Technology, **49**, 703–774 (1976).
DOI: 10.5254/1.3534979

[39] Voet A.: Reinforcement of elastomers by fillers: Review of period 1967–1976. Journal of Polymer Science: Macromolecular Reviews, **15**, 327–373 (1980).
DOI: 10.1002/pol.1980.230150107

[40] Edwards D. C.: Polymer-filler interactions in rubber reinforcement. Journal of Materials Science, **25**, 4175–4185 (1990).
DOI: 10.1007/BF00581070

[41] Halpin J. C.: Stiffness and expansion estimates for oriented short fiber composites. Journal of Composite Materials, **3**, 732–734 (1969).
DOI: 10.1177/002199836900300419

[42] Bokobza L.: Multiwall carbon nanotube elastomeric composites: A review. Polymer, **48**, 4907–4920 (2007).
DOI: 10.1016/j.polymer.2007.06.046

[43] Perez L. D., Zuluaga M. A., Kyu T., Mark J. E., Lopez B. L.: Preparation, characterization, and physical properties of multiwall carbon nanotube/elastomer composites. Polymer Engineering and Science, **49**, 866–874 (2009).
DOI: 10.1002/pen.21247

[44] Frogley M. D., Ravich D., Wagner H. D.: Mechanical properties of carbon nanoparticle-reinforced elastomers. Composites Science and Technology, **63**, 1647–1654 (2003).
DOI: 10.1016/S0266-3538(03)00066-6

[45] Cooper C. A., Young R. J., Halsall M.: Investigation into the deformation of carbon nanotubes and their composites through the use of Raman spectroscopy. Composites Part A: Applied Science and Manufacturing, **32**, 401–411 (2001).
DOI: 10.1016/S1359-835X(00)00107-X

[46] Kao C. C., Young R. J.: A Raman spectroscopic investigation of heating effects and the deformation behaviour of epoxy/SWNT composites. Composites Science and Technology, **64**, 2291–2295 (2004).
DOI: 10.1016/j.compscitech.2004.01.019

[47] Bokobza L.: Vibrational spectroscopic and mechanical investigation of carbon nanotube-reinforced styrene-butadiene rubbers. Macromolecular Symposia, **305**, 1–9 (2011).
DOI: 10.1002/masy.201000119

[48] Bokobza L.: A Raman investigation of carbon nanotubes embedded in a soft polymeric matrix. Journal of Inorganic and Organometallic Polymers and Materials, in press (2011).
DOI: 10.1007/s10904-011-9590-7

[49] Clément F., Bokobza L., Monnerie L.: On the Mullins effect in silica-filled polydimethylsiloxane networks. Rubber Chemistry and Technology, **74**, 847–870 (2001).
DOI: 10.5254/1.3547657

[50] Bokobza L., Belin C.: Effect of strain on the properties of a styrene–butadiene rubber filled with multiwall carbon nanotubes. Journal of Applied Polymer Science, **105**, 2054–2061 (2007).
DOI: 10.1002/app.26153

eXPRESS Polymer Letters Vol.6, No.3 (2012) 224–236
Available online at www.expresspolymlett.com
DOI: 10.3144/expresspolymlett.2012.25

Tensile and impact properties of three-component PP/wood/elastomer composites

G. Keledi[1,2], *A. Sudár*[1,2], *Ch. Burgstaller*[3], *K. Renner*[1,2], *J. Móczó*[1,2], *B. Pukánszky*[1,2*]

[1]Laboratory of Plastics and Rubber Technology, Department of Physical Chemistry and Materials Science, Budapest University of Technology and Economics, H-1521 Budapest, P.O. Box 91, Hungary
[2]Institute of Materials and Environmental Chemistry, Chemical Research Center, Hungarian Academy of Sciences, H-1525 Budapest, P.O. Box 17, Hungary
[3]Transfercenter für Kunststofftechnik GmbH, Franz-Fritsch-Strasse 11, A-4600 Wels, Austria

Received 13 July 2011; accepted in revised form 2 October 2011

Abstract. Polypropylene (PP) was reinforced with wood flour and impact modified with elastomers to increase stiffness and impact resistance simultaneously. Elastomer content changed in four (0, 5, 10 and 20 wt%), while that of wood content in seven steps, the latter from 0 to 60 wt% in 10 wt% steps. Structure and adhesion were controlled by the addition of functionalized (maleated) polymers. Composites were homogenized in a twin-screw extruder and then injection molded to tensile bars. Fracture resistance was characterized by standard and instrumented impact tests. The results showed that the components are dispersed independently of each other even when a functionalized elastomer is used for impact modification, at least under the conditions of this study. Impact resistance does not change much as a function of wood content in PP/wood composites, but decreases drastically from the very high level of the PP/elastomer blend to almost the same value obtained without impact modifier in the three-component materials. Increasing stiffness and fiber related local deformation processes led to small fracture toughness at large wood content. Micromechanical deformation processes depend mainly on the strength of PP/wood interaction; debonding and pull-out take place at poor adhesion, while fiber fracture dominates when adhesion is strong. Composites with sufficiently large impact resistance cannot be prepared in the usual range of wood contents (50–60 wt%).

Keywords: *damage mechanism, PP/wood composites, impact modification, interfacial adhesion, composite structure*

1. Introduction

Wood flour and natural fibers are used in increasing quantities mainly for the reinforcement of commodity polymers [1–3]. Such reinforcements have many advantages over particulate fillers or glass fibers; they increase stiffness considerably, they are obtained from renewable resources, are available in abundant quantities, cheap, and light at the same time [2, 4, 5]. Major application areas of these materials are the building and the automotive industries. In structural applications often large stiffness and impact resistance are required simultaneously, which are achieved traditionally by the combination of several functional additives. Composites used as bumper materials, for example, usually contain an elastomer to improve impact resistance and a filler or fiber to increase stiffness [6–8]. Research has started as early as the 80's on these materials [6, 9–12] and they have been commercially available for several decades.

Structure can be quite complicated in such multicomponent materials. Two boundary structures may form in them: the two components, i.e. the elastomer and the filler, can be distributed separately

---

[*]Corresponding author, e-mail: bpukanszky@mail.bme.hu

from each other in the polymer matrix [13–15], or the elastomer can encapsulate the reinforcement to create embedded structure [6–8, 16]. The actual structure is determined by the adhesion and shear forces prevailing in the melt during homogenization, the first favoring embedding because of thermodynamic reasons, while the second separate dispersion through the shearing apart of the elastomer layer from the wood fiber [17]. Usually intermediate structures form in composites produced under practical conditions, a part of the filler is embedded into the elastomer phase, but individual elastomer droplets and filler particles can be also located in the matrix. Structure can be tailored by the control of interfacial adhesion through the use of appropriate coupling agents [18–21]. Functionalized polymers are used to control structure in polypropylene. The introduction of maleated PP (MAPP) leads almost exclusively to the separate dispersion of the components. The reaction of the maleic anhydride group with the wood fibers creates strong covalent bonds, on the one hand, and the interdiffusion of MAPP forms entanglements with the matrix polymer, on the other, resulting in strong adhesion and good stress transfer as well [22–24]. Adhesion force changes from about 100 mJ/m^2 to nearly 1000 mJ/m^2 in this way [25]. The addition of maleated ethylene-propylene-diene elastomer (MAEPDM), on the other hand, results in a large extent of embedding. Properties change considerably with structure even at the same composition. Stiffness was shown to depend mainly on the extent of embedding, while impact resistance was influenced also by other factors including micromechanical deformation processes occurring around the inclusions (elastomer, filler) [26].

It seems to be obvious to use wood and/or natural fibers to replace mineral fillers or glass fibers also in such composites. However, wood flour differs considerably from traditional reinforcements. Wood particles are large, usually several 100 µm in size, which facilitates debonding, the separation of the matrix/filler interface already at small stresses [27–29]. A functionalized polymer coupling agent is needed practically always in order to achieve reasonable properties, at least in polyolefin composites. Besides debonding, large wood particles may initiate other micromechanical deformation processes during the deformation of the composites like fiber pull-out, or fiber fracture at strong interfacial adhesion [29, 30]. These differences compared to particulate fillers and glass fibers, and the tendency to replace traditional reinforcements with natural ones require more detailed study of the behavior of multicomponent materials containing wood fibers. Very few papers have been published in this area yet. A model study was carried out on the recycling of PP/PE blends by Clemons [31], and functionalized elastomers were used to modify structure and properties in PP/wood composites by Oksman and Clemons [32, 33]. Since impact resistance is one of the crucial properties in structural materials, the goal of our study was to investigate the effect of structure and interfacial adhesion on fracture toughness in wood reinforced multicomponent PP composites impact modified with elastomers. An attempt was made to control structure and adhesion by the use of functionalized polymers. Wood content changed in a wide, industrially relevant range. Besides the effect of wood content on fracture resistance, we tried also to identify the mechanism of failure in these composites.

2. Experimental

The polymer used in the study was the Tipplen H 781 F grade PP homopolymer (MFR = 0.7 g/10 min at 230°C and 2.16 kg load) produced by TVK, Tiszaújváros, Hungary. The Vistalon 706 ethylene-propylene-diene (EPR) elastomer (ethylene content: 65 wt%, Mooney viscosity ML1+4 at 125°C: 42) of Exxon Mobil, Houston, USA was used to increase impact resistance. The functionalized polymers applied for the control of structure and interfacial adhesion were the Orevac CA 100 grade maleated PP (MFI = 150–200 g/10 min at 230°C and 2.16 kg, MA content: 1.0 wt%) from Arkema, Puteaux, France and the Exxcellor VA 1803 maleated EPDM (ethylene content: 43 wt%, MFI = 3 g/10 min at 230°C and 2.16 kg, MA content: 0.5–1.0 wt%) from Exxon Mobil, Houston, USA. We hoped that the application of the first leads to separate dispersion, while the second to the complete encapsulation of wood particles. The Filtracel EFC 1000 wood flour was supplied by Rettenmaier and Söhne GmbH, Rosenberg, Germany. The wood was treated to remove waxes by the producer, it contained 70.4 wt% holocellulose, 28.7 wt% lignin and 0.9 wt% waxes. The filler had an average particle size of 210 µm as determined by laser light scattering. Scanning electron microscopic (SEM) analysis of particle geometry showed average particle length of 363 µm, diameter of 64 µm and aspect ratio of 6.8. MAPP was always added in 10 wt% calculated for the amount of wood [34], while 5, 10 and 20 wt% of the matrix polymer was replaced by impact modifier (EPR or MAEPDM). Wood content changed from 0 to 60 wt% in 10 wt% steps related to the total weight of the composites.

The composites were homogenized using a ThermoPrism TSE 24 (Thermo Fisher Sci. Inc., Waltham, USA) twin-screw extruder with a screw diameter of 24 mm and an L/D ratio of 28. Screw configuration included two kneading zones with different lengths and conveying elements. The polymer components were introduced into the hopper, while wood was added to the melt through a side feeder. Zone temperatures changed from 170 to 220°C in 10°C steps in the six zones of the extruder. The granulated material was dried for 4 hours at 105°C in an oven and then injection molded to standard ISO 527 1A tensile specimens using a Demag IntElect 50 machine (Demag Ergotech GmbH, Schwaig, Germany) at 170–180–190–200–210°C zone and 50°C mold temperatures, 50 mm/s injection rate, max 1300 bar holding pressure and 25 sec holding time. The samples were conditioned at 23°C and 50% RH for a week before testing.

Tensile testing was carried out with an Instron 5566 type machine (Instron Corp., Canton, USA). Stiffness was determined at 0.5 mm/min, while other tensile characteristics like yield stress, yield strain, tensile strength and elongation-at-break at 5 mm/min cross-head speed and 115 mm gauge length. Impact resistance was determined on notched Charpy specimens according to the ISO 179 standard at 2 mm notch depth. Instrumented impact testing was carried out using a Ceast Resil 5.5 instrument (CEAST S.p.A., Pianezza, Italy) with a 4 J hammer. The structure of the composites was studied by scanning electron microscopy using a Jeol JSM 6380 LA apparatus (JEOL Ltd., Tokyo, Japan). The distribution of the components in the matrix was determined on fracture surfaces created at liquid nitrogen temperature. Samples containing elastomer were etched in n-hexane for 1 min. SEM micrographs were recorded also on surfaces created in the tensile or impact test in order to determine the mechanism of failure. Etching was used when appropriate.

3. Results and discussion

The combination of all the compositional variables resulted in a very large number of composites. As a consequence we refrain from the presentation of all results and focus our attention on materials containing 20 wt% elastomer. However, all the results are presented in figures showing general correlations. In the first two sections we present tensile properties and structure, while impact resistance is analyzed in detail in the next part of the paper. General correlations and practical consequences are discussed in the last section.

3.1. Tensile properties

Model calculations proved that thermodynamics favors the formation of embedded structure. On the other hand, weak interaction and large shear destroys the embedded structure formed, separate the filler and elastomer from each other [17]. Besides being an important characteristic of structural materials, the stiffness of PP composites containing an elastomer and a reinforcement at the same time offers valuable information also about structure. The elastomer decreases stiffness, but otherwise the effect of the components is additive in the case of separate dispersion. On the other hand, embedding results in additional decrease of stiffness, the extent of which can be used for the estimation of the amount of embedded particles [26, 35]. The dependence of the Young's modulus of the composites is presented in Figure 1. The wood flour used in our study reinforces PP considerably and interfacial adhesion does not influence stiffness much. These observations are in complete agreement with our earlier results [36–38]. A slight deviation is observed from the expected tendency at large, 50 and 60 wt% filler content, which indicates a small extent of aggregation. The separate dispersion of the components is expected when both MAPP and EPR are added (▽), and the correlation is practically parallel to that of the PP/wood/MAPP composites (○) proving that the expectation is fulfilled. At large wood content the stiffness of the PP/wood/EPR (▵) composites is somewhat smaller than in the presence of MAPP indicating a small extent of embedding or larger extent of aggregation. However, this latter seems to be less probable. MAEPDM was expected to encapsulate the particles completely [31, 32]. The composition dependence of the stiffness of the compos-

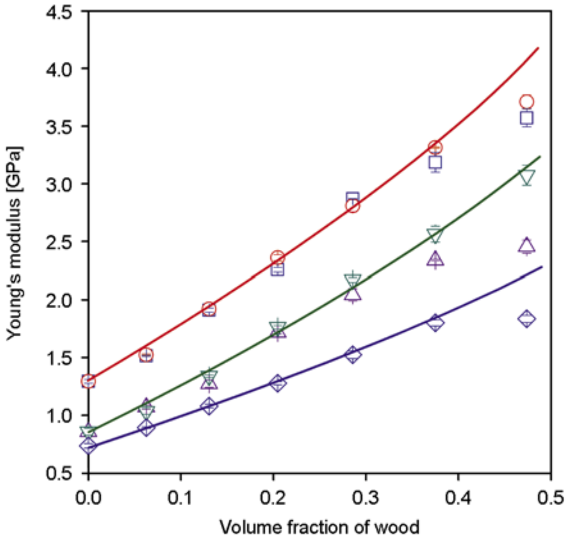

Figure 1. Stiffness of multicomponent PP composites plotted against their wood content. Elastomer content is 20 wt%, that of MAPP is 10 wt%. Symbols: (□) PP/wood, (○) PP/wood/MAPP, (∆) PP/wood/EPR, (∇) PP/wood/EPR/MAPP, (◇) PP/wood/MAEPDM.

ites containing this component does not confirm this expectation (◇). Wood reinforces PP also in this case and the increase in modulus is only slightly smaller in the presence of MAEPDM than with EPR that indicates a somewhat larger, but still small extent of embedding. We may conclude from the analysis of the composition dependence of stiffness that only small extent of embedding occurs in our composites and the separate distribution of the components dominates.

As shown above, stiffness does not depend very much on interfacial adhesion; its effect cannot be deduced from the composition dependence of Young's modulus. Properties measured at larger deformations, like tensile strength, show changes in interactions very sensitively. Tensile strength is plotted against wood content for the same five series of composites in Figure 2. The effect of adhesion and elastomer modification can be clearly seen in the figure. We refrained from drawing lines through all series for better clarity; lines are drawn anyway only to guide the eye and they are not fitted correlations. If we compare PP/wood composites with (○) and without (□) MAPP, the effect of adhesion becomes obvious. Strength increases drastically with increasing wood content in the first case, while it remains constant or slightly decreases in the second. The incorporation of the elastomer decreases strength, but the relative effect of adhesion, i.e. the presence or absence of MAPP, remains the same. Strength is very small in composites containing EPR without MAPP (∆), while a considerable increase in strength is observed at strong adhesion (∇). These results also support our assumption about the separate distribution of the components. The effect of MAEPDM is very similar to that of EPR; composite strength is very small in its presence (◇). We must also comment on the strange composition dependence of strength with the minimum at small and the increase or leveling off at larger wood content. The deformability of the matrix (with or without elas-

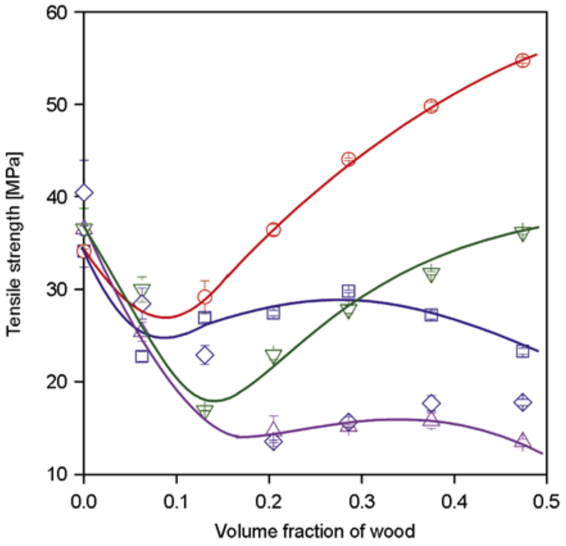

Figure 2. Effect of composition and coupling on the tensile strength of PP/wood composites. Composition and symbols are the same as in Figure 1.

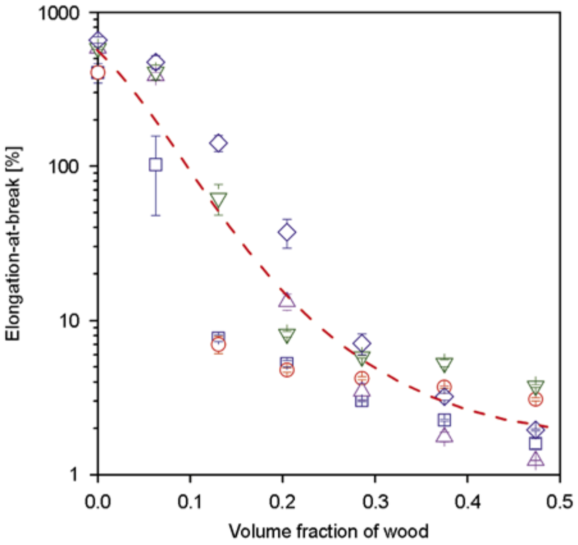

Figure 3. Dependence of the deformability of PP/wood composites on composition and interfacial adhesion. Composition and symbols are the same as in Figure 1.

tomer) and the composites containing various amounts of wood is extremely different; it covers a wide range between 1000 and 2% (Figure 3). Specimen cross-section changes at large elongations and strain hardening increases strength thus complicating the comparison of engineering strength values. Nevertheless, Figure 3 indicates that the presence of the elastomer increases the deformability of the samples, thus we may expect larger impact resistance for these composites.

3.2. Structure

Structure is one of the major factors determining the properties and performance of heterogeneous materials. The structure of the multicomponent multiphase materials in question is rather complicated. The dispersion of the components, aggregation, the orientation of the fibers, and crystalline morphology are the main factors to be considered in the interpretation of composite behavior. One of the most important of these issues is the distribution and possible embedding of the fibers into the elastomer. The composition dependence of stiffness, and that of the other properties studied, indicates that the components are separately dispersed in most composites and only a small extent of encapsulation may occur mostly at large fiber and elastomer content.

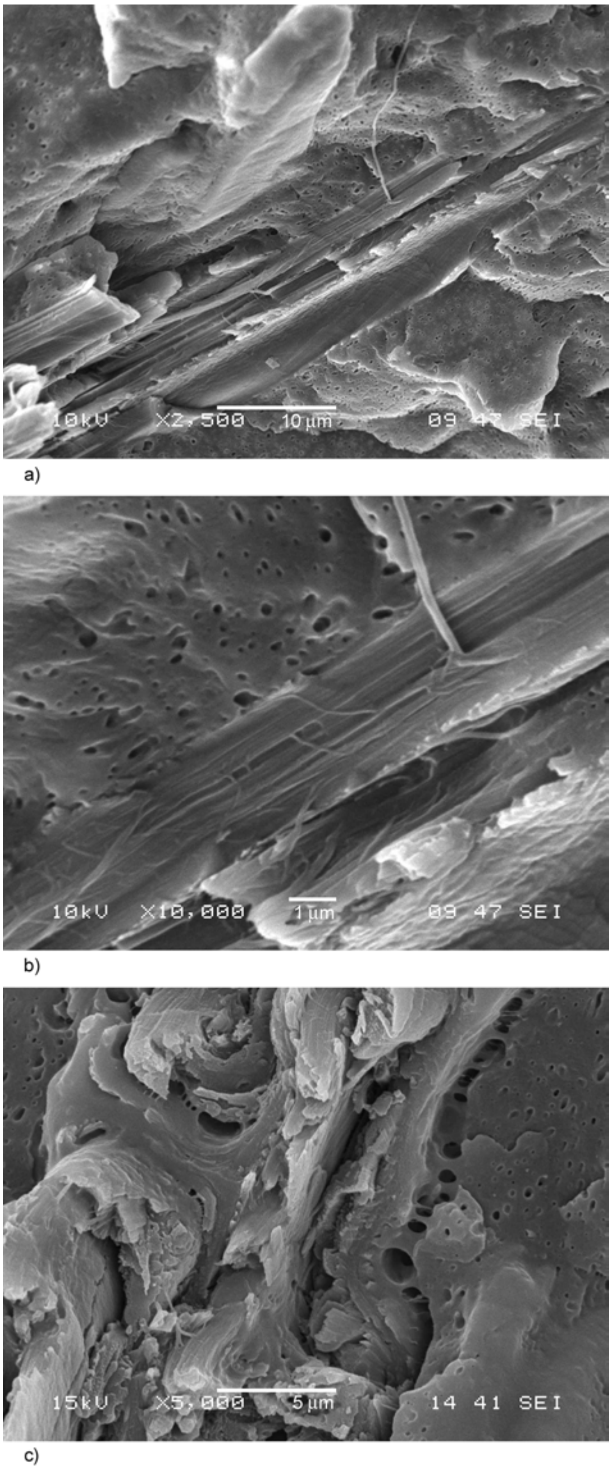

Figure 4. Distribution of the components in PP/wood/elastomer composites in the presence of different functionalized polymers. a) PP/wood (29 vol%)/EPR/MAPP, b) the same as a) at larger magnification, c) PP/wood (29 vol%)/MAEPDM.

In order to check this conclusion drawn from the composition dependence of tensile properties, the structure of the composites was studied also by scanning electron microscopy. The distribution of the components can be determined quite easily on fracture surfaces etched with n-hexane [13]. The elastomer is removed by the solvent during etching leaving holes behind, thus the discrimination of the phases becomes quite easy. Embedding can be detected by the apparently smaller number and total area of holes, and by voids appearing around wood particles. We refrain from the presentation of a large number of micrographs and show only two structures recorded on composites, which are supposed to have the two boundary structures, i.e. separate distribution of the components or complete encapsulation. The first structure should be obtained when both an elastomer and MAPP are added to the PP/wood composite. This structure is shown in Figure 4a. The micrograph verifies our assumption; the elastomer is distributed as submicron sized particles independently of the large wood particles. Unfortunately, the dissimilar dimensions of the dispersed components make the analysis of the structure quite complicated. The same part of the composite is shown in Figure 4b in larger magnification. The micrograph clearly shows that wood is firmly embedded in the PP matrix and elastomer particles are not located on its surface. The other boundary structure, complete embedding, could not be verified in the same way. Figure 4c presents a SEM micrograph taken from the fracture surface of a PP composite containing MAEPDM besides wood. The structure is very similar to that shown in Figure 4a. A large number of small elastomer droplets are visible on the surface. This does not exclude the possibility of fiber encapsulation, but the extent of the latter must be small. A long thin crack runs around the large wood particle, which might be interpreted as dissolved MAEPDM elastomer. However, it is apparently located in the matrix and not on the surface of the wood, and the number of separately dispersed elastomer particles strongly denies the formation of embedded structure. Accordingly, the SEM study confirmed our previous conclusion drawn from the composition dependence of tensile properties that elastomer and wood are distributed mostly separately in the PP matrix.

3.3. Fracture toughness

Impact resistance might be the crucial property of PP/wood composites used in certain application areas as structural materials. Reports in the literature indicate that impact resistance often decreases as an effect of wood reinforcement [38–44] similarly to many particulate filled composites [45–51]. On the other hand, this decrease was compensated by the incorporation of an elastomer into these latter materials. The composition dependence of notched Charpy impact strength is presented for the five series of composites in Figure 5. Without elastomer fracture toughness is relatively small and it appears to go through a slight maximum with increasing wood content. The effect is stronger for PP/wood composites not containing MAPP than in those prepared with it, i.e. at good adhesion. The elastomer increases impact resistance considerably, as expected. However, fracture toughness decreases drastically with increasing wood content almost to the same level of PP/wood composites at the end of the composition range. Contrary to tensile strength, adhesion seems to have only a small effect on impact toughness; obviously other factor or factors determine the resistance of the material against fracture.

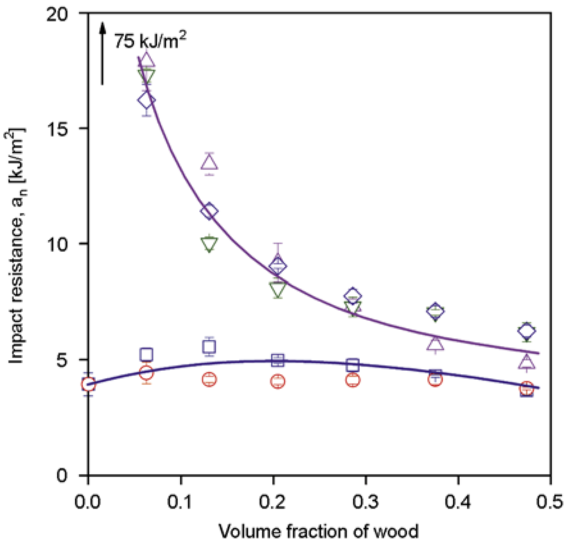

Figure 5. Effect of composition and interfacial adhesion on the impact resistance of multicomponent PP/wood composites. Composition and symbols are the same as in Figure 1.

We hoped that instrumented impact testing supplies additional information about the fracture process itself and about the factors determining fracture resistance. Selected force vs. time traces are presented in Figure 6 to demonstrate the effect of the various additives and factors on the fracture process. Neat PP fails by brittle fracture (Figure 6a). The maximum of the force vs. time traces and the critical stress intensity factor K_{Ic} is related to fracture initiation, while the area under the traces depends also on crack propagation. Fracture is initiated at a relatively small force and catastrophic failure occurs in a few milliseconds with small energy consumption. The presence of a small amount of wood

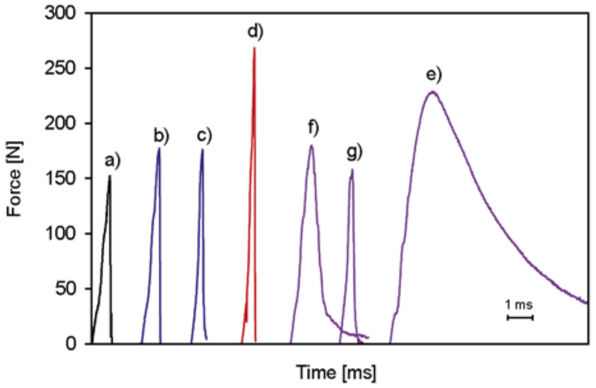

Figure 6. Force vs. time traces recorded by instrumented impact testing on selected multicomponent PP/wood composites. Elastomer content is 20 wt%. a) PP, b) PP/6 vol% wood, c) PP/47 vol% wood, d) PP/47 vol% wood/MAPP, e) PP/EPR, f) PP/13 vol% wood/EPR, g) PP/47 vol% wood/EPR.

increases initiation force and does not change the time to failure much, which leads to increasing fracture energy (Figure 6b). We assume that debonding is the dominating micromechanical deformation process in these composites, which requires surplus energy consumed by the debonding process itself and the subsequent plastic deformation. At larger amount of wood (47 vol%, Figure 6c) stiffness and initiation force increase further, but increased stiffness leads to smaller plastic deformation and reduced energy of fracture (see also the slight maximum in Figure 5). Improved adhesion, i.e. the presence of MAPP, results in a significant increase in initiation force, but increased stiffness reduces the resistance against crack propagation thus overall fracture resistance remains practically constant (Figure 6d). The polymer containing the elastomer behaves completely differently. The elastomer increases the resistance against initiation (see Fmax~240 N), but catastrophic failure does not occur, the propagation of the crack needs constant energy supply (Figure 6e). The addition of wood to the PP/elastomer blend increases stiffness and facilitates crack propagation (Figure 6f) and at large wood content the traces, thus the fracture process, becomes similar, if not the same, as without the elastomer (Figure 6g). Both initiation force and the time to fracture decrease significantly with increasing wood content.

The comparison of the force vs. time traces of Figure 6 indicates that the two components change both crack initiation and propagation. Wood content and adhesion have larger effect on the first, while elastomer on the second. The critical stress intensity factor, K_{Ic}, was calculated by Equation (1) [52]:

$$K_{Ic} = \sigma_F Y a^{1/2} \tag{1}$$

where σ_F is the maximum force recorded during fracture (see Figure 6), a the depth of the notch and Y is a factor depending on the dimensions of the specimen and on loading conditions. The effect of the components on the critical stress intensity factor, K_{Ic}, is presented in Figure 7. We can clearly see the influence of the various processes and factors on the variation of K_{Ic}. The combined effect of reinforcement and increasing stiffness is reflected in the maximum of the correlation obtained for the PP/wood composites (□). The continuously increasing K_{Ic} of the PP/wood/MAPP composite indicates that debonding must play an important role in failure (○).

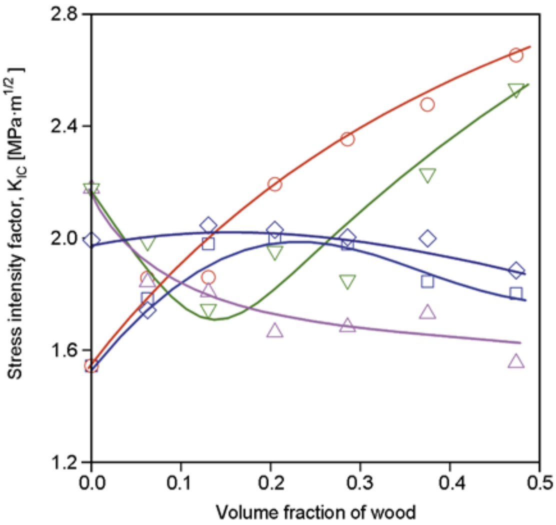

Figure 7. Dependence of the critical stress intensity factor (K_{Ic}) on composition and interfacial adhesion. Composition and symbols are the same as in Figure 1.

Increasing wood content leads to decreasing initiation resistance in the presence of the elastomer (△) and the combined effect of elastomer content, adhesion and wood content is shown by the correlation obtained for PP/wood/EPR/MAPP composites (▽). Although the critical stress intensity factor changes in a wide range, crack propagation seems to dominate fracture resistance and the effect of wood is stronger than that of the elastomer when both components are present. Obviously crack propagation becomes fast and plastic deformation small when the matrix contains large amounts of wood.

Further information can be obtained about the effect of the main factors, if we analyze the composition dependence of fracture resistance with the help of a simple model developed earlier [53], shown in Equation (2):

$$a_n = \frac{a_{n0}}{E/E_0}\frac{1-\varphi}{1+2.5\varphi}\exp(B\varphi) \tag{2}$$

where a_n and a_{n0} are the impact resistance of the composites and the matrix, respectively, E/E_0 is the relative stiffness of the composites, φ is the volume fraction of the dispersed component and B expresses the effect of this latter on impact resistance. According to the model impact resistance is influenced by four factors: matrix property (a_{n0}), the decrease of the deformability of the polymer with increasing amount of reinforcement (E/E_0), changing load-bearing cross-section [$(1-\varphi)/(1+2.5\varphi)$], interfacial interactions and all additional factors [exp($B\varphi$)]. The model proved to be valid for a large number of particulate filled, elastomer modified and multicomponent materials [53]. In these latter the analysis is somewhat difficult since different approaches can be adopted. PP can be regarded as the matrix, the role of the elastomer ignored and only fiber content used as independent variable. This route is obviously wrong because of the influence of the elastomer on both fracture initiation, but especially on crack propagation. The PP/elastomer blend can be also regarded as matrix, while the third possibility is to investigate the combined effect of the additives in the PP matrix. Since the analysis of structure indicated the separate dispersion of the components, we followed the last route.

If we transform Equation (2) to calculate reduced impact strength by dividing composite impact strength with the factors accounting for matrix property, deformability and load-bearing cross-section we arrive to Equation (3):

$$a_{\mathrm{nred}} = a_{\mathrm{n}} \frac{E}{E_0} \frac{1 + 2.5\varphi}{1 - \varphi} = a_{\mathrm{n0}} \exp(B\varphi) \qquad (3)$$

and, if we plot the natural logarithm of this quantity against filler content, we should obtain a straight line the slope of which is parameter B. This latter expresses the effect of the dispersed component on fracture resistance compared to zero effect, i.e. a composite containing the amount of holes corresponding to φ. This means that a filler, reinforcement or other component can have a positive effect on impact resistance even if the actual numbers decrease compared to the matrix value. B is influenced by interfacial interactions, but also by structural effects like particle or matrix orientation, aggregation, etc.

The results obtained for five series are presented in in Figure 8. We can see two sets of lines, one with large slopes corresponding to two-component PP/elastomer blends, and the other to composites containing both elastomer and wood. The combined amount of wood and elastomer is used as compositional variable for these latter composites. We can see that straight lines are obtained in all cases indeed. The slope for the PP/elastomer blends is very large and similar to each other in agreement with the known fact that elastomers increase the impact resistance of PP considerably. The EPR used has a slightly larger effect than the MAEPDM selected. More interesting are the three-component PP/wood/elastomer composites. The smaller slopes express the weaker effect of wood on impact resistance, while the intercepts which differ from the corresponding matrix property express the combined effect of the elastomer and the orientation of the fibers. The slope of the line for the PP/wood/elastomer composites prepared without MAPP (Δ) shows that wood has very little positive effect on impact resistance and that it comes mainly from the energy needed for debonding and from a slight hindrance of crack propagation. Adhesion influences the fracture process strongly and the effect of wood on it (▽), B increases considerably compared to the previous case. This change is caused, in all probability, by the increase of initiation force (see Figure 7). On the other hand, the smaller intersection indicates that adhesion counteracts the positive effect of the elastomer. Parameter B of the composites containing MAEPDM is only slightly larger than that obtained for EPR, which confirms the similarity of structures and the separate distribution of the com-

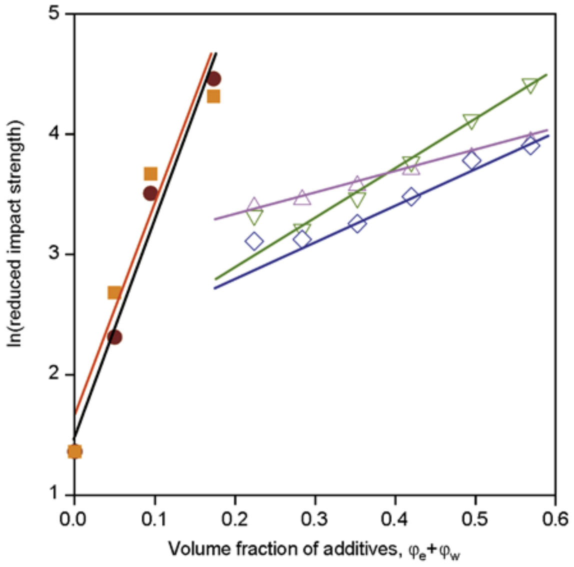

Figure 8. Model calculations carried out for the analysis of the effect of components on the impact resistance of three-component PP/wood/elastomer composites (see Equations (2) and (3) and the calculated parameters in Table 1). Symbols: (●) PP/EPR, (■) PP/MAEPDM blend; the rest of the symbols are the same as in Figure 1.

Table 1. Effect of elastomer impact modifier and wood reinforcement on the impact resistance of three-component PP/wood composites; results of model calculations (see Equations (2) and (3))

Component			Intersection	a_{n0c}[a] [kJ/m^2]	B	R^2[b]
Wood	Elastomer	MAPP				
–	EPR	–	1.46	4.32	18.22	0.9746
–	MAEPDM	–	1.67	5.31	16.85	0.9269
+	EPR[c]	–	3.02	20.44	1.61	0.9951
+	MAEPDM[c]	–	2.27	9.67	2.93	0.9822
+	EPR[c]	+	1.97	7.20	4.30	0.9989

[a] calculated impact resistance of the matrix
[b] determination coefficient, goodness of the linear fit
[c] at 20 wt% elastomer content

ponents. The parameters determined by the model calculations are compiled in Table 1 and support our considerations presented above. We can conclude from all these results that although the presence of wood improves resistance against crack initiation, it facilitates crack propagation very much and thus becomes the dominating factor determining fracture toughness at large wood content.

3.4. Correlations, consequences

The application of multicomponent materials in practice indicates that the approach of the simultaneous use of an elastomer and a reinforcing filler or fiber results in composites which, at least in certain cases, have large stiffness and considerable impact resistance at the same time. The materials prepared in this study failed to meet this requirement espe-

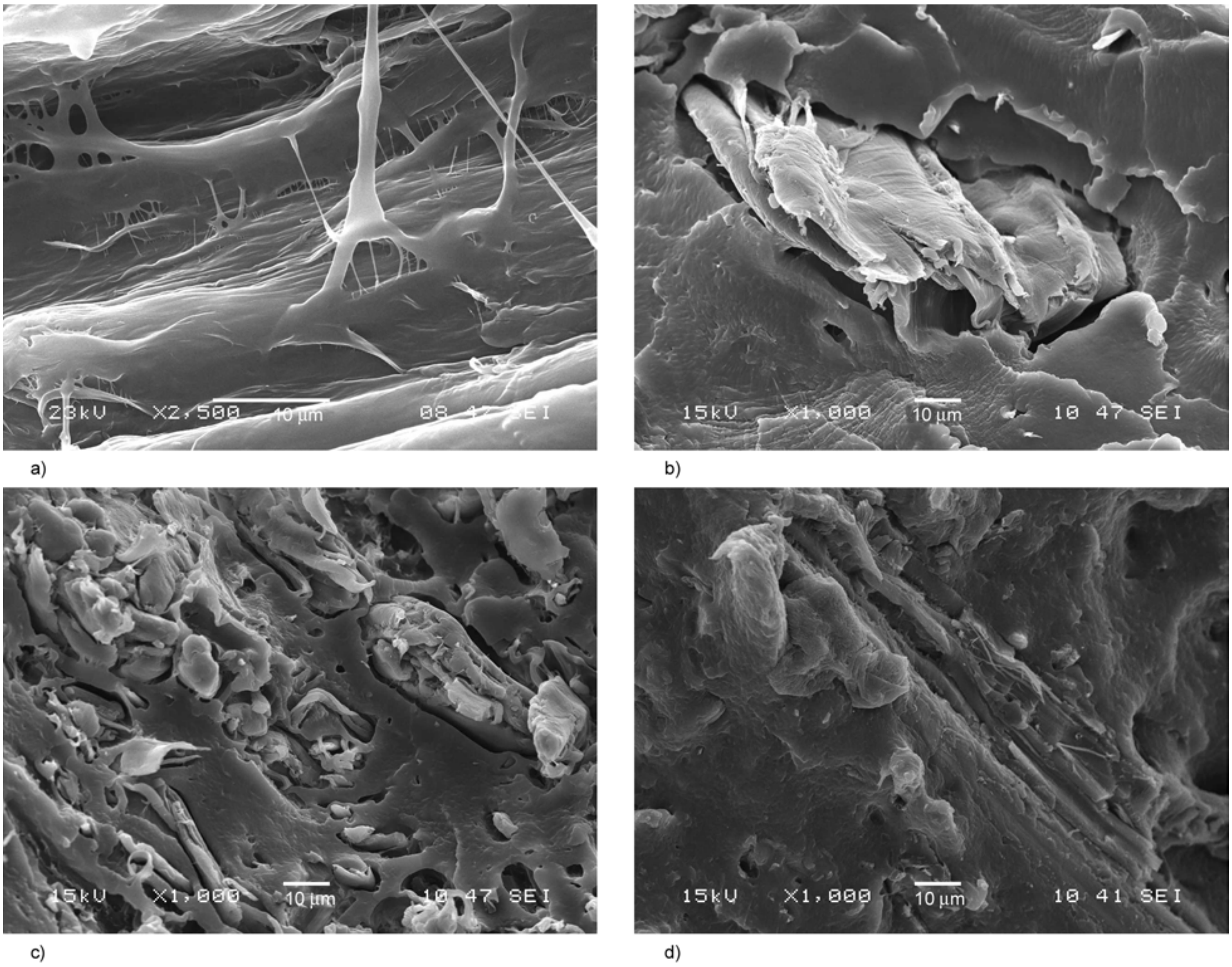

Figure 9. SEM micrographs recorded on the fracture surface of multicomponent PP/wood composites; study of deformation and failure mechanism. The surfaces were created in impact testing. a) PP/20 wt% EPR, b) PP/6 vol% wood/20 wt% elastomer, c) PP/29 vol% wood/20 wt% elastomer, d) PP/29 vol% wood/20 wt% elastomer/MAPP.

cially in the usual range of wood contents. Previous sections showed the main factors influencing fracture toughness. In a further attempt to reveal the reason for the lack of success, we analyzed the fracture surface of various samples by SEM. Only a few examples are shown here to support conclusions drawn in previous sections. Figure 9a shows the fracture surface of a specimen prepared at large elastomer content. We can see that the presence of the elastomer results in considerable plastic deformation as expected. This effect depends on the particle size of the droplets, their dispersion, the properties of the elastomer and interaction. Differences in these factors explain the dissimilar effect of the EPR and the MAEPDM used here. Wood on the other hand, decreases fracture resistance generally, in spite of the fact that debonding consumes energy. The micrograph in Figure 9b proves that very limited plastic deformation occurs in the presence of even a small amount (6 vol%) of wood and the dominating deformation process is debonding. The fact that debonding is dominating in composites not containing MAPP, i.e. at poor adhesion, is shown by Figure 9c in which debonding dominates accompanied by limited pull-out and fiber fracture. At strong adhesion, the main deformation process is the fracture of the fibers (Figure 9d) which is further facilitated by the continuously increasing stiffness with increasing fiber content. Larger stiffness results in smaller deformability in spite of the presence of the elastomer and large fiber content increases the probability of fiber related processes. The domination of these latter and the additive effect of the two components are demonstrated quite convincingly by Figure 10 in which impact resistance is plotted against the relative ratio of the two components, i.e. elastomer (φ_e) and wood (φ_w). A unique and very close correlation is obtained with larger deviations at large elastomer and small wood content. In order to address our main question, i.e. the possibility of simultaneously increasing impact resistance and stiffness, the former property is often plotted against the latter. The correlation of the two quantities is presented for the series of composites discussed throughout this paper in Figure 11. Supporting very much the conclusions of the previous figure, the composites can be divided into two groups, to those containing an elastomeric component and to the two prepared without it. We can see that impact resistance is dominated by fiber related processes, debonding or fiber fracture, and failure is accompanied by very small energy consumption in the latter. This demonstrates again the importance of crack propagation against crack initiation, since resistance against the latter increased quite significantly with fiber content especially in the case of good adhesion (see Figure 7). The other three sets of composites show the usual inverse correlation of

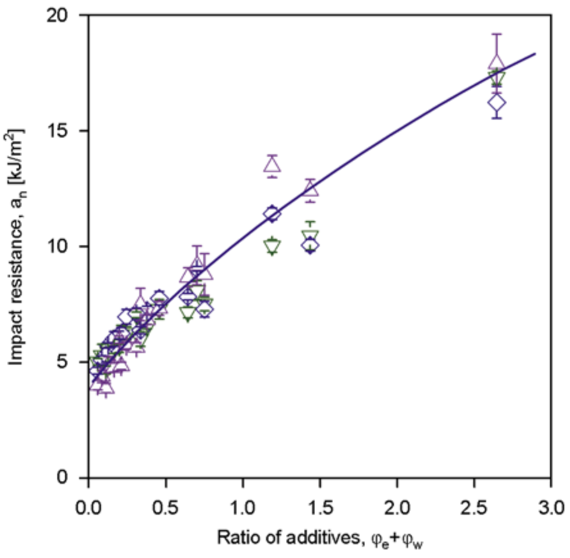

Figure 10. Impact resistance of multicomponent PP/wood composites plotted against the ratio of elastomer and wood volume fractions (φ_e/φ_w). Symbols are the same as in Figure 1. Results obtained at all elastomer contents (5, 10 and 20 wt%) are plotted in the figure.

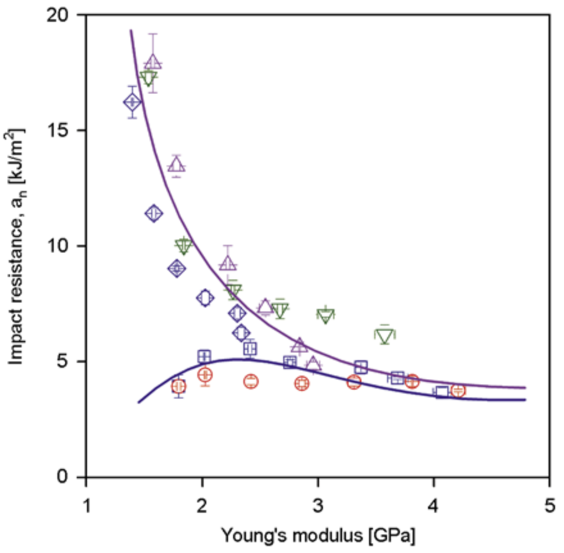

Figure 11. Correlation of impact resistance and stiffness for the five series of composites discussed in the paper. Composition and symbols are the same as in Figure 1.

the two properties characteristic for most structural materials. Very little deviation is observed from the general tendency, but based on the figure we may conclude that separate dispersion is slightly more advantageous than the embedding of the particles through the use of a functionalized elastomer. Figure 11 clearly proves that wood cannot be used in the usual large amounts in composites intended for application in which large stiffness and toughness is required. Failure occurs very easily even at small wood contents because of easy debonding and fracture of the particles caused by their large size. Further study is needed, however, to check the effect of embedding, since all results indicated only limited extent of encapsulation in our composites in spite of the use of the functionalized elastomer.

4. Conclusions

The study of the structure of three-component PP/wood/elastomer composites showed that the components are dispersed independently of each other even when a functionalized elastomer is used for impact modification, at least under the conditions of this study. The stiffness of the composites increases with wood content, but good adhesion, i.e. coupling is needed to improve strength. Impact resistance does not change much as a function of wood content in PP/wood composites, but decreases drastically from the very high level of the PP/elastomer blend to almost the same value as obtained without the impact modifier. Increasing stiffness and fiber related micromechanical deformation processes lead to small fracture toughness at large wood content. These processes depend mainly on PP/wood adhesion; debonding and pull-out take place at poor adhesion, while fiber fracture dominates when adhesion is strong. Composites with sufficiently large impact resistance cannot be prepared in the usual range of wood contents (50–60 wt%). Separate dispersion of the components seems to favor somewhat larger impact resistance, but the effect is slight and needs further checking.

Acknowledgements

The authors are indebted to Zsolt László for his help in the determination of the particle characteristics of wood. The research on heterogeneous polymer systems was financed by the National Scientific Research Fund of Hungary (OTKA Grant No. K 68748 and F 68579) and by the Forbioplast FP7 project of EU (212239); we appreciate the support very much.

References

[1] Bledzki A. K., Sperber V. E., Faruk O.: Natural and wood fibre reinforcement in polymers, Vol. 13. Rapra, Shawbury (2002).

[2] Bledzki A. K., Gassan J.: Composites reinforced with cellulose based fibres. Progress in Polymer Science, **24**, 221–274 (1999).
DOI: 10.1016/S0079-6700(98)00018-5

[3] Bledzki A. K., Faruk O., Huque M.: Physico-mechanical studies of wood fiber reinforced composites. Polymer-Plastics Technology and Engineering, **41**, 435–451 (2002).
DOI: 10.1081/PPT-120004361

[4] Bledzki A. K., Mamun A. A., Volk J.: Physical, chemical and surface properties of wheat husk, rye husk and soft wood and their polypropylene composites. Composites Part A: Applied Science and Manufacturing, **41**, 480–488 (2010).
DOI: 10.1016/j.compositesa.2009.12.004

[5] La Mantia F. P., Morreale M.: Green composites: A brief review. Composites Part A: Applied Science and Manufacturing, **42**, 579–588 (2011).
DOI: 10.1016/j.compositesa.2011.01.017

[6] Stamhuis J. E.: Mechanical properties and morphology of polypropylene composites. Talc-filled, elastomer-modified polypropylene. Polymer Composites, **5**, 202–207 (1984).
DOI: 10.1002/pc.750050308

[7] Stamhuis J. E.: Mechanical properties and morphology of polypropylene composites II. Effect of polar components in talc-filled polypropylene. Polymer Composites, **9**, 72–77 (1988).
DOI: 10.1002/pc.750090110

[8] Stamhuis J. E.: Mechanical properties and morphology of polypropylene composites. III. Short glass fiber reinforced elastomer modified polypropylene. Polymer Composites, **9**, 280–284 (1988).
DOI: 10.1002/pc.750090406

[9] Serafimow B. L.: Rheological properties of multicomponent mixtures based on polypropylene. Plaste und Kautschuk, **29**, 598–600 (1982).

[10] Comitov P. G., Nicolova Z. G., Siméonov I. S., Naidenova K. V., Siarova A. D.: Basic polypropylene compositions possessing an improved shock resistance (in French). European Polymer Journal, **20**, 405–407 (1984).
DOI: 10.1016/0014-3057(84)90068-5

[11] Lee Y. D., Lu C. C.: The mechanical and rheological properties of EPR modified PP composites. Journal of the Chinese Institute of Chemical Engineers, **13**, 1–8 (1982).

[12] Dao K. C., Hatem R. A.: Properties of blends of rubber/talc/polypropylene.in 'Proceedings of the SPE Antec 84, New Orleans, USA' Vol 42, 198–204 (1984).

[13] Kolarík J., Lednický F.: Structure of polypropylene/EPDM elastomer/calcium carbonate composites. in 'Polymer composites' (eds.: Sedlácek B.) Walter de Gruyter, Berlin, 537–544 (1986).

[14] Premphet K., Horanont P.: Influence of stearic acid treatment of filler particles on the structure and properties of ternary-phase polypropylene composites. Journal of Applied Polymer Science, **74**, 3445–3454 (1999).
DOI: 10.1002/(SICI)1097-4628(19991227)74:14<3445::AID-APP19>3.0.CO;2-0

[15] Hornsby P. R., Premphet K.: Influence of phase microstructure on the mechanical properties of ternary phase polypropylene composites. Journal of Applied Polymer Science, **70**, 587–597 (1998).
DOI: 10.1002/(SICI)1097-4628(19981017)70:3<587::AID-APP21>3.0.CO;2-X

[16] Pukánszky B., Kolarík J., Lednický F.: Mechanical properties of three-component polypropylene composites. in 'Polymer composites' (ed.: Sedlácek B.) Walter de Gruyter, Berlin, 553–560 (1986).

[17] Pukánszky B., Tüdős F., Kolarík J., Lednický F.: Ternary composites of polypropylene, elastomer, and filler: Analysis of phase structure formation. Polymer Composites, **11**, 98–104 (1990).
DOI: 10.1002/pc.750110205

[18] Kelnar I.: The effect of PP and EPR grafted with acrylic acid on the properties and phase structure of polypropylene/elastomer/short glass fibre composites. Die Angewandte Makromolekulare Chemie, **189**, 207–218 (1991).
DOI: 10.1002/apmc.1991.051890119

[19] Chiang W-Y., Yang W-D.: Polypropylene composites. I. Studies of the effect of grafting of acrylic acid and silane coupling agent on the performance of polypropylene mica composites. Journal of Applied Polymer Science, **35**, 807–823 (1988).
DOI: 10.1002/app.1988.070350320

[20] Chiang W. Y., Yang W. D., Pukánszky B.: Polypropylene composites. II: Structure-property relationships in two- and three-component polypropylene composites. Polymer Engineering and Science, **32**, 641–648 (1992).
DOI: 10.1002/pen.760321002

[21] Kolarík J., Lednický F., Jancar J., Pukánszky B.: Phase-structure of ternary composites consisting of polypropylene elastomer filler – Effect of functionalized components. Polymer Communications, **31**, 201–204 (1990).

[22] Felix J. M., Gatenholm P.: The nature of adhesion in composites of modified cellulose fibers and polypropylene. Journal of Applied Polymer Science, **42**, 609–620 (1991).
DOI: 10.1002/app.1991.070420307

[23] Kazayawoko M., Balatinecz J. J., Woodhams R. T.: Diffuse reflectance Fourier transform infrared spectra of wood fibers treated with maleated polypropylenes. Journal of Applied Polymer Science, **66**, 1163–1173 (1997).
DOI: 10.1002/(SICI)1097-4628(19971107)66:6<1163::AID-APP16>3.0.CO;2-2

[24] Kazayawoko M., Balatinecz J. J., Matuana L. M.: Surface modification and adhesion mechanisms in woodfiber-polypropylene composites. Journal of Materials Science, **34**, 6189–6199 (1999).
DOI: 10.1023/A:1004790409158

[25] Renner K., Móczó J., Vörös G., Pukánszky B.: Quantitative determination of interfacial adhesion in composites with strong bonding. European Polymer Journal, **46**, 2000–2004 (2010).
DOI: 10.1016/j.eurpolymj.2010.07.008

[26] Molnár Sz., Pukánszky B., Hammer C. O., Maurer F. H. J.: Impact fracture study of multicomponent polypropylene composites. Polymer, **41**, 1529–1539 (2000).
DOI: 10.1016/S0032-3861(99)00305-5

[27] Pukánszky B., Vörös G.: Mechanism of interfacial interactions in particulate filled composites. Composite Interfaces, **1**, 411–427 (1993).

[28] Móczó J., Pukánszky B.: Polymer micro and nanocomposites: Structure, interactions, properties. Journal of Industrial and Engineering Chemistry, **14**, 535–563 (2008).
DOI: 10.1016/j.jiec.2008.06.011

[29] Renner K., Móczó J., Pukánszky B.: Deformation and failure of PP composites reinforced with lignocellulosic fibers: Effect of inherent strength of the particles. Composites Science and Technology, **69**, 1653–1659 (2009).
DOI: 10.1016/j.compscitech.2009.03.015

[30] Renner K., Kenyó C., Móczó J., Pukánszky B.: Micromechanical deformation processes in PP/wood composites: Particle characteristics, adhesion, mechanisms. Composites Part A: Applied Science and Manufacturing, **41**, 1653–1661 (2010).
DOI: 10.1016/j.compositesa.2010.08.001

[31] Clemons C.: Elastomer modified polypropylene–polyethylene blends as matrices for wood flour–plastic composite. Composites Part A: Applied Science and Manufacturing, **41**, 1559–1569 (2010).
DOI: 10.1016/j.compositesa.2010.07.002

[32] Oksman K.: Improved interaction between wood and synthetic polymers in wood/polymer composites. Wood Science and Technology, **30**, 197–205 (1996).
DOI: 10.1007/BF00231633

[33] Oksman K., Clemons C.: Mechanical properties and morphology of impact modified polypropylene–wood flour composites. Journal of Applied Polymer Science, **67**, 1503–1513 (1998).
DOI: 10.1002/(SICI)1097-4628(19980228)67:9<1503::AID-APP1>3.0.CO;2-H

[34] Dányádi L., Janecska T., Szabó Z., Nagy G., Móczó J., Pukánszky B.: Wood flour filled PP composites: Compatibilization and adhesion. Composites Science and Technology, **67**, 2838–2846 (2007).
DOI: 10.1016/j.compscitech.2007.01.024

[35] Pukánszky B.: Heterogeneous polypropylene blends and composites: Structure, properties, interaction. Journal of Polymer Engineering, **12**, 1–32 (1993).
DOI: 10.1515/POLYENG.1993.12.1-2.1

[36] Dányádi L., Renner K., Szabó Z., Nagy G., Móczó J., Pukánszky B.: Wood flour filled PP composites: Adhesion, deformation, failure. Polymers for Advanced Technologies, **17**, 967–974 (2006).

[37] Dányádi L., Renner K., Móczó J., Pukánszky B.: Wood flour filled polypropylene composites: Interfacial adhesion and micromechanical deformations. Polymer Engineering and Science, **47**, 1246–1255 (2007).
DOI: 10.1002/pen.20768

[38] Bledzki A. K., Faruk O.: Wood fiber reinforced polypropylene composites: Compression and injection molding process. Polymer-Plastics Technology and Engineering, **43**, 871–888 (2004).
DOI: 10.1081/PPT-120038068

[39] Kokta B. V., Raj R. G., Daneault C.: Use of wood flour as filler in polypropylene: Studies on mechanical properties. Polymer-Plastics Technology and Engineering, **28**, 247–259 (1989).
DOI: 10.1080/03602558908048598

[40] Woodhams R. T., Thomas G., Rodgers D. K.: Wood fibers as reinforcing fillers for polyolefins. Polymer Engineering and Science, **24**, 1166–1171 (1984).
DOI: 10.1002/pen.760241504

[41] Li T. Q., Li R. K.: A fracture mechanics study of polypropylene–wood flours blends. Polymer-Plastics Technology and Engineering, **40**, 1–21 (2001).
DOI: 10.1081/PPT-100000116

[42] Arbelaiz A., Fernández B., Ramos J. A., Retegi A., Llano-Ponte R., Mondragon I.: Mechanical properties of short flax fibre bundle/polypropylene composites: Influence of matrix/fibre modification, fibre content, water uptake and recycling. Composites Science and Technology, **65**, 1582–1592 (2005).
DOI: 10.1016/j.compscitech.2005.01.008

[43] Mutjé P., Vallejos M. E., Gironès J., Vilaseca F., López A., López J. P., Méndez J. A.: Effect of maleated polypropylene as coupling agent for polypropylene composites reinforced with hemp strands. Journal of Applied Polymer Science, **102**, 833–840 (2006).
DOI: 10.1002/app.24315

[44] Morreale M., Scaffaro R., Maio A., La Mantia F. P.: Effect of adding wood flour to the physical properties of a biodegradable polymer. Composites Part A: Applied Science and Manufacturing, **39**, 503–513 (2008).
DOI: 10.1016/j.compositesa.2007.12.002

[45] Sjögren B. A., Berglund L. A.: Failure mechanisms in polypropylene with glass beads. Polymer Composites, **18**, 1–8 (1997).
DOI: 10.1002/pc.10255

[46] Zebarjad S. M., Tahani M., Sajjadi S. A.: Influence of filler particles on deformation and fracture mechanism of isotactic polypropylene. Journal of Materials Processing Technology, **155**, 1459–1464 (2004).
DOI: 10.1016/j.jmatprotec.2004.04.187

[47] Leong Y. W., Abu Bakar M. B., Ishak Z. A. M., Ariffin A., Pukánszky B.: Comparison of the mechanical properties and interfacial interactions between talc, kaolin, and calcium carbonate filled polypropylene composites. Journal of Applied Polymer Science, **91**, 3315–3326 (2004).
DOI: 10.1002/app.13542

[48] Mareri P., Bastide S., Binda N., Crespy A.: Mechanical behaviour of polypropylene composites containing fine mineral filler: Effect of filler surface treatment. Composites Science and Technology, **58**, 747–752 (1998).
DOI: 10.1016/S0266-3538(97)00156-5

[49] Maiti S. N., Sharma K. K.: Studies on polypropylene composites filled with talc particles Part I Mechanical properties. Journal of Materials Science, **27**, 4605–4613 (1992).
DOI: 10.1007/BF01165994

[50] Velasco J. I., Morhain C., Arencón D., Santana O. O., Maspoch M. L.: Low-rate fracture behaviour of magnesium hydroxide filled polypropylene block copolymer. Polymer Bulletin, **41**, 615–622 (1998).
DOI: 10.1007/s002890050409

[51] Liu J. Y., Reni L., Wei Q., Wu J. L., Liu S., Wang Y. J., Li G. Y.: Fabrication and characterization of polycaprolactone/calcium sulfate whisker composites. Express Polymer Letters, **5**, 742–752 (2011).
DOI: 10.3144/expresspolymlett.2011.72

[52] Williams J. G.: Fracture mechanics of polymers. Ellis Horwood, Chichester (1984).

[53] Pukánszky B., Maurer F. H. J.: Composition dependence of the fracture toughness of heterogeneous polymer systems. Polymer, **36**, 1617–1625 (1995).
DOI: 10.1016/0032-3861(95)99007-H

eXPRESS Polymer Letters Vol.6, No.3 (2012) 237–248
Available online at www.expresspolymlett.com
DOI: 10.3144/expresspolymlett.2012.26

Effect of injection molding parameters on nanofillers dispersion in masterbatch based PP-clay nanocomposites

J. J. Rajesh[1,2], *J. Soulestin*[1,2*], *M. F. Lacrampe*[1,2], *P. Krawczak*[1,2]

[1]Université Lille Nord de France, F-59000 Lille, France
[2]Ecole des Mines de Douai, Department of Polymers and Composites Technology & Mechanical Engineering,
941 Rue Charles Bourseul, BP 10838, F-59508, Douai, France

Received 15 June 2011; accepted in revised form 5 October 2011

Abstract. The effect of injection molding parameters (screw rotational speed, back pressure, injec-tion flow rate and holding pressure) on the nanofiller dispersion of melt-mixed PP/clay nanocomposites was investigated. The nanocomposites containing 4 wt% clay were obtained by dilution of a PP/clay masterbatch into a PP matrix. The evaluation of the dispersion degree was obtained from dynamic rheological measurements. The storage modulus and complex viscosity exhibit significant dependence on the injection molding parameters. PP/clay nanocomposite molded using more severe injection parameters (high shear and long residence time) displays the highest storage modulus and complex viscosity, which illustrates the improved dispersion of clay platelets. This better dispersion leads to better mechanical properties particularly higher Young modulus, tensile strength and unnotched impact strength. A Taguchi analysis was used to identify the influence of individual process parameters. The major individual parameter is the injection flow rate, whose increase improves nanoclay dispersion. The combination of high back pressure and high screw rotational speed is also necessary to optimize the dispersion of clay nanoplatelets.

Keywords: *nanocomposites, masterbatch, polypropylene, montmorillonite, rheology*

1. Introduction

Polymer layered silicate (PLS) nanocomposites are materials in which the reinforcing elements (called nanofillers) are nano-sized at least in one direction leading to very high aspect ratio (length/thickness >100), surface area (100–1000 m^2/g), and surface area to volume ratio [1–2]. The interfacial effects are therefore predominant in that case com-pared with the conventional reinforcements like talc or glass fibers even at very low filler loading level (around 5 wt%). Proper dispersion of nanofillers is a key issue, and as soon as it is achieved, is reflected in superior specific mechanical, thermal, flame retardancy and barrier properties [1–2]. The most commonly developed polymer nanocomposites are based on clay silicate layered nanoplatelets and montmorillonite is the most widely used among them due to its natural abundance and high aspect ratio. The extent of property improvement mainly depends on the dispersion and/or exfoliation of clay nanoplatelets. The exfoliation of clay platelets is an uphill task, particularly in non-polar polymer like polypropylene (PP) because of the unfavorable enthalpic interaction with the highly hy-drophilic clay, which prohibits the diffusion of polymer molecules into the intergallery space. Even if attempts have been made to use pristine (unmodified) clay [3–6], modification of clay with organic agents and addition of compatibilizers such as maleic anhydride (MA) are common solutions used to improve the interaction between PP and clay nanoplatelets. Thereby improved dispersion and thus mechanical properties may be

---

[*]Corresponding author, e-mail: jeremie.soulestin@mines-douai.fr

achieved [7–14] even if full exfoliation cannot be obtained in PP matrices due to the huge polarity difference between the matrix and the clay [15, 16].

The most popular manufacturing process to produce in an economically viable way very complex shape thermoplastic parts for various industrial applications in a single and rapid automatic step (mass production) is injection molding. However, various parameters viz. screw rotation speed, back pressure, injection flow rate, mold temperature, melt temperature, holding pressure, etc., are likely to affect the properties of the injection molded products. The influence of the above-mentioned parameters on mechanical properties of PP was studied extensively [17–19]. However, the literature available on the influence of these parameters on the dispersion of the nanoplatelets in the clay-based nanocomposites is still limited. Authors mainly focused on extrusion process [20–25].

Besides, direct processing (i.e. addition of the nanofillers directly into the host polymer matrix so as to reach the targeted particle weight content) was generally used in the above-mentioned studies. However, masterbatch-based nanocomposites processing (i.e. dilution in a host thermoplastic of a masterbatch highly concentrated in nanofillers) is usually preferred by plastics converters as it avoids direct handling of health hazardous and environmentally unfriendly nanomaterials in industrial production workshops. Nevertheless, the influence of the masterbatch-based processing conditions on the nanofiller dispersion in polymer nanocomposites is sparsely reported in the literature [25–29].

It is therefore worth clarifying the relationship between various injection-molding conditions and the dispersion of clay nanoplatelets in the case of PP nanocomposites obtained by melt-mixing from a PP/clay masterbatch. The influence of injection flow rate, holding pressure, back pressure and screw rotation speed will be investigated in particular in this study, the nanoclay dispersion being assessed using dynamic rheological measurements.

2. Background on assessment of nanofiller dispersion by dynamic rheological measurements

The main issue to solve is to get a representative evaluation of the dispersion degree at the macroscopic scale. Transmission electron microscopy and X-ray diffraction are widely used but provide qualitative assessment only. Alternatively, dynamic rheology may provide a semi-quantitative evaluation of the clay nanoplatelets dispersion degree as the reduction of the filler size down to nanometric scale substantially modifies the viscoelastic properties of filled polymers [30–33].

Actually, it is well admitted that the exfoliated and/or disordered intercalated silicate layers form a network type structure rendering the system highly elastic as revealed by the appearance of a secondary plateau for the dynamic storage modulus (G') in the low frequency regime. This gradual change of the behavior from liquid-like to solid-like is mainly correlated to the extent of dispersion and distribution of the clay platelets that form a three-dimensional percolating network. The tendency of formation of this mesoscopic structure gradually increases with increasing degree of dispersion of the silicate layers in the polymer matrix. The existence of the solid-like rheological behavior of the polymer/clay nanocomposites is attributed to the frictional interactions between the highly anisotropic silicate layers. They become particularly significant when percolation (defined as the formation of a long range connectivity) is obtained leading to a frequency independent behavior at the lower frequencies.

Hoffmann *et al*. [34] confirmed that the higher storage moduli (G') and the lower terminal slope in G' vs frequency (ω) plot illustrated the profound interaction between the silicate platelets and their trend to form a three dimensional superstructure. According to Chow *et al*. [35], the stability of the clay dispersion can be related to the terminal slope, i.e. the higher the slope the less stable the clay dispersion. Moreover, the appearance of a stronger shear thinning effect and higher complex viscosity ($|\eta^*|$) in the lower frequency region indicates a strong intercalation and/or exfoliation process of clay platelets. According to these authors, if the clay layers are well separated from each other (i.e. at exfoliated stage), then shear thinning is more likely to occur than in the case of intercalated composites. Also, the frictional and electrostatic interactions between the many dispersed clay platelets can lead to higher complex viscosity value. Wang *et al*. [36] also discussed this issue. The silicate sheets have positively charged edges and negatively charged faces. This electrostatic interaction between the exfoliated clay platelets leads to strong filler-filler interaction between the clay platelets. The closer vicinity of these clay platelets, probably due to the larger number density and the electrostatic interaction between them, is responsible for higher complex viscosity since the oriented clay platelets under shear field can recover quickly after shear cessation. Galgali *et al*. [8] suggested that the dramatic decrease in creep compliance of compatibilized PP-clay nanocomposites could be due to the frictional interaction between the clay platelets. Therefore larger shear force is required to overcome this frictional interaction between the clay platelets leading to higher complex viscosity value.

Finally, all the authors agree about the correlation between the rheological properties of the nanocomposites at low frequency and the nanofiller dispersion degree. Thus, the comparison of the rheological properties at low frequency of different nanocomposites obtained using various injection molding conditions may allow assessing the influence of each injection molding parameter on the dispersion degree of the clay nanoplatelets.

3. Experimental

The materials studied were 4 wt% organoclay filled PP nanocomposites (NC) prepared by diluting a masterbatch containing 40 wt% clay (Nanoblend 1001, PolyOne, USA) with PP homopolymer with a MFI of 12 g/10 min (B10FB, PolyChim, France) by melt blending technique using a twin screw extruder (BC 45, Clextral, France) with length/diameter ratio $L/D = 28$. The compounding was carried out using a rotation speed of 70 rpm at a flow rate of 9 kg/h. The barrel and die temperature settings ranged from 200 to 220°C. In these conditions the residence time was about 5 min. The neat PP and extruded PP nanocomposites were injection-molded using a 800 kN clamping force injection molding machine (KM80, Krauss Maffei, Germany). The geometry of the injection-molded samples was a 2 mm thick box with a U shape (Figure 1) so as to roughly reproduce the geometry of many industrial parts (boxes, bumper, dash board insert …). The mould cavity was fed by a sprue gate. The set-up injection molding conditions (L at low level and H at high level) are compiled in Table 1. The parameters levels were chosen considering the capacity of the injection-molding machine. Preliminary tests were carried out with the studied materials to determine the possible range of parameters (processing window). For instance, the boundaries of holding pressure are the maximum holding pressure reachable by the injection molding machine and the minimum pressure giving a part of good quality.

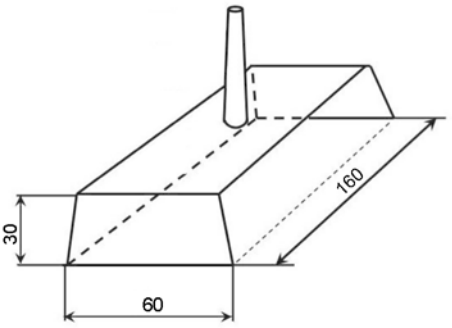

Figure 1. Typical part manufactured by injection moulding

The designation of the various samples obtained that way is the following: PP-H and NC-H, respectively, for the PP and PP nanocomposites which were injection-molded with all set-up parameters at high levels; PP-L and NC-L, respectively, for the PP and PP nanocomposites which were injection-molded with all set-up parameters at low levels. The influence of individual injection molding parameters on the nanoclay dispersion was studied using a L16 (2^{15}) orthogonal array design of experiment (DOE) based on the Taguchi method [37]. The DOE was based on four factors (injection flow rate (Q), holding pressure (HP), back pressure (BP), screw rotation speed (SS)) and two interactions between factors (injection flow rate/holding pressure and screw rotation speed/back pressure). The others processing parameters (holding time, cooling time…) were kept constant. The designation of the nanocomposites samples used for Taguchi analysis is NC-X where X denotes the trial number. Table 2

Table 1. Factors (injection molding parameters) and levels selected in the DOE

	Factors				
	Assigned test level	**Injection flow rate (Q) [cm^3/s]**	**Holding pres-sure (HP) [bar]**	**Back pressure (BP) [bar]**	**Screw speed (SS) [rpm]**
Assigned set-up level	High level (H)	50	350	65	90
	Low level (L)	25	250	35	50

Table 2. L16 (2^{15}) orthogonal array used for the Taguchi DOE

Trial #	Injection flow rate (Q)	Holding pres-sure (HP)	Back pressure (BP)	Screw ro-tation speed (SS)
NC-1 (NC-H)	High	High	High	High
NC-2	Low	High	High	High
NC-3	High	Low	High	High
NC-4	High	High	Low	High
NC-5	High	High	High	Low
NC-6	High	High	Low	Low
NC-7	High	Low	High	Low
NC-8	High	Low	Low	High
NC-9	Low	High	High	Low
NC-10	Low	High	Low	High
NC-11	Low	Low	High	High
NC-12	Low	Low	Low	High
NC-13	Low	Low	High	Low
NC-14	Low	High	Low	Low
NC-15	High	Low	Low	Low
NC-16 (NC-L)	Low	Low	Low	Low

gathers the injection-molding parameters of the nanocomposites samples used for the Taguchi analysis.

The dynamic rheological tests were carried out on samples cut from the edge of the U-shaped injection-molded parts using a rotational rheometer (ARES, Rheometric Scientific, USA) in dynamic frequency sweep mode starting from 0.1 to 100 rad/s at 170°C under air atmosphere. The cone and plate configuration with a cone angle of 0.1 rad was used. All the tests were performed at 10% fixed strain rate in the linear viscoelastic domain. PP nanocomposites have a linear viscoelastic behavior until a strain amplitude of about 30%. Storage modulus (G') and complex viscosity ($|\eta^*|$) were calculated from the tests with data collected at ten points per decade.

Mechanical properties of all compounded materials were determined on standard injection-molded test specimens. Young modulus and elongation at break of the molded dog bone shaped test specimens were measured using a tensile machine (Instron 1185, USA) at a crosshead rate of 20 mm/min at 25°C according to ISO 527 standard. Charpy notched and un-notched impact tests were carried out as per ISO 179-1 standard at 25°C using an impact pendulum (Zwick, Germany). All the reported values were calculated as average over five specimens for each composition.

Morphological analysis was performed on cryofactured surfaces of nanocomposites. A thin layer of carbon was sputter deposited onto the sample. Imaging of the nanocomposite was carried out under high vacuum with an Scanning Electron Microscope (S-4300SE/N, Hitachi, Japan) operating at 5 kV.

Structure of the nanocomposites was evaluated by Transmission Electron Microscopy (TEM) on injection-molded samples. Ultrathin sections were cut at ambient temperature with a microtome (Leica Reichert FCS) and collected on a 300 mesh copper grid before observation by TEM microscope (Leo 922).

4. Results and discussion

4.1. Effect of processing conditions on nanofiller dispersion

Rheological measurements were used to evaluate the dispersion of the clay nanoplatelets for nanocomposites (NC-L and NC-H) obtained by injection molding with different processing parameters. For comparison purpose the neat PP (PP-L and PP-H) was injection molded in the same conditions. Compared to PP-L and NC-L, the nanocomposite NC-H and the PP-H were injection molded with a higher injection flow rate, holding pressure, back pressure and rotational speed so as to increase the dispersion of the clay platelets.

Figures 2 and 3 show the storage modulus (G') and complex viscosity ($|\eta^*|$) as a function of frequency (ω) respectively. The different processing parameters have no significant effect on the rheological

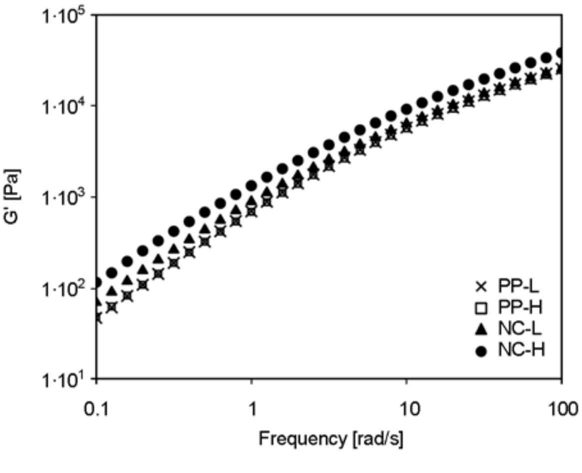

Figure 2. Storage modulus (G') as a function of frequency for PP and PP nanocomposites injection molded with all process parameters set-up at low (PP-L, NC-L) level and high (PP-H, NC-H) level

behavior of the polymer matrix, the G' and $|\eta^*|$ curves being similar for both PP samples (PP-L and PP-H). G' at low frequency is higher upon addition of clay into PP. Moreover, the rheological properties are modified depending on injection molding parameters. The storage modulus G' of the NC-H nanocomposite is higher than the one of the NC-L nanocomposite. As no significant effect of the injection molding parameters is noticed for neat PP, this difference may be ascribed to the improved dispersion of nanoclay when injection flow rate, holding pressure, back pressure and screw rotational speed increase.

Both nanocomposites NC-L and NC-H show no percolation as G' is frequency dependent even at low frequency (Figure 2). This might be explained by the limited dispersion degree due to unfavorable interaction between PP and clay nanoplatelets and by the low clay content (4% wt), whereas the percolation is generally observed at higher clay concentration [8]. Moreover, this tends to evidence that exfoliation does not occur during injection molding leading to intercalated nanocomposites with a dispersion degree insufficient to achieve a percolation effect. However, during the injection molding process of NC-H nanocomposites, due to better plasticating and/or more severe shearing conditions, the size of the clay tactoids is reduced and the aspect ratio increases. This issue will be discussed later on the basis of microstructural characterization.

The evolution of the complex viscosity $|\eta^*|$ of both PP references (PP-L and PP-H) is quite similar at all frequencies (Figure 3). In the case of nanocomposites (NC-L and NC-H), the viscosities are higher deviating from the behavior of neat PP. The viscosity is also clearly higher for NC-H nanocomposite compared to NC-L nanocomposite confirming the better dispersion obtained in this latter case.

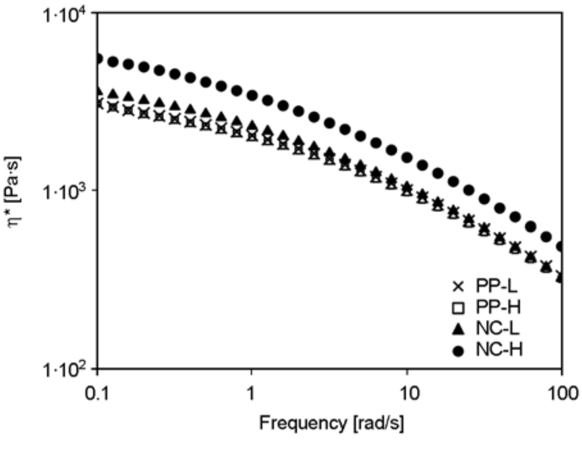

Figure 3. Complex viscosity ($|\eta^*|$) as a function of frequency for PP and PP nanocomposites injection molded with all process parameters set-up at low (PP-L, NC-L) level and high (PP-H, NC-H) level

Table 3. Terminal slope, storage modulus G', shear thinning coefficient n and complex viscosity $|\eta^*|$ at 0.1 rad/s of PP and PP/clay nanocomposites

Material	Terminal slope	Storage modulus, G' [Pa]	Shear thinning coefficient, n	Complex viscosity, $|\eta^*|$ [Pa·s]
PP-L	1.23	48	–0.14	3110
PP-H	1.21	49	–0.15	3104
NC-L	1.00	71	–0.26	3620
NC-H	0.98	107	–0.28	5270

In order to quantitatively assess the clay platelets dispersion in the PP matrix, the storage modulus G', complex viscosity $|\eta^*|$, terminal slope and shear thinning coefficient n values of PP and its nanocomposites at 0.1 rad/s are compiled in Table 3. The terminal slope is defined as the slope of the G' vs frequency (ω) curve in the low frequency region (below 100 rad/s). The shear thinning coefficient is defined as the n exponent of the power law fitting the complex viscosity vs frequency (ω) curves. At low frequency (0.1 rad/s), the storage modulus and complex viscosity are higher for NC-H than for NC-L nanocomposites. This could be explained as follows. NC-L nanocomposite being molded at lower injection flow rate (meaning lower shear induced during injection step), larger particles are present. The number density of clay platelets and tactoids is therefore lower and might be less than the critical level required to significantly modify the rheological behavior in the low frequency region. Micrographs of cryo-fractured surfaces indicate a number of clay platelets lower for NC-L (Figure 4a) than for NC-H (Figure 5a). Lower number of silicate particles coupled with poor affinity with the apolar PP matrix leads to slightly lower storage modulus and complex viscosity values for NC-L compared to NC-H. Lots of voids or micro-cracks on the surface confirm the poor filler-matrix bonding in both NC-L and NC-H. The other important parameters (viz. back pressure and screw rotation speed) that control the plastication step during which the dispersion process generally begins, were also set up at the lower level. These lower level of injection-molding parameters do not promote the delamination of

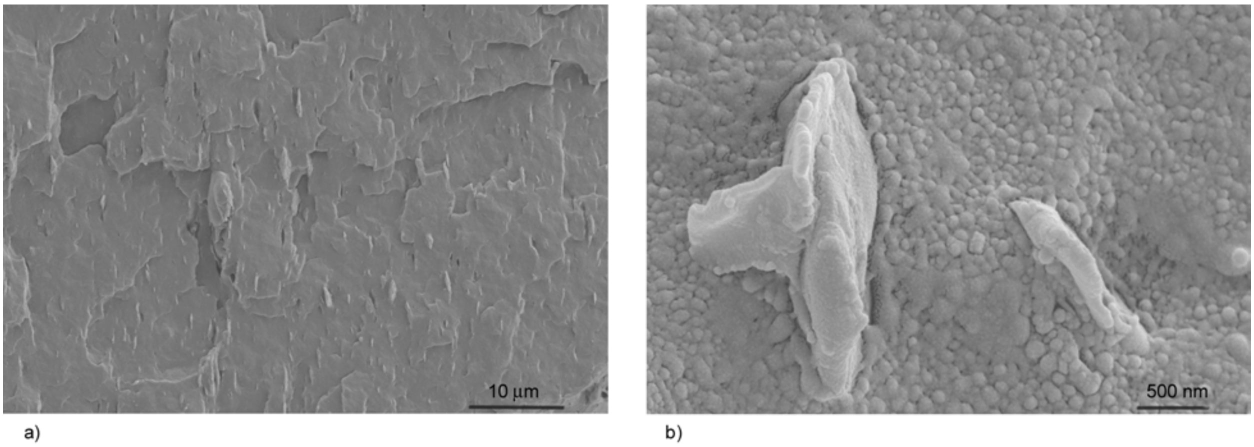

Figure 4. SEM images of cryo-fractured surface of NC-L nanocomposite at low (a) and high (b) magnification

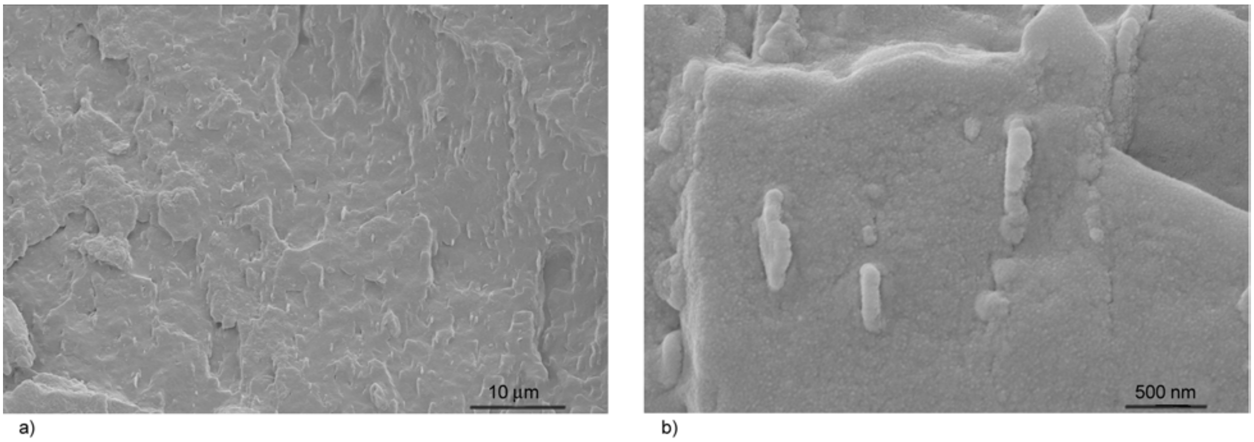

Figure 5. SEM images of cryo-fractured surface of NC-H nanocomposite at low (a) and hig (b) magnification

the clay tactoids and the homogeneous dispersion of clay platelets. Therefore, the dispersion degree of clay platelets may be lower in NC-L than in NC-H. SEM micrographs (Figure 4b and 5b) also confirm this and hence explain lower storage modulus and complex viscosity values measured for NC-L nanocomposites.

TEM observations (Figure 6 and 7) further provide supporting evidence of the above-mentioned trend. Clay platelets are dispersed as tactoids and the structure of both nanocomposites is intercalated. Few isolated platelets are observed. However, in the case of NC-H nanocomposite some exfoliated clay platelets are visible, even if not in a sufficient number to influence significantly the rheological properties of the nanocomposites. The comparison of NC-H and NC-L nanocomposites TEM observations demonstrates clearly that the dispersion degree is higher in the case of NC-H nanocomposite which presents tactoids of smaller size (length below 1 µm and width around 200 nm) and thus higher interface area.

However, as attested by the rheological measurements, none of the nanocomposites presents a sufficient dispersion of the layered silicate as the Newtonian plateau remains. Indeed, the increase of G' and $|\eta^*|$ is usually attributed to the formation of stable three-dimensional network structures, which might consist of exfoliated clay platelets in larger extent because the percolation network could be built in any polymers regardless of its polarity and molecular weight [38]. Moreover, NC-L and NC-H nanocomposites have low shear thinning behavior compared to results reported elsewhere [39]. Even if the dispersion is improved in the case of NC-H compared to NC-L, no or few exfoliation has occured and the extent of intercalation is limited compared to the dispersion commonly obtained in the case of PA6 nanocomposites [40–43].

In order to evaluate the effect of the injection-molding induced dispersion of clay, the mechanical

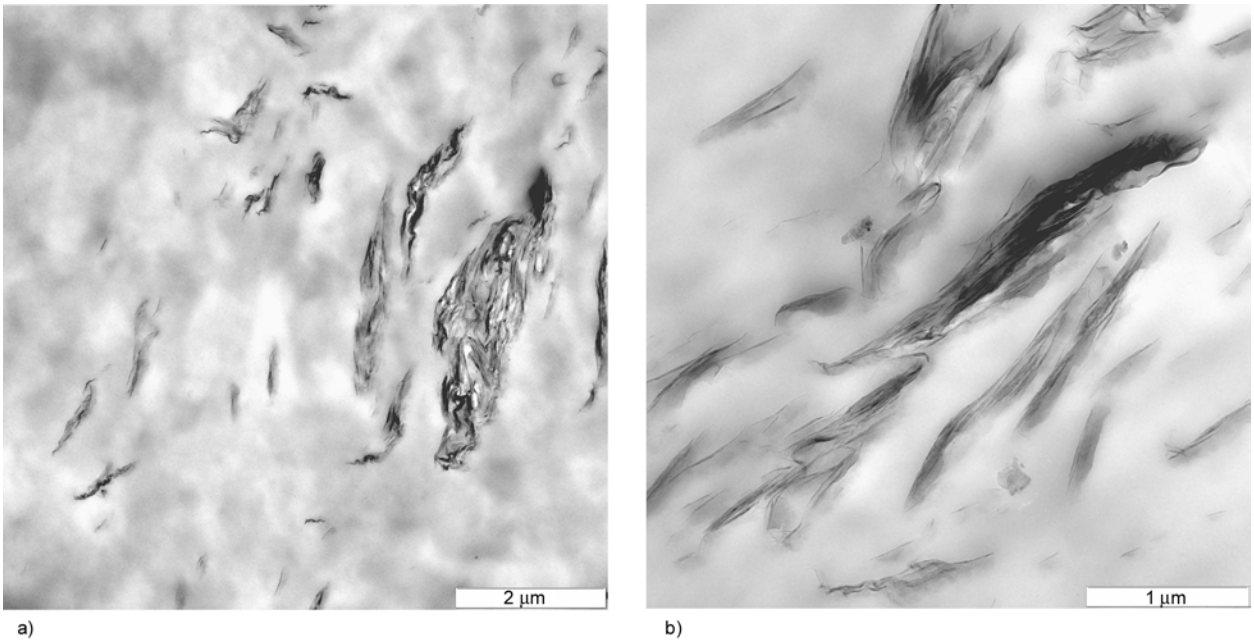

Figure 6. TEM images surface of NC-L nanocomposite at low (a) and high (b) magnification

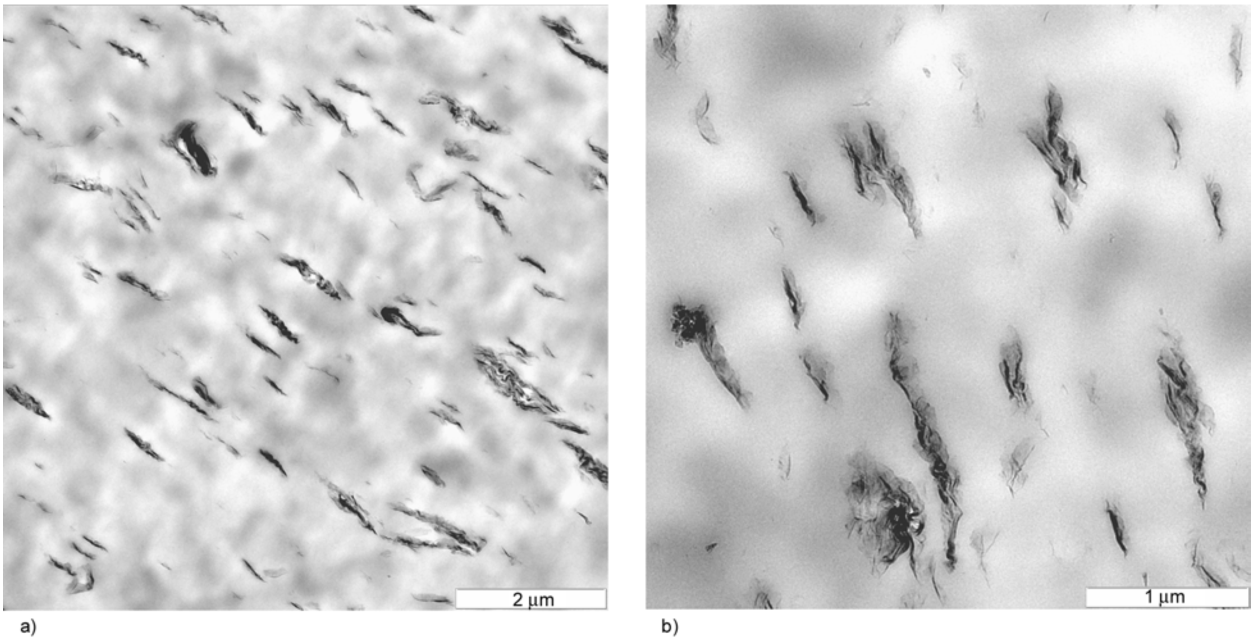

Figure 7. TEM images surface of NC-H nanocomposite at low (a) and high (b) magnification

Table 4. Tensile and Charpy impact properties of PP and PP nanocomposites (average value±standard deviation)

Material	Young modulus [MPa]	Yield stress [MPa]	Tensile el-ongation at break [%]	Stress at break [MPa]	Impact strength – unnotched [kJ/m^2]	Impact strength – notched [kJ/m^2]
PP-L	1280 ± 20	28.9 ± 0.3	616 ± 15	35.2 ± 0.6	117 ± 8	2.4 ± 0.2
PP-H	1254 ± 23	28.8 ± 0.3	613 ± 12	34.7 ± 0.5	120 ± 9	2.3 ± 0.1
NC-L	1617 ± 54	35.3 ± 0.6	100 ± 22	8.7 ± 6.1	52 ± 4	4.3 ± 0.9
NC-H	1687 ± 45	35.6 ± 0.6	103 ± 23	12.9 ± 5.2	64 ± 8	3.9 ± 0.9

properties of the nanocomposites NC-L and NC-H were measured and compared to neat PP. The values of tensile properties (Young modulus, yield stress, stress and elongation at break) and Charpy impact strength are reported in Table 4.

Compared to neat PP (PP-L and PP-H), the increase of the Young modulus for NC-L is about 25% whereas the increase for NC-H is slightly higher (30% compared to PP). The dispersion degree does not significantly modify the yield stress. The influence of the clay dispersion degree is much more visible on the stress at break. The higher dispersion degree in the case of NC-H nanocomposite tends to increase significantly (+50%) the stress at break. Whereas the elongation at break is usually expected to be influenced by the dispersion state, the difference between NC-L and NC-H is here negligible, considering the decrease of ductility when the clay platelets are added into the PP matrix and the standard deviations (experimental data dispersion).

A similar trend is observed for the unnotched impact strength (e.g. toughness decrease upon addition of nanoclay into PP). Conversely, in the case of notched impact strength, the nanocomposites NC-L and NC-H have a higher toughness compared to PP. This is due to the fact that notched impact behavior is controlled to a greater extent by factors affecting the propagation of fracture due to stress concentration at the notch tip. The presence of dispersed clay tactoids may restrict the propagation leading to higher toughness as already observed in the case of PP/carbon nanotube nanocomposites [44, 45]. Concerning the impact strength, the toughness of the better dispersed NC-H nanocomposites tends to be higher (+20%) when measured on unnotched samples.

Finally, it may be concluded that the clay dispersion is influenced by the injection molding conditions. This difference of dispersion degree is sufficient to lead to variations in mechanical properties and thus justifies the optimization of the injection molding parameters so as to take the most of these nanocomposites.

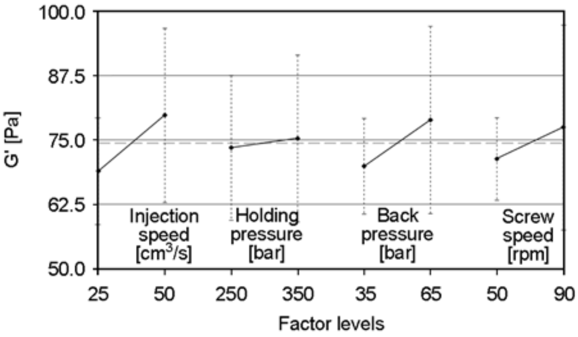

Figure 8. Effect of injection molding parameters on storage modulus G' of PP/Clay nanocomposites – Standard deviations represent data scattering when the considered factor is set-up to its low or high level in the Taguchi DOE

4.2. Optimization of processing parameters

A Taguchi Design Of Experiment (DOE) was used to point out the extent of influence of individual injection molding parameters (also called factors) and their interactions on the nanoclay dispersion [37]. The storage modulus G' was chosen as output parameter for the Taguchi analysis because of its correlation with the nanoplatelets dispersion as already discussed previously. Figures 8 and 9 respectively present the influence of individual injection molding parameters and the influence of the interactions (Taguchi effect graphs). Figure 10 shows the contributions of the individual parameters and interactions to the storage modulus determined from the DOE.

This Taguchi analysis indicates that injection flow rate and back pressure are the two most important individual injection molding parameters that govern the storage modulus of PP/clay nanocomposites and thus, the nanoplatelets dispersion degree. Among them injection flow rate is the dominant factor. Screw rotation speed has little effect. Holding pressure does not show any effect. Therefore the opti-

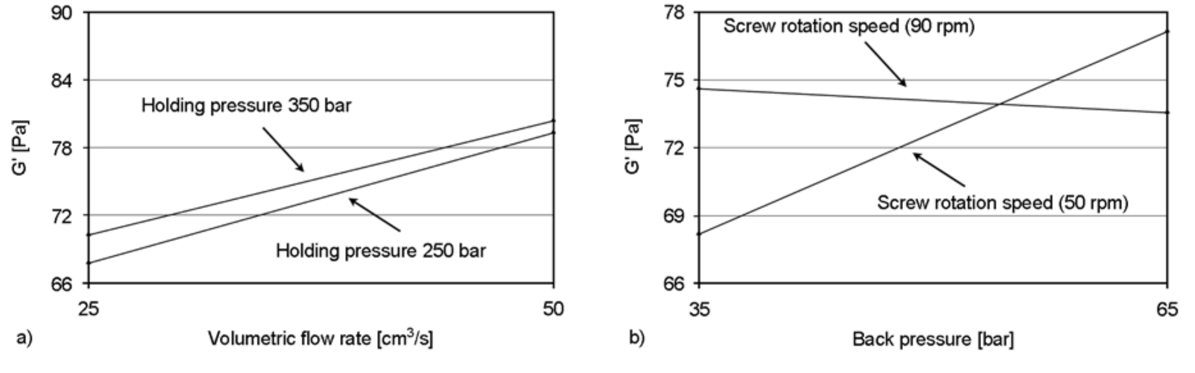

Figure 9. Influence of interactions between injection molding parameters on storage modulus G' of PP/clay nanocomposites

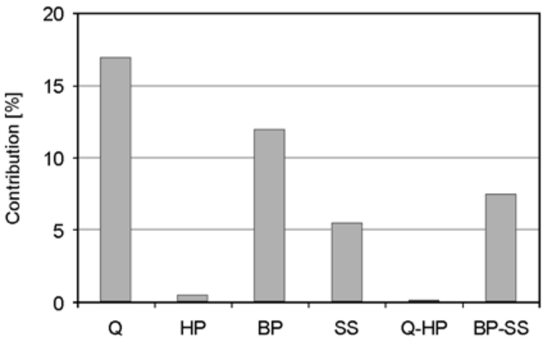

Figure 10. Contribution of individual factors and interactions between factors to the storage modulus (G') variations of PP/clay nanocomposites, from the Taguchi DOE analysis

mum injection molding condition for PP nanocomposites leading to the higher storage modulus should have higher injection flow rate, higher back pressure and higher screw rotation speed. The storage modulus data reported in Table 5 confirm this trend. A reduction in holding pressure (NC-3) does not affect the storage modulus significantly compared to NC-H. However, the reduction in any of other three injection molding parameters lowers the storage modulus compared to NC-H, although the extent of decrement depends on the considered injection molding parameter. This set of optimum conditions leading to the highest storage modulus was logically expected because the dispersion of clay layers begins at the plastication step, which involves parameters such as back pressure and screw rotation speed [46]. Generally a higher plastication effect would result in a better distribution and/or dispersion of clay layers. The increase of shearing force due to the high screw rotation speed causes a better dispersion of clay layers whereas the high back pressure further promotes the dispersion and favors the distribution of the clay domains by providing higher residence time in the barrel. Taguchi analysis shows that the back pressure displays a higher contribution (more than twice) as compared to the screw rotation speed. It tends to prove that, considering the plastication step, the optimization of the nanoclay dispersion requires the increase of the residence time more than the increase of shearing. After the plastication step, the injection step is crucial considering that the injection flow rate is the most important parameter and brings a huge change in the storage modulus values (comparison of NC-H and NC-2). The very high shearing forces induced during the injection step may promote the final delamination of the clay tactoids homogeneously distributed during the plastication step.

Table 5. Experimental data obtained by dynamic rheological measurements – Storage modulus (G') and complex viscosity ($|\eta^*|$) of PP/clay nanocomposites at 0.1 rad/s

Material	G' [Pa]	Complex viscosity, $|\eta^*|$ [Pa·s]
NC-1 (NC-H)	107	5270
NC-2	74	4259
NC-3	104	5096
NC-4	79	4385
NC-5	76	4289
NC-6	59	3170
NC-7	73	3657
NC-8	74	3576
NC-9	59	3241
NC-10	62	3314
NC-11	58	3203
NC-12	63	3379
NC-13	80	4409
NC-14	86	4520
NC-15	66	3359
NC-16 (NC-L)	71	3620

The interactions between injection flow rate and holding pressure (Q-HP), and between the back pressure and screw rotation speed (BP-SS) were also considered (Figure 9) The interaction between the screw rotation speed and the back pressure has a significant influence on the storage modulus when compared with the contribution of the corresponding factors. Also, the interaction between holding pressure and injection flow rate does not show any effect on the storage modulus. The reduction in both the back pressure and screw rotation speed results in a drastic change in G' value of NC-H (comparison of NC-H and NC-14) from 107 to 59 Pa, which is the lowest among all nanocomposites. The combined effect of back pressure and screw rotation speed on dispersion is not surprising as these parameters are intimately correlated to the plastication step and promote a longer residence time [46].

Based on these results it can be concluded that the optimization of injection molding parameters could be done as follows. Increasing the shear using high injection flow rate and increasing the residence time by improving the plastication step (high screw rotation speed and mainly high back pressure) result in higher dispersion degree and thus, better mechanical properties. This is confirmed by rheological measurements as the better dispersion (highest G') is obtained for NC-1 and NC-3, the two samples having these parameters at high level (i.e. Q = 50 cm^3/s, BP = 65 bars and SS = 90 rpm).

5. Conclusions

Injection molding parameters influence the dispersion of clay in PP matrix as attested by the modification of dynamic rheological properties of masterbatch-based melt-mixed PP/clay nanocomposites. Nanocomposites injection-molded at higher back pressure, screw rotational speed, injection flow rate and holding pressure display higher storage modulus and complex viscosity compared to those manufactured with process parameters set-up at lower level. Such improvement achieved with more severe injection molding conditions was attributed to optimized dispersion during injection molding.

The effect of the dispersion degree of the nanoclay on mechanical properties was evaluated. The Young modulus, the Young modulus and the unnotched Charpy impact strength were improved when more severe injection molding parameters were used. Based on a Taguchi analysis, the influence of the individual injection molding parameters and of their interactions on the dispersion was investigated. The injection flow rate and the back pressure are the most influent parameters because of higher shear and longer residence time respectively. The interaction between the back pressure and the screw rotation speed also has a significant influence.

Dilution of highly concentrated PP/clay masterbatches in neat PP is a very promising way to produce polymer nanocomposites injection-molded products in industrially viable conditions. However, the injection molding machine set-up has to take into account the specificity of the polymer nanocomposites. In particular, the dispersion of the nanoplatelets in the final part is a critical issue that requires a careful optimization of the injection molding parameters so as to obtain the expected properties.

References

[1] Utracki L. A.: Clay-containing polymeric nanocomposites. Rapra Technology, Shawbury (2004).

[2] Gupta B., Lacrampe M-F., Krawczak P.: Polyamide-6/clay nanocomposites: A critical review. Polymers and Polymer Composites, **14**, 13–38 (2006).

[3] Aloui M., Soulestin J., Lacrampe M-F., Krawczak P., Rousseaux D., Marchand-Brynaert J., Devaux J., Quiévy N., Sclavons M.: A new elaboration concept of polypropylene/unmodified Montmorillonite nanocomposites by reactive extrusion based on direct injection of polypropylene aqueous suspensions. Polymer Engineering and Science, **49**, 2276–2285 (2009). DOI: 10.1002/pen.21474

[4] Wang Z. M., Nakajima H., Manias E., Chung T. C.: Exfoliated PP/clay nanocomposites using ammonium-terminated PP as the organic modification for montmorillonite. Macromolecules, **36**, 8919–8922 (2003). DOI: 10.1021/ma0352911

[5] Xu L., Nakajima H., Manias E., Krishnamoorti R.: Tailored nanocomposites of polypropylene with layered silicates. Macromolecules, **42**, 3795–3803 (2009). DOI: 10.1021/ma9002853

[6] Liao B., Song M., Liang H., Pang Y.: Polymer-layered silicate nanocomposites. 1. A study of poly(ethylene oxide)/Na$^+$-montmorillonite nanocomposites as polyelectrolytes and polyethylene-block-poly(ethylene glycol) copolymer/Na$^+$-montmorillonite nanocomposites as fillers for reinforcement of polyethylene. Polymer, **42**, 10007–10011 (2001). DOI: 10.1016/S0032-3861(01)00563-8

[7] Reichert P., Hoffmann B., Bock T., Thomann R., Mülhaupt R., Friedrich C.: Morphological stability of poly(propylene) nanocomposites. Macromolecular Rapid Communications, **22**, 519–523 (2001). DOI: 10.1002/1521-3927(20010401)22:7<519::AID-MARC519>3.0.CO;2-W

[8] Gagali G., Ramesh C., Lele A.: A rheological study on the kinetics of hybrid formation in polypropylene nanocomposites. Macromolecules, **34**, 852–858 (2001). DOI: 10.1021/ma000565f

[9] Solomon M. J., Almusallam Q. S., Seefeldt K. F., Somwangthanaroj A., Varadan P.: Rheology of polypropylene/clay hybrid materials. Macromolecules, **34**, 1864–1872 (2001). DOI: 10.1021/ma001122e

[10] García-López D., Picazo O., Merino J. C., Pastor J. M.: Polypropylene–clay nanocomposites: Effect of compatibilizing agents on clay dispersion. European Polymer Journal, **39**, 945–950 (2003). DOI: 10.1016/S0014-3057(02)00333-6

[11] Jian L., Zhou C., Gang W., Wei Y., Ying T., Qing L.: Preparation and linear rheological behavior of polypropylene/MMT nanocomposites. Polymer Composites, **24**, 323–331 (2003). DOI: 10.1002/pc.10032

[12] Li J., Zhou C., Wang G., Zhao D.: Study on rheological behavior of polypropylene/clay nanocomposites. Journal of Applied Polymer Science, **89**, 3609–3617 (2003). DOI: 10.1002/app.12643

[13] Gu S-Y., Ren J., Wang Q-F.: Rheology of poly(propylene)/clay nanocomposites. Journal of Applied Polymer Science, **91**, 2427–2434 (2004).
DOI: 10.1002/app.13403

[14] Treece M. A., Oberhauser J. P.: Soft glassy dynamics in polypropylene–clay nanocomposites. Macromolecules, **40**, 571–582 (2007).
DOI: 10.1021/ma0612374

[15] Manias E., Touny A., Wu L., Strawhecker K., Lu B., Chung T. C.: Polypropylene/montmorillonite nanocomposites. Review of the synthetic routes and materials properties. Chemistry of Materials, **13**, 3516–3523 (2001).
DOI: 10.1021/cm0110627

[16] Rousseaux D. D. J., Sallem-Idrissi N., Baudouin A., Devaux J., Godard P., Marchand-Brynaert J., Sclavons M.: Water-assisted extrusion of polypropylene/clay nanocomposites: A comprehensive study. Polymer, **52**, 443–451 (2011).
DOI: 10.1016/j.polymer.2010.11.027

[17] Trotignon J-P., Verdu J.: Skin-core structure–fatigue behavior relationships for injection-molded parts of polypropylene. I. Influence of molecular weight and injection conditions on the morphology. Journal of Applied Polymer Science, **34**, 1–18 (1987).
DOI: 10.1002/app.1987.070340101

[18] Čermák R., Obadal M., Ponížil P., Polášková M., Stoklasa K., Lengálová A.: Injection-moulded α- and β-polypropylenes: I. Structure vs. processing parameters. European Polymer Journal, **41**, 1838–1845 (2005).
DOI: 10.1016/j.eurpolymj.2005.02.020

[19] LaFranche E., Brassart G., Krawczak P.: Processing-induced morphology: Its relationship with tensile-impact behaviour in injection-moulded polypropylene. Polymers and Polymer Composites, **14**, 563–576 (2006).

[20] Médéric P., Razafinimaro T., Aubry T., Moan M., Klopffer M-H.: Rheological and structural investigation of layered silicate nanocomposites based on polyamide or polyethylene: Influence of processing conditions and volume fraction effects. Macromolecular Symposia, **221**, 75–84 (2005).
DOI: 10.1002/masy.200550308

[21] Peltola P., Välipakka E., Vuorinen J., Syrjälä S., Hanhi K.: Effect of rotational speed of twin screw extruder on the microstructure and rheological and mechanical properties of nanoclay-reinforced polypropylene nanocomposites. Polymer Engineering and Science, **46**, 995–1000 (2006).
DOI: 10.1002/pen.20586

[22] Lertwimolnun W., Vergnes B.: Influence of compatibilizer and processing conditions on the dispersion of nanoclay in a polypropylene matrix. Polymer, **46**, 3462–3471 (2005).
DOI: 10.1016/j.polymer.2005.02.018

[23] Modesti M., Lorenzetti A., Bon D., Besco S.: Effect of processing conditions on morphology and mechanical properties of compatibilized polypropylene nanocomposites. Polymer, **46**, 10237–10245 (2005).
DOI: 10.1016/j.polymer.2005.08.035

[24] Kracalik M., Laske S., Gschweitl M., Friesenbichler W., Langecker G. R.: Advanced compounding: Extrusion of polypropylene nanocomposites using the melt pump. Journal of Applied Polymer Science, **113**, 1422–1428 (2009).
DOI: 10.1002/app.29888

[25] Treece M. A., Zhang W., Moffitt R. D., Oberhauser J. P.: Twin-screw extrusion of polypropylene-clay nanocomposites: Influence of masterbatch processing, screw rotation mode, and sequence. Polymer Engineering and Science, **47**, 898–911 (2007).
DOI: 10.1002/pen.20774

[26] Li Y-C., Chen G-H.: HDPE/expanded graphite nanocomposites prepared via masterbatch process. Polymer Engineering and Science, **47**, 882–888 (2007).
DOI: 10.1002/pen.20772

[27] Pötschke P., Bhattacharyya A. R., Alig I., Dudkin S. M., Leonhardt A., Täschner C., Ritschel M., Roth S., Hornbostel B., Cech J.: Dispersion of carbon nanotubes into thermoplastic polymers using melt mixing. in 'Electronic properties of synthetic nanostructures: XVIII international winterschool/euroconference on electronic properties of novel materials' (eds.: Kuzmany H., Fink J., Mehring M., Roth S.) American Institute of Physic, Washington 478–482 (2004).

[28] Shah R. K., Paul D. R.: Nylon 6 nanocomposites prepared by a melt mixing masterbatch process. Polymer, **45**, 2991–3000 (2004).
DOI: 10.1016/j.polymer.2004.02.058

[29] Yilmazer U., Ozden G.: Polystyrene–organoclay nanocomposites prepared by melt intercalation, in situ, and masterbatch methods. Polymer Composites, **27**, 249–255 (2006).
DOI: 10.1002/pc.20191

[30] Dorigato A., Pegoretti A., Penati A.: Linear low-density polyethylene/silica micro- and nanocomposites: Dynamic rheological measurements and modelling. Express Polymer Letters, **4**, 115–129 (2010).
DOI: 10.3144/expresspolymlett.2010.16

[31] Sarvestani A. S.: Modeling the solid-like behavior of entangled polymer nanocomposites at low frequency regimes. European Polymer Journal, **44**, 263–269 (2008).
DOI: 10.1016/j.eurpolymj.2007.11.023

[32] Le Meins J-F., Moldenaers P., Mewis J.: Suspensions in polymer melts. 1. Effect of particle size on the shear flow behavior. Industrial and Engineering Chemistry Research, **41**, 6297–6304 (2002).
DOI: 10.1021/ie020117r

[33] Osman M. A., Atallah A.: Interparticle and particle–matrix interactions in polyethylene reinforcement and viscoelasticity. Polymer, **46**, 9476–9488 (2005).
DOI: 10.1016/j.polymer.2005.07.030

[34] Hoffmann B., Kressler J., Stöpplemann G., Friedrich C., Kim G-M.: Rheology of nanocomposites based on layered silicates and polyamide-12. Colloid and Polymer Science, **278**, 629–636 (2000).
DOI: 10.1007/s003960000294

[35] Chow W. S., Mohd Ishak Z. A., Karger-Kocsis J.: Morphological and rheological properties of polyamide 6/poly(propylene)/organoclay nanocomposites. Macromolecular Materials and Engineering, **290**, 122–127 (2005).
DOI: 10.1002/mame.200400269

[36] Wang K., Zhao P., Yang H., Liang S., Zhang Q., Du R., Fu Q., Yu Z., Chen E.: Unique clay orientation in the injection-molded bar of isotactic polypropylene/clay nanocomposite. Polymer, **47**, 7103–7110 (2006).
DOI: 10.1016/j.polymer.2006.08.022

[37] Taguchi G., Konishi S., Wu Y.: Quality engineering series, Vol. 1, Taguchi methods, research and development. ASI, Dearborn (1992).

[38] Wang K., Liang S., Zhao P., Qu C., Tan H., Du R., Zhang Q., Fu Q.: Correlation of rheology–orientation–tensile property in isotactic polypropylene/organoclay nanocomposites. Acta Materialia, **55**, 3143–3154 (2007).
DOI: 10.1016/j.actamat.2007.01.020

[39] Ray S. S.: Rheology of polymer/layered silicate nanocomposites. Journal of Industrial and Engineering Chemistry, **12**, 811–842 (2006).

[40] Zhao J., Morgan A. B., Harris J. D.: Rheological characterization of polystyrene–clay nanocomposites to compare the degree of exfoliation and dispersion. Polymer, **46**, 8641–8660 (2005).
DOI: 10.1016/j.polymer.2005.04.038

[41] Samyn F., Bourbigot S., Jama C., Bellayer S., Nazare S., Hull R., Castrovinci A., Fina A., Camino G.: Crossed characterisation of polymer-layered silicate (PLS) nanocomposite morphology: TEM, X-ray diffraction, rheology and solid-state nuclear magnetic resonance measurements. European Polymer Journal, **44**, 1642–1653 (2008).
DOI: 10.1016/j.eurpolymj.2008.03.021

[42] Soulestin J., Rashmi B. J., Bourbigot S., Lacrampe M. F., Krawczak P.: Mechanical and optical properties of polyamide 6/clay nanocomposite cast-films: Influence of the exfoliation degree. Macromolecular Materials and Engineering, in press (2011).
DOI: 10.1002/mame.201100202

[43] Touchaleaume F., Soulestin J., Sclavons M., Devaux J., Lacrampe M. F., Krawczak P.: One-step water-assisted melt-compounding of polyamide 6/pristine clay nanocomposites: An efficient way to prevent matrix degradation. Polymer Degradation and Stability, **96**, 1890–1900 (2011).
DOI: 10.1016/j.polymdegradstab.2011.07.005

[44] Prashantha K., Soulestin J., Lacrampe M. F., Claes M., Dupin G., Krawczak P.: Multi-walled carbon nanotube filled polypropylene nanocomposites based on masterbatch route: Improvement of dispersion and mechanical properties through PP-g-MA addition. Express Polymer Letters, **2**, 735–745 (2008).
DOI: 10.3144/expresspolymlett.2008.87

[45] Prashantha K., Soulestin J., Lacrampe M. F., Krawczak P., Dupin G., Claes M.: Masterbatch-based multi-walled carbon nanotube filled polypropylene nanocomposites: Assessment of rheological and mechanical properties. Composites Science and Technology, **69**, 1756–1763 (2009).
DOI: 10.1016/j.compscitech.2008.10.005

[46] Rosato D. V., Rosato M. G.: Injection molding handbook. Kluwer, Norwell (2000).

eXPRESS Polymer Letters Vol.6, No.3 (2012) 249–256
Available online at www.expresspolymlett.com
DOI: 10.3144/expresspolymlett.2012.27

Evaluation of structural change and local strain distribution in polymers comparatively imaged by FFSA and OCT techniques

E. Leiss-Holzinger[1*], *U. D. Cakmak*[2], *B. Heise*[3,4], *J.-L. Bouchot*[3], *E. P. Klement*[3], *M. Leitner*[1], *D. Stifter*[4], *Z. Major*[2]

[1]RECENDT, Research Center for Non Destructive Testing GmbH, Science Park 2/2.OG, Altenberger Straße 69, 4040 Linz, Austria
[2]Institute of Polymer Product Engineering, Johannes Kepler University Linz, Altenbergerstrasse 69, 4040 Linz, Austria
[3]Christian Doppler Laboratory for Microscopic and Spectroscopic Material Characterization, Department of Knowledge-Based Mathematical Systems (FLLL), Johannes Kepler University Linz, Altenbergerstr. 69, 4040 Linz, Austria
[4]Christian Doppler Laboratory for Microscopic and Spectroscopic Material Characterization, Center for Surface- and Nanoanalytics (ZONA), Johannes Kepler University Linz, Altenbergerstr. 69, 4040 Linz, Austria

Received 23 June 2011; accepted in revised form 5 October 2011

Abstract. Mechanical material testing combined with optical coherence tomography (OCT) allows for the first time the immediate detection of inner structural changes along with a qualitative observation of the local strain distribution in surface near bulk regions of semitransparent and translucent specimens. In addition to a 3D full field strain analysis (FFSA) system based on digital image correlation (DIC), a customized spectral domain OCT system operating at 1550 nm was applied for investigation. Exemplified by tensile testing of elastomer particle filled polypropylene specimens, local dissimilarity evaluation of the OCT images was performed. The results show the high potential of OCT to provide complementary information to DIC-based FFSA, like to identify processes influencing the remaining life of advanced commodity plastics such as the start and progress of yielding, identification of the yielding point, localization of the necking front and the development of small scale voids as in the case of matrix crazing.

Keywords: *material testing, polymer blends and alloys, damage mechanism, full field strain analysis, optical coherence tomography*

1. Introduction

The high demands on tailor made materials such as light weight but stiff construction, in addition to aesthetic and haptic properties, are increasingly met by advanced commodity plastics. Various fillers and fibers with different particle size, shape, and surface properties are applied to modify the material's stiffness, strength, and tribological behavior. These are the visible improvements on the macroscopic scale. However, on a mesoscopic scale the material is multiphase and at the corresponding interfaces the material is prone to various defects, as e.g. rupture of elastomer particles resulting in voids [1]. One challenge is to characterize these defects in engineering structures before and during the service in order to visualize the actual mechanical state (stress and strain), with an emphasis on the remaining product life assessment. In the literature and in practice many non-destructive testing and evaluation (NDTE) methods have been introduced with discussions regarding their limitations [2–6].

---

[*]Corresponding author, e-mail: elisabeth.leiss@recendt.at

Optical coherence tomography (OCT) is a non-destructive and contactless method for high-resolution imaging of internal structures within turbid media. Invented in the early 90's [7], OCT was originally developed for biomedical applications and is nowadays a well established tool for *in vivo* diagnostics of eye diseases [8]. In the materials sector, the applications range from imaging of subsurface cracks in ceramics or Teflon, to the investigation of thin multi-layer foils, coatings and injection moulded plastic parts [9]. In the subsurface regions of such semi-transparent and translucent media OCT detects microscopic size defects and structures with a spatial resolution in the micrometer range [10]. The penetration depth strongly depends on the attenuation properties of the material (scattering and absorption) in the used wavelength range. OCT uses light in the near-infrared (800–1500 nm) and therefore composites containing conducting fibers (e.g. carbon) or metal components are not suitable for OCT imaging due to their opacity. However, a customized OCT system is easy to operate, usually requires no sample preparation and the measurement head can be designed specially towards the needs of the application, e.g. as a hand-held detector. In addition, this method allows the immediate observation of a specimen and its inner structure during material testing. OCT has lately also shown high potential as a high resolution imaging method for *in-situ* monitoring during arbitrary mechanical loading of heterogeneous polymer structures [11]. Based on the principle of standard photoelasticity [12], the so called polarization sensitive (PS-) OCT [13] technique can yield depth resolved polarization patterns. This method was proven to be applicable for the non destructive quantification of internal stress in polymer materials [14, 15], including dynamic measurements during tensile tests [11], but shows two major restrictions: First, samples becoming strongly depolarizing under stress will not show any polarization patterns, as it is the case for the specimens presented in this work. Secondly, a PS-OCT setup detects only stress induced birefringence perpendicular to the incident light beam, which leads to a systematic error. A more promising approach is speckle tracking. Since its invention in the 80's [16], digital image correlation (DIC) in combination with speckle tracking is used to determine the local strain distribution on surfaces during mechanical loading. In order to receive adequate speckles, it is common practice to apply a stochastic color spray pattern on the specimen surface. In contrast, the depth resolved, OCT based method relies on intrinsic speckles inside the real specimen that do not only represent material related information but also noise [17]. In addition, rigid-sample displacement occurring during the testing procedure and several imaging artifacts, like strong reflections at defects, misalignments, or decreasing signal-to-noise ratio over depth, require extended image enhancement. Thus, existing DIC software does not directly work on the recorded OCT images.

For this work tensile tests were performed on elastomer particle filled PP polymer test bars. The local strain on the surface was monitored with a stereoscopic full field strain analysis (FFSA) system based on DIC. As complementary method depth resolved measurements with an OCT system followed by advanced data processing were performed and the promising results are presented in the following.

2. Experimental setup and method

Based on white light interferometry, OCT employs light in the near infrared spectral region [8, 18]. The light coming from the optical source is split into a sample and a reference interferometer arm, with the latter one being terminated by a mirror. The light back reflected from the reference mirror and the different sample structures is then recombined. The so called spectral domain (SD-) OCT uses a broadband light source with the spectrum being detected as a whole by the grating spectrometer, as depicted in Figure 1a). The lateral (Δx) and depth resolution (Δz) are independent and limited by the optics and the square of the center wavelength λ_c over the source bandwidth ($\Delta\lambda$) (with $\Delta z \propto (\lambda_c)^2/(\Delta\lambda)$), respectively [19]. Thus, best resolution is achieved for high bandwidth sources centered at shorter wavelengths. On the other hand, the penetration depth is limited by the attenuation properties in the wavelength range used. It was shown that for most polymers measurements applying 1550 nm center wavelength resulted in a more than doubled penetration depth when compared to measurements performed at 800 nm [9]. Thus, the SD-OCT system was equipped with a superluminescence diode centered around 1550 nm and a spectral width of 55 nm (Exalos,

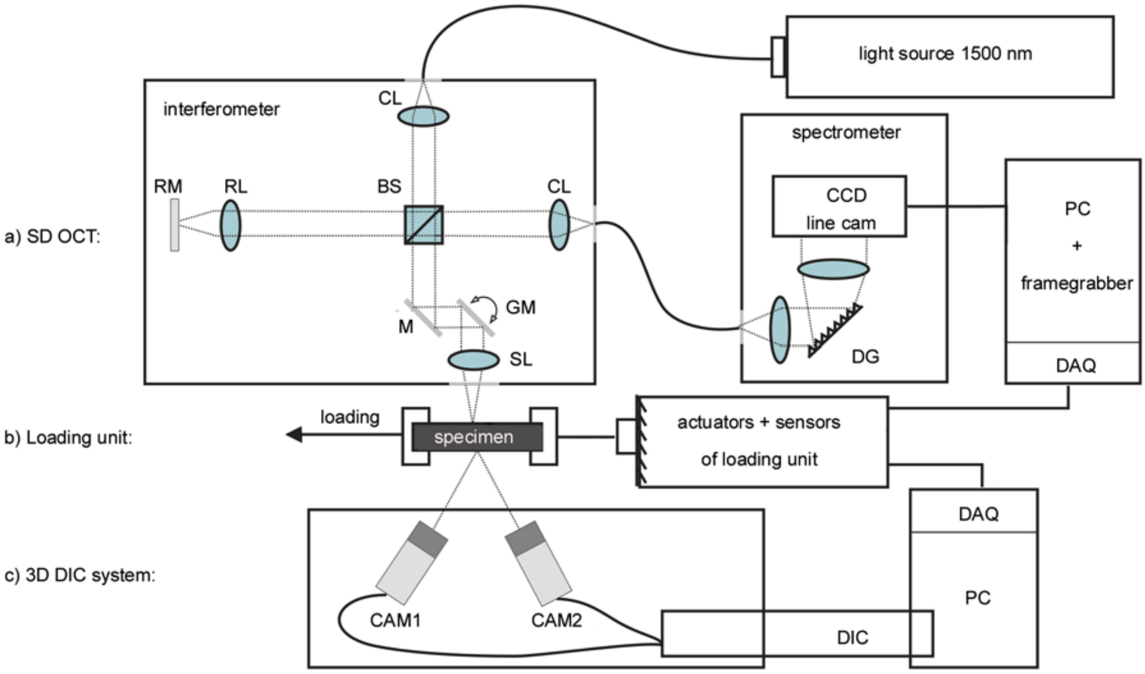

Figure 1. Schematic illustration of the a) spectral domain (SD)-OCT set-up, b) the loading unit and c) the 3D DIC system. Mirror (M), reference mirror (RM), beam splitter (BS), collimator lens (CL), sample lens (SL), reference lens (RL), galvanometer mirror (GM), diffractive grating (DG), data acquisition (DAQ), digital image correlation (DIC).

Switzerland), as well as an InGaAs line camera for the spectrometer. This results in a depth resolution of 19 µm in air, which corresponds roughly to 13 µm in typical polymer materials with a refractive index $n \sim 1.45$. The interferometer of the OCT setup was built in a Michelson configuration, as shown in Figure 1a. A galvanometer mirror was used to scan the specimen laterally at a lateral resolution of ~ 14 µm. Cross sectional images (1000 × 512 pixels) with a sensitivity of 95 dB over depth were acquired at a frame rate of 4 Hz. A customized compact measurement head allowed the integration into the tensile testing machine (TestBench; Bose Inc; Michigan, USA) that is depicted in Figure 1b. The full field strain analysis based on DIC (ARAMIS, GOM Braunschweig, Germany) was performed by the stereoscopic system depicted in Figure 1c. As samples, specimens of elastomeric particle filled polypropylene (PP) were investigated. The size of the specimens was $35 \times 10 \times 2$ mm^3. Those specimens were cut from an injection molded flat plaque with a bench shear. Under identical testing conditions, the materials were investigated during loading of the tensile machine in situ with DIC and then with the OCT-setup. To achieve a high temporal resolution considering an OCT frame rate of 4 Hz, the tensile tests were performed at a velocity of 0.01 mm/s. The maximum displacement was 6.5 mm. Eight specimens were investigated and in both experiments they all showed necking similar in range and position without fracture, with OCT and FFSA providing comparable results.

While the FFSA system surveyed the sample's upper surface in full length (*xy*-plane in Figure 2a), the OCT images showed a cross sectional area of 9 mm in length and 3.5 mm in depth (*xz*-plane in Figure 2a). Figures 2b and 2c show two consecutive OCT frames of the performed measurements. The sample surface was slightly tilted with respect to the sample lens. Due to galvanometer scanning, a small difference in the optical path length of the travelling rays causes an inherent distortion at the left and the right side of the OCT images. Thus, the sample surface appears bent, although it is straight. The OCT images are analyzed in detail in the results section. Advanced image processing methods were applied to determine the local (dis)similarity between temporally subsequent OCT frames, resulting in a so-called Local Dissimilarity (LD-) map, as shown in Figure 2d. Considering a local neighborhood the value of the dissimilarity between subsequent frames was estimated within the corresponding local

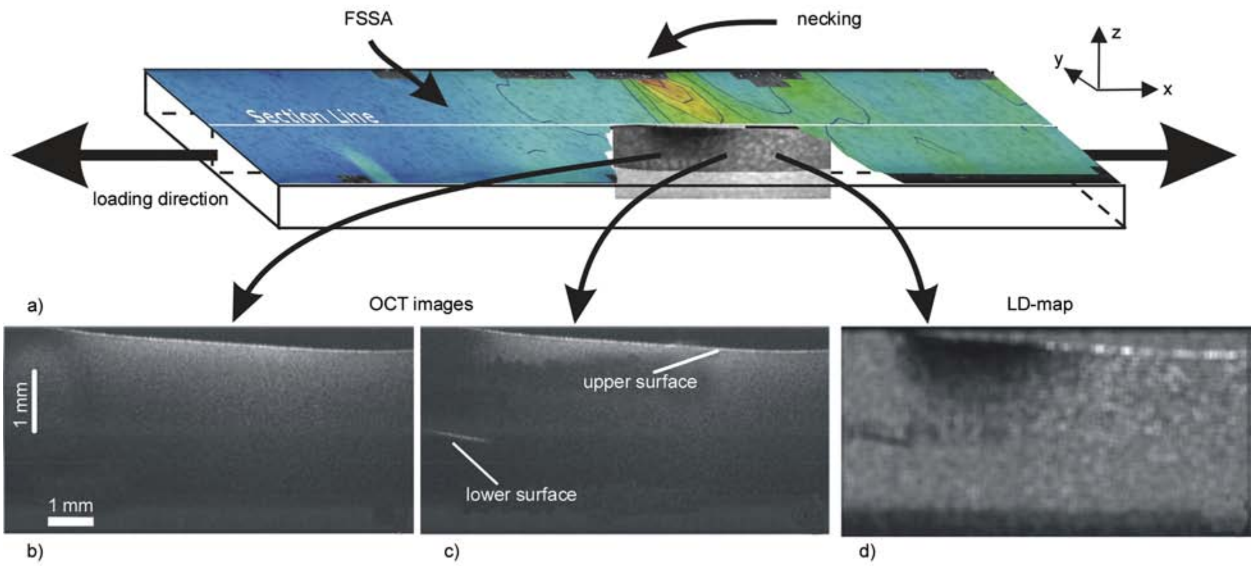

Figure 2. a) Scheme of specimen loaded in axial direction: stress-strain distribution of the upper surface measured with the FFSA system during testing; b) and c) are consecutive OCT scans acquired during testing (1000 × 512 pixels); d) corresponding LD-map

regions. By investigating different dissimilarity measures (be referred to [20]) the Euclidian distance (L2-norm) was chosen here as dissimilarity measure, as depicted in Figure 2d.

3. Results and discussion

The global stress-strain curves were derived from the linear variable differential transformer (LVDT) integrated in the loading test bench and they showed good agreement during the measurements via the OCT and the FFSA system, as shown in Figure 3a. Four significant states i to iv were chosen for comparison of the results, as presented in Figures 3 and 4. Figure 3b shows the color-coded local strain distribution as detected by the FFSA system over the entire upper surface of the specimen. The panels presented in Figure 4b only show the region of the OCT measurements and have a lateral extension of just 9 mm. The panels presented in Figure 4b correspond therefore to the cross sectional OCT images and the corresponding LD maps shown in Figure 4c and 4d. At the beginning of plastic deformation – states i and ii – the global strain is uniformly distributed according to the FFSA measurements shown in Fig-

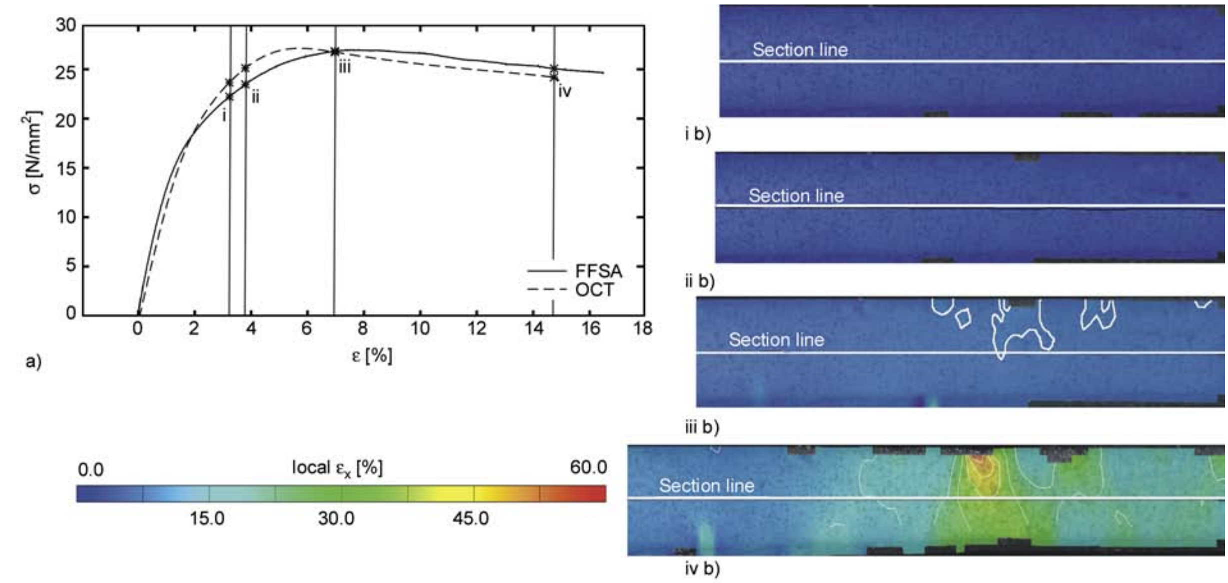

Figure 3. a) Global stress-strain curves measured during the OCT and the FFSA measurement via a linear variable differential transformer (LVDT); b) local strain measured by the FFSA system; the states i to iv are analyzed in detail in the results section

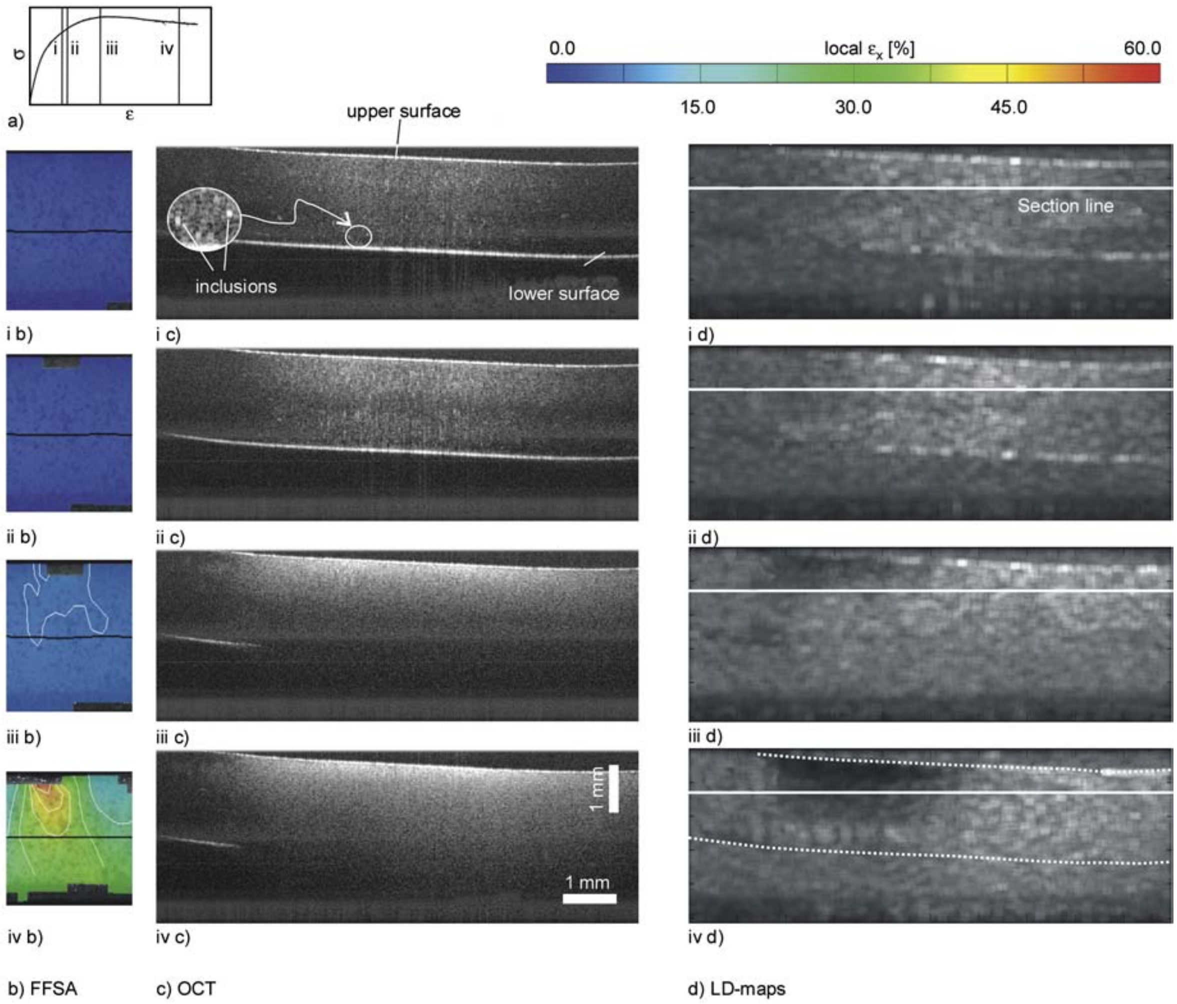

Figure 4. a) Global stress-strain curve; b) local strain measured by the FFSA system; c) OCT measurement within the specimen's cross-section; d) corresponding local dissimilarity map

ure 3 and as magnified detail in Figure 4ib and 4iib. In contrast, the OCT image already reveals a change in the material properties: in Figure 4ic the specimen is still highly translucent showing air inclusions around agglomerated elastomer particles, whereas in the next state Figure 4iic, the development of a brighter region near the upper surface indicating increasing scattering of the material shows up. This can be attributed to small-scale cavitations between the elastomer particles and the host matrix [20]. The corresponding LD maps in Figures 4id and 4iid show a bright region in the center, reflecting this beginning change in opacity. The remaining darker region, including the air beyond the lower surface, is a measure for the high similarity between consecutive frames, and thus also reflects the high signal-to-noise ratio. In states iii and iv flowing of the material is observed: the FFSA measurement shows the onset of necking in Figure 3 and as magnified detail in Figure 4iiib and an advanced state in Figures 3 and 4ivb. The brightness of the specimen in the OCT images 4iiic and 4ivc indicates high scattering of the material implying the beginning of matrix crazing and stress whitening. Multiply scattered photons lead to a reduced penetration depth of OCT and so the lower surface is no more visible. The lower half of the OCT image is dominated by noise of random nature, leading to dissimilarity between consecutive frames. This corresponds to the bright regions in the lower half of the LD maps in Figures 4iiid and 4ivd. Near the upper surface two regions can clearly be distinguished: an increasing dark area representing a static region within the specimen, and to the right a bright region indicating the flowing of material. These two regions form a border, which can be clearly observed and represents, from the microscopic point of view the interface between the static and the highly dynamic area, and in the macroscopic view the front of the necking.

For better comparison with the global stress strain curve, a characteristic value representing the whole LD-map was needed. Anyhow, the lower part of the LD-map was not taken into account, since it includes a large area of air under the sample and shows significant noise in case of reduced penetration depth (state iii, iv). Thus, only the upper half of the image was considered as region of interest, as shown in Figure 5a. As characteristic value, we calculated the percentage of the total 'static area' with respect to the total area in the LD-map. A static area is an area of high similarity between consecutive frames and is represented by dark pixels. In contrary, a dynamic area is an area of low similarity between consecutive frames and is represented by bright pixels. Considering that not only material yielding but also overall elongation, rigid sample movements and noise 'brighten' a pixel, the determination of an appropriate gray level as limit between static and dynamic regions is not trivial. Two alternative grey levels were found suitable for further processing; the first one was chosen near the lower knee of the histogram as shown in Figure 5a. Regions brighter than this level were assumed to be highly dynamic. Regarding the second gray level, regions darker than this level were assumed to be truly static. For calculation of the characteristic value, pixels with values lower than the respective gray level were summed-up via integration of the histogram (I1, I2), as depicted in Figure 5a. To visualize the continuous development of necking within the sample, the resulting curves, I1 and I2, were compared to the global stress strain curve in Figure 5b: The beginning of the tensile test is dominated by a lack of similarity due to rigid movements of the specimen followed by its overall elongation. Thus, the percentage of the static area remains at its minimum for both variants, I1 and I2. At state i a first significant increase of I1 is observed, reflecting a considerable reduction of the dynamic area, and indicating that the specimen has reached a stable position. I2 does not increase until the formation of a static region within the specimen, indicated by an arrow in Figure 5b. This coincides with the moment when crossing the yield point and marks the beginning of the non-uniform elongation flow.

To illustrate the local development of the overall elongation Figure 5c depicts the strain measured along the white section lines indicated in Figure 3b. For state iv the local strain peaks due to necking. Figure 5d shows a comparison of the gray values obtained along the white section lines drawn in Fig-

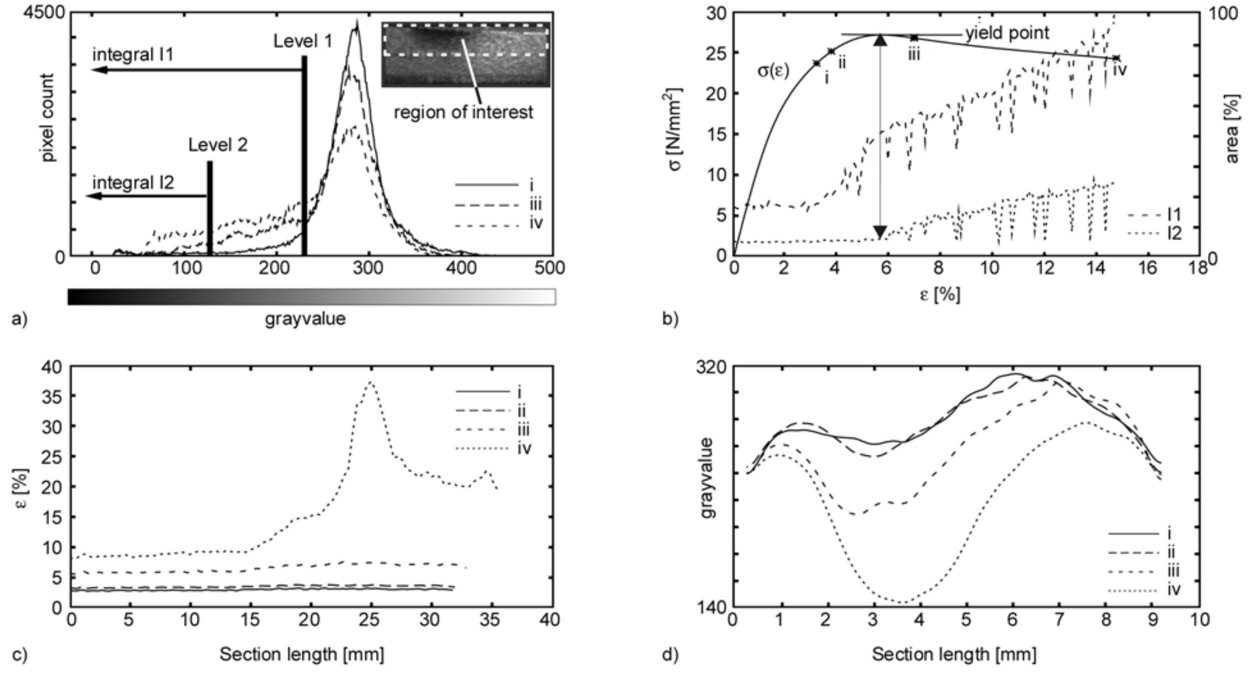

Figure 5. a) LD-Map histograms for three states (i, ii, iii) based on the upper half of the LD-Map (region of interest). b) OCT: Global stress strain curve (left y-scale) in comparison with characteristic values I1 and I2 (right y-scale) computed from the LD-Map. c) FFSA: Local distribution of strain along the section line given in Figure 3b; d) OCT: Local distribution of gray value along the section line of Figure 4d.

ure 4d. The curves show an increasing slope, which corresponds to a rising non-uniformity in elongation.

4. Conclusions

As demonstrated in this work, a combined evaluation approach by FFSA and OCT provides novel complementary information and thus represents a promising procedure to investigate *in situ* dynamic processes occurring inside scattering specimens during tensile tests. In addition to observing the development of micro defects and the progression of structural change, the depth resolved necking front between static and flowing material was detected. OCT is applicable to specimens of arbitrary size, affords no extensive radiation protection in contrast to X-ray computed tomography (CT), and can be customized to be integrated in a testing device. Furthermore, by means of speckle tracking the local distribution of strain can be determined and turns OCT superior to conventional techniques like standard photoelasticity.

Consequently, this great potential is now to be exploited through (i) an enhancement of the OCT setup with respect to higher penetration depth and resolution in both space and time, (ii) a systematic collection of measurement data derived simultaneously via OCT and FFSA systems, and (iii) advanced data processing.

Beyond the qualitative material characterization given already by the local dissimilarity map, furthermore, an extended data processing is needed for analyzing the OCT-imaged material behavior in a quantitative way. A combined statistical and correlation based multi-scale analysis of the speckle patterns is suggested to distinguish between noise and information carrying speckles and finally to calculate the displacement and strain fields. In addition, information in the LD-maps is found primarily in the characteristics of the local distribution. Thus, a more sophisticated approach than the evaluation of the static area portion is needed to generate a scalar quantity describing the whole LD-map or the stress/strain map. Finally, advanced data processing can reveal significant processes occurring within the specimen, such as the start and progress of yielding, identification of the yielding point, localization of the necking front and the development of small scale voids as in the case of matrix crazing.

Acknowledgements

We thank C.K. Hitzenberger and his group at the Medical University of Vienna for continuous advice in OCT technology. The financial support by the Austrian Science Fund (project P19751-N20), the European Regional Development Fund in the framework of the EU-programme Regio 13, the federal state Upper Austria, the Austrian Federal Ministry of Economy, Family and Youth and the National Foundation for Research, Technology and Development is gratefully acknowledged.

References

[1] Karaeva A. A., Serenko O. A., Goncharuk G. P., Bazhenov S. L.: New mechanism of failure of a dispersion-filled polymer composite. Physical Chemistry, **423**, 289–291 (2008).
DOI: 10.1134/S0012501608110018

[2] Bohse J., Kroh G., Wolf H.: Acoustic emission characterizes micro mechanic behavior (in German). Kunststoffe, **81**, 543–547 (1991).

[3] Bar-Cohen Y.: Emerging NDE technologies and challenges at the beginning of the 3rd milleneum – Part I. Material Evaluation, **58**, 17–30 (2000).

[4] Bar-Cohen Y.: Emerging NDE Technologies and challenges at the beginning of the 3rd milleneum – Part II. Material Evaluation, **58**, 141–150 (2000).

[5] Predak S., Lütze S., Zweschper T., Stößel R., Busse G.: Comparative non-destructive characterization. Damage of short glass fiber reinforced polypropylene (in German). MP Materials Testing, **43**, 14–18 (2002).

[6] Hendorfer G.: Active thermography for quantitative analysis of defects (in German). MP Materials Testing, **51**, 400–404 (2009)

[7] Huang D., Swanson E. A., Lin C. P., Schuman J. S., Stinson W. G., Chang W., Hee M. R., Flotte T., Gregory K., Puliafito C. A., Fujimoto J. G.: Optical coherence tomography. Science, **254**, 1178–1181 (1991).
DOI: 10.1126/science.1957169

[8] Bouma B. E., Tearney G. E.: Handbook of optical coherence tomography. Marcel Dekker, New York (2002).

[9] Stifter D.: Beyond biomedicine: A review of alternative applications and developments for optical coherence tomography. Applied Physics B: Lasers and Optics, **88**, 337–357 (2007).
DOI: 10.1007/s00340-007-2743-2

[10] Stifter D., Wiesauer K., Wurm M., Schlotthauer E., Kastner J., Pircher M., Götzinger E., Hitzenberger C. K.: Investigation of polymer and polymer/fibre composite materials with optical coherence tomography. Measurement Science and Technology, **19**, 074011/1–074011/8 (2008).
DOI: 10.1088/0957-0233/19/7/074011

[11] Stifter D., Leiss-Holzinger E., Major Z., Baumann B., Pircher M., Götzinger E., Hitzenberger C. K., Heise B.: Dynamic optical studies in materials testing with spectral-domain polarization-sensitive optical coherence tomography. Optics Express, **18**, 25712–25725 (2010).
DOI: 10.1364/OE.18.025712

[12] Ramesh K.: Digital photoelasticity: Advanced techniques and applications. Springer, Heidelberg (2000).

[13] de Boer J. F., Milner T. E., van Gemert M. J. C., Stuart Nelson J.: Two-dimensional birefringence imaging in biological tissue by polarization-sensitive optical coherence tomography. Optics Letters, **22**, 934–936 (1997).
DOI: 10.1364/OL.22.000934

[14] Wiesauer K., Sanchis Dufau A. D., Götzinger E., Pircher M., Hitzenberger C. K., Stifter D.: Nondestructive quantification of internal stress in polymer materials by polarisation sensitive optical coherence tomography. Acta Materialia **53**, 2785–2791 (2005).
DOI: 10.1016/j.actamat.2005.02.034

[15] Wiesauer K., Pircher M., Goetzinger E., Hitzenberger C. K., Engelke R., Ahrens G., Gruetzner G., Stifter D.: Transversal ultrahigh-resolution polarizationsensitive optical coherence tomography for strain mapping in materials. Optics Express, **14**, 5945–5953 (2006).
DOI: 10.1364/OE.14.005945

[16] Bruck H. A., McNeill S. R., Sutton M. A., Peters W. H.: Digital image correlation using Newton-Raphson method of partial differential correction. Experimental Mechanics, **29**, 261–267 (1989).
DOI: 10.1007/BF02321405

[17] Kirkpatrick S. J., Wang R. K., Duncan D. D.: OCT-based elastography for large and small deformations. Optics Express, **14**, 11585–11597 (2006).
DOI: 10.1364/OE.14.011585

[18] Sheppard C. J. R., Roy M., Sharma M. D.: Image formation in low-coherence and confocal interference microscopes. Applied Optics, **43**, 1493–1502 (2004).

[19] Brezinski M. E.: Optical coherence tomography: Principles and applications. Academic Press, Amsterdam (2006).

[20] Stifter D., Heise B., Bouchot J-L., Major Z., Leiss-Holzinger E., Pircher M., Götzinger E., Baumann B., Hitzenberger C. K.: Spectral domain polarization sensitive optical coherence tomography at 1.55 μm: Novel developments and applications for dynamic studies in materials science. in ‘Proceeding of Optical Coherence Tomography and Coherence Domain Optical Methods in Biomedicine XV, San Francisco, USA’ 78890Z (2011).
DOI: 10.1117/12.873542